The LRS Double Prism Assembly
to be flown on the James Webb Space Telescope

and

Host galaxies of active galactic nuclei in the near infrared

INAUGURAL-DISSERTATION

zur

Erlangung des Doktorgrades

der Mathematisch-Naturwissenschaftlichen Fakultät

der Universität zu Köln

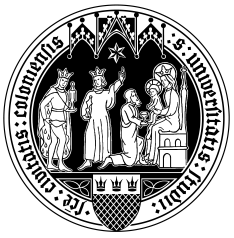

vorgelegt von

Sebastian Fischer
aus Solingen

Köln 2008

Berichterstatter: Prof. Dr. A. Eckart
Prof. Dr. M. Abd-Elmeguid

Tag der mündlichen Prüfung: 21. November 2008

Abstract

The work presented in my thesis covers two aspects of modern astronomy: Observations and instrumentation. Part I of this thesis addresses the design, the development and the qualification of the Low Resolution Spectroscopy Double Prism Assembly (LRSDPA). From an instrumentational point of view, the purpose of the LRSDPA is to make an integration of two prisms, made of Germanium and Zincsulfide, into the imaging module of the mid infrared instrument of the James Webb Space Telescope possible. My design of the LRSDPA answers to several challenging specifications, joining together available envelope, mechanical, thermal, optical and alignment aspects. Both prisms are mounted separately onto a holder via a semi-kinematic interface. The Aluminium components of the demonstration, qualification and flight model all have been manufactured at the mechanical workshop of the 1st Institute of Physics. As it is demanded of all space equipment, the function and performance of the LRSDPA has to be thoroughly demonstrated. The qualification campaign that was conducted in collaboration with the Centre Spatial de Liège, has just been brought to a successful finish.

A brief introduction to the James Webb Space Telescope and its mid infrared instrument are given in Chapters 1 and 2. Chapter 3 then describes in detail the scientific capabilities, the design and the qualification of the LRSDPA.

The low resolution spectroscopy mode will provide prism slit spectroscopy at a resolution of R=100 and cover the wavelength range from 5 μm-10 μm. This mode is particularly aiming at spectroscopic analyses of very low surface brightness objects, such as the first light-emitting galaxies that re-ionized the universe shortly after the big bang. This scenario of re-ionization is supposed to happen shortly after the big bang, at redshifts of z=10-15. At these redshifts, the mid infrared wavelength domain gets in particular interesting, because it covers the rest-frame optical and near infrared wavelengths. Near infrared characteristics are also well suited to investigate key properties of host galaxies of active galactic nuclei (AGN), which constitute part II of my thesis.

The study of host galaxies of quasi-stellar objects (QSO) is handicapped by the bright nucleus outshining its host, even with state-of-the-art telescopes. Untangling the host from the nucleus is easier for closer AGN, and in the near infrared wavelengths, the contrast in spectral energy distributions of active nucleus and host galaxy favor the detection of the host. For these reasons, we have

created a nearby type I AGN sample optimized for near infrared studies, with a redshift limit of z< 0.06. Chapter 4 gives a short introduction to the background motivating the selection of this sample.

In Chapter 5, I present large scale, near infrared, seeing limited slit spectroscopy and imaging of nine of these AGN, carried out with ISAAC, mounted at the very large telescope (VLT) of the European Southern Observatory. Hydrogen recombination lines are observed in seven of the nine sources of which five show a broad component. In three sources, extended 1-0S(1) rotational-vibrational molecular hydrogen emission is detected. Stellar CO absorption is seen in four sources. In one of these objects, an upper limit of the central mass can be determined from the stellar velocity field. H- and Ks-band imaging allow me to determine the morphology class of the host galaxies. Colors (with supplementary J-band 2micron all sky survey images) show that the four galaxies with detected CO absorption are characterized by an overall strong stellar contribution. After removal of the nuclear point source, the host galaxies show colors typical for non-active spiral galaxies.

In chapter 6, I analyze the central kiloparsec of another source included in this sample, HE 0036-5133, using adaptive optics and SINFONI, the integral field near infrared spectrograph of the VLT. This source is mostly famous for its extremely soft X-ray radiation and an X-ray outburst detected during the ROSAT all sky survey in 1990. With the help of different extinction maps and equivalent widths of various stellar absorption lines, the data reveals a deeply hidden nuclear bar and enhanced nuclear star formation, but no prominent sign of extreme QSO-like nuclear activity. In addition, the data supports that the origin of the soft X-ray core is caused by an absent hard X-ray source, rather than a deeply embedded hard X-ray source.

Zusammenfassung

Ich widme mich in meiner Doktorarbeit zwei Aspekten moderner Astronomie: Beobachtung und Instrumentierung. Teil I meiner Arbeit handelt von dem Design, der Entwicklung und der Qualifizierung der "Low Resolution Spectroscopy Double Prism Assembly" (die Doppel Prisma Baugruppe für niedrig-auflösende Spektroskopie, LRSDPA). Die Baugruppe ermöglicht den Einbau zweier Prismen aus Germanium und Zink-Sulfid in die Abbildungskamera des mitt-infrarot Instrumentes des James Webb Weltraum Teleskopes. Mein Design des LRSDPA berücksichtigt viele anspruchsvolle Spezifikationen und kombiniert den zur Verfügung stehenden Platz, mechanische, thermische, optische und Ausrichtungs-Aspekte. Beide Prismen werden über eine semi-kinematische Verbindung separat in eine Halterung montiert. Die Aluminium Komponenten des Demonstrations-, Qualifikations- und Flugmodells des LRSDPA wurden alle in der feinmechanischen Werkstatt des I. Physikalischen Institutes hergestellt. Wie es für alle Weltraum-Applikationen üblich ist, muss die Funktion und Regelgüte des LRSDPA durch Tests gründlich dargestellt werden. Die Qualifikationskampagne, die ich in Kollaboration mit dem Centre Spatial de Liège durchführte, wurde kürzlich zu einem erfolgreichen Ende gebracht.

Ich gebe eine kurze Einführung zu dem James Webb Weltraum Teleskop und seinem mitt-infrarot Instrument in den Kapiteln 1 und 2. In Kapitel 3 wird im Detail die wissenschaftlichen Möglichkeiten, das Design und die Qualifikation des LRSDPA beschrieben.

Die niedrig auflösende Spektroskopie wird Prismen-Schlitz-Spektroskopie mit einer spektralen Auflösung von R=100 über einen Wellenlängenbereich von 5 μm-10 μm bereitstellen. Diese Betriebsart zielt speziell auf die spektroskopische Analyse von sehr leuchtkraftschwachen Objekten, wie etwa die ersten leuchtenden Galaxien, die das Universum kurz nach dem Urknall zurück-ionisiert haben. Es wird erwartet, dass dieses Szenario der Zurück-Ionisierung bei Rotverschiebungen von etwa z=10-15 geschah. Bei diesen Rotverschiebungen wird das mitt-infrarote Licht besonders interessant, da das im Ruhesystem der Galaxie optische und nah-infrarote Licht in diesen Wellenlängenbereich verschoben werden. Charakteristiken im nah-infraroten Licht eignen sich auch gut, um Schlüsseleigenschaften von Wirtsgalaxien aktiver Galaxienkerne (AGK) zu untersuchen, was in Teil II meiner Arbeit behandelt wird.

Die Untersuchung von Wirtsgalaxien Quasi-stellarer Objekte (QSO) wird

durch die Tatsache, dass der helle Kern seine Galaxie überstrahlt, beeinträchtigt. Auch unter zuhilfenahme neuester Teleskope bleiben solche Studien schwierig. Den Wirt von seinem Kern zu entwirren, ist leichter für nahe AGK, und im nah-infraroten Licht erlaubt der Kontrast in der Verteilung der spektralen Energiedichte der AGK und Wirtsgalaxien die deutlichste Detektion des Wirtes. Aus diesen Gründen haben wir eine Auswahl an nahen Typ I AGK getroffen, die mit einer Obergrenze für die Rotverschiebung von $z< 0.06$ für Studien bei nah-infraroten Wellenlängen optimiert ist. Kapitel 4 gibt eine kurze Einführung in den Hintergrund, der die Auswahl dieser Quellen motiviert.

In Kapitel 5 präsentiere ich nah-infrarote, Seeing-limitierte Schlitzspkroskopie und Aufnahmen von neun dieser AGK, die mit ISAAC am Very Large Telescope (VLT) der europäischen Südsternwarte durchgeführt wurden. Wasserstoff-Rekombinationslinien werden in sieben der neun AGK beobachtet, wovon 5 eine breite Komponente zeigen. Drei Quellen weisen ausgedehnten molekularen Wasserstoff auf. Stellare CO-Absorption wird in vier Quellen entdeckt. Für eine dieser Quellen kann daraus das stellare Geschwindigkeitsfeld und eine obere Grenze für die Schwarzlochmasse bestimmt werden. Über H- und K-Band Aufnahmen bestimme ich die Morphologie der Wirtsgalaxien. Farben (mit zusätzlichen J-Band Aufnahmen des 2Micron All Sky Survey) zeigen, dass jene Quellen mit detektierter CO-Absorption auch insgesamt durch einen starken stellaren Beitrag charakterisiert werden. Nachdem die Punktquelle des Kernes abgezogen wurde, zeigen die Galaxien typische Farben nicht-aktiver Spiral-galaxien.

In Kapitel 6 untersuche ich den zentralen Kiloparsec einer weiteren Quelle aus dieser Auswahl, HE 0036-5133. Hierfür benutze ich adaptive Optik und SINFONI, den Integral-Field Spektrographen des VLTs. Diese Quelle ist auffällig durch ihre extrem weiche Röngtgenstrahlung und durch einen Röntgenausbruch, der 1990 während des ROSAT All Sky Surveys detektiert wurde. Mit Hilfe verschiedener Extinktionskarten und Äquivalentbreiten mehrerer stellarer Absorptionslinien zeigen die Daten einen Kern-Balken und erhöhte Sternentstehung im Kern, aber keine markanten Zeichen extremer, QSO-ähnlicher Aktivität. Zusätzlich unterstützen meine Daten, dass die weiche Röntgenstrahlung durch eine fehlende harte Röntgenquelle produziert wird, im Gegensatz zu einer stark eingebetteten harten Röntgenquelle.

Contents

Part I

The LRS Double Prism Assembly

CHAPTER 1

The James Webb Space Telescope

Figure 1.1: *The 1:1 Northrop Grumman James Webb Space Telescope model. In the front, a scientist (myself) indicates the size of the LRSDPA presented in chapter 3 (the spread of the fingers).*

The James Webb Space Telescope (in short the Webb Telescope, or JWST) will be a large, infrared-optimized space telescope, scheduled for launch in early 2013.[1] It is developed jointly by the United States National Aeronautics and Space Administration (NASA), and the European and Canadian Space Agencies (ESA, CSA). JWST is considered as the successor of the famous Hubble Space Telescope (HST) and is one of the NASA/ESA cornerstone missions for the next 2 decades.

It will have a 6.5 m diameter primary mirror. It is passively cooled to approximately 35 K, with a large sun-shield protecting the science instruments from the

[1]The satellite is named after James E. Webb, NASA head from 1961 to 1968. J. Webb was responsible for leading NASA into a balanced direction between *human* space flight and space *science*.

radiation coming from earth, moon and the sun. For this reason, it will be placed at the L2 Lagrange point of the earth-sun 2 body system. JWST will provide the usage of 4 scientific instruments: a Near Infrared Camera (NIRCam), a Near Infrared Spectrograph (NIRSpec), a Near Infrared Tunable Filter Imager (TFI), and a Mid Infrared Instrument (MIRI). Although operating at 30 K (i.e. 8 K for the MIRI instrument), the launch of the satellite will be performed at ambient temperatures in an Ariane V rocket. In space, JWST will unfold (c.f. Figure 1.4) and passively cool down to its operating temperature.

In this chapter, a basic overview over the scientific aims motivating the need for JWST, and its instrument capabilities is presented. For an in-detail discussion of the JWST mission, I refer to Gardner et al. (2006).

1.1 Scientific Aims

The reasoning behind the JWST mission is that there are certain astrophysical questions that cannot be answered with ground-based telescopes alone. The Webb Telescope will provide insights into 4 distinct fields of modern Astronomy:

- How did the Universe build up its present elemental/chemical composition?
- How did the first galaxies form, and how do galaxies evolve?
- How do stars and proto-planetary systems form?
- How do planets form? How are habitable zones established?

1.1.1 The Reionization of the Universe

Theory and observation predict that the early universe was of very simple nature. The Big Bang produced (in decreasing order of present mass-energy density): dark energy, dark matter, hydrogen, helium, cosmic microwave and neutrino background radiation, and additional trace quantities of lithium, beryllium, and boron. As the universe expanded, the consequent cool-down allowed for the formation of hydrogen molecules. After about $100 \cdot 10^6$ years after the Big Bang, it is thought that the first individual stars could form (Barkana & Loeb 2001). Theory predicts that insufficient cooling mechanisms, caused by the zero metallicity chemical abundance[2], highly favored the production of (so called *type*

[2] In astronomy, usually everything heavier than Helium is considered as metal.

III) stars with masses between 30 and 500 $M_\odot$, burning for only a few million years before meeting a violent death (Bromm & Larson 2004). These stars ended either in a core-collapse supernova (type II) or a black hole. Probably, the black holes started to swallow gas and other stars to become mini-quasars, which grew and merged to become the supermassive black holes found at the centers of all massive galaxies (with significant bulge component, Magorrian et al. 1998). The supernovae enriched the surrounding gas with the chemical elements produced in their interiors, and future generations of stars consequently showed higher metallicities. JWST aims at the detection of these supernovae and mini-quasars.

Following the emergence of the first bright objects in the universe, hydrogen in the intergalactic medium was reionized. Results from the Wilkinson Microwave Anisotropy Probe (WMAP, Kogut et al. 2003; Page et al. 2007; Spergel et al. 2007, Figure 1.2) combined with data on quasars at $z \sim 6$ from the Sloan Digital Sky Survey (SDSS; Fan et al. 2002) suggest that this reionization had a complex history (Cen 2003b). Although there are indications that galaxies produced the majority of the ultraviolet radiation which caused the reionization, the contribution of quasars could be significant.

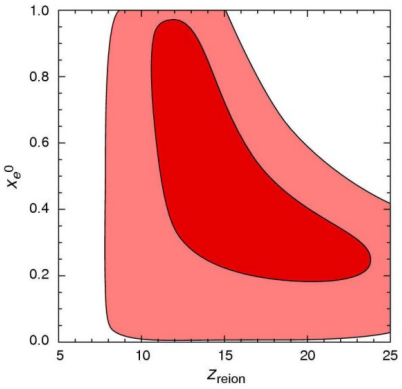

Figure 1.2: *WMAP constraints on the reionization history. The plot shows the 68% and 95% joint 2-d marginalized confidence level contours for a model in which the Universe is partially reionized with an ionization fraction x_0^e at z_{reion}, and then fully reionized at $z = 7$. The WMAP data are inconsistent with a single epoch of reionization at $z \sim 6$, and argue for a complex reionization history. (From* Spergel et al. 2007*).*

JWST will address the when, how, and what in this theme: When exactly, and how, did reionization occur? What are the first galaxies? What sources were responsible for the reionization? JWST will conduct ultra-deep near-infrared surveys with spectroscopic and mid-infrared follow-up to find and identify the first galaxies to form in the early universe. It will determine the processes that caused reionization through spectroscopy of high-redshift quasars or galaxies, and studies of the properties of galaxies during that epoch. Low resolution mid infrared spectroscopy will provide the redshift of bright sources with prominent low/zero metallicity.

1.1.2 The Assembly of Galaxies

Theory explains the assembly of galaxies as the hierarchical merging of dark-matter concentrations (e.g. White & Frenk 1991; Cole et al. 1994). Small objects formed first, merged together, and grew larger. Throughout this dynamical process, the chemical composition evolves as more and more heavy elements are produced in successive generations of stars. The diverse taxonomy and properties of galaxies found in the present-day universe is considered as the result of the interplay between the luminous sources and dark matter. Although most of the observed early galaxies are smaller and more irregular than their present day counterparts, this scenario is questioned by the presence of extremely massive ellipticals already at redshifts of z ~6 (e.g. Bouwens et al. 2006, and references therein). However, there are also antithetic studies that deny a redshift of these objects of z>4 (e.g. Dunlop et al. 2007).

Despite the recent progress in this field, many questions are still open. How did the heavy elements form? What physical processes determine galaxy properties? When and how did the Hubble Sequence of galaxies form? What are the roles of starbursts and black holes in galaxy evolution? To answer these questions, JWST will observe galaxies back to their earliest precursors, so that we can understand their growth and evolution. JWST will conduct deep wide-imaging and spectroscopic surveys of thousands of galaxies to study morphology, composition and the effects of environment. It will conduct detailed studies of individual ultra-luminous infrared galaxies (ULIRGs) and active galactic nuclei (AGN) to investigate the mechanisms behind these sources (Gardner et al. 2006).

1.1.3 The Formation of Stars and Proto-planetary Systems

Despite the advances in stellar astronomy in the last 100 years, the detailed processes involved in star formation are yet to be determined. The key objective in the field of the formation of Stars and proto-planetary systems is to unravel the birth and early evolution of stars, from infall on to dust-enshrouded protostars, to the birth of planetary systems.

Already for a single, isolated low-mass star, the evolution to a planetary system is a complex process (e.g. Shu et al. 1987). More recent observations show, however, that fragmentation of clouds plays a significant role, giving only rare occasions where stars can form in isolation. This means stars form in highly dynamic clusters of protostars, and the situation becomes even more complex.

In addition, observations of the earliest stages of star formation are hindered by the intrinsic fact that they occur in heavily obscured clouds. In order to pene-

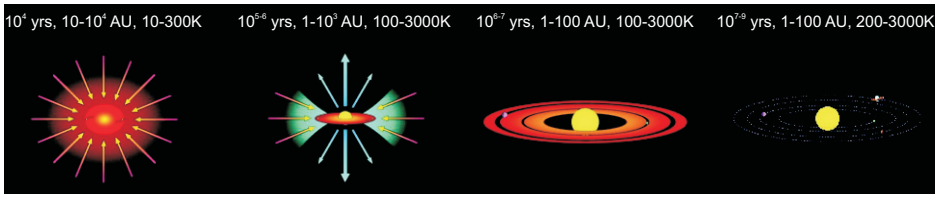

Figure 1.3: *The formation of an isolated planetary system (following Shu et al. 1987; Gardner et al. 2006).*

trate the dust and detect the emission from gas and dust at temperatures between 3000 K - 100 K, imaging and spectroscopy at wavelengths between 1 μm - 30 μm is crucial.[3]

JWST will address several key questions in this scheme: How do protostellar clouds collapse? What role does the environment play in star formation? What is the initial mass function (IMF) of stars at substellar masses? How do proto-planetary systems form? How do gas and dust coalesce to form planetary systems? JWST will observe stars at all phases of their evolution, from infall onto dust-enshrouded protostars, through the formation of planetary systems, penetrating the dust to determine the physical processes that produce stars, planets and debris disks.

1.1.4 The Formation of Planets

Understanding the origin of the Earth and its ability to support life is an important objective for astronomy. Mandatory aspects in this scenario include understanding the formation of planetesimals, and how they combine to form larger objects. We do not know how planets reach their present orbits, and how the large planets affect the smaller ones in solar systems like our own. We want to learn about the chemical and physical history of the small and large objects that formed the Earth and delivered the necessary chemical precursors for life. The cool objects and dust in the outer Solar System are evidence of conditions in the early Solar System, and are directly comparable to cool objects and dust observed around other stars.

JWST will address several key questions in this theme: How do planets form? How are circumstellar disks like our Solar System? How are habitable zones established? JWST will determine the physical and chemical properties of planetary systems, including our own, and investigate the potential for the

[3]For a blackbody radiator at a given temperature T [K], following Wien's law, the maximum of the Planck curve (in μm) is roughly given by 3000 / T.

origins of life in those systems. JWST will use coronagraphy to investigate extrasolar planets and debris disks, and will compare these observations to objects within our own Solar System.

1.2 JWST Hardware Features

The above mentioned scientific challenges require an extremely sensitive infrared telescope, with a wide field of view (FOV), high angular resolution, a stable point spread function (PSF), and wide wavelength coverage for imaging and spectroscopy.

1.2.1 The Satellite

The Webb Telescope consists of the optical telescope element, the integrated science instrument module (ISIM), a sunshield, and a spacecraft (Figure 1.4). For sufficient resolution and light collecting area, JWST's primary mirror has a diameter of 6.5 m. In order to fit into the Ariane V launch vessle, the mirror is segmented into 18 segments, and foldable (2 segments on each side are flipped against the satellite). Each segment is made of Beryllium, similar to the ISO and Spitzer primary mirrors. Figure 1.5 compares the size of the primary mirror to present day (optical/NIR) space telescopes.

In order to minimize the thermal background observed by JWST, the satellite is passively cooled to a temperature of 40K (and actively in the case of the Mid infrared instrument which provides its own cooler for cooldown to an operating temperature of 6 K). The location of JWST at the L2 Lagrange point of the earth-sun system ensures that earth and sun are always aligned along the same direction. The science instruments and optical elements are protected of the thermal radiation coming from sun, earth and moon by a 5-layer sunshield which covers an area of about 22 m times 13 m. This allows the telescope to be background limited by zodiacal light at wavelengths below 10 μm, and provides high sensitivity up to mid infrared wavelengths of 29 μm. The improvement in sensitivity over Spitzer as well as future 30 m ground based telescopes at wavelengths $> 2\,\mu$m is apparent (Figure 1.5).

1.2.2 The Science Instruments

In this Section, three of the four science instruments contained in ISIM are briefly described. As member of the European Consortium which is responsible for the development of the mid infrared instrument, and a member of the MIRI test

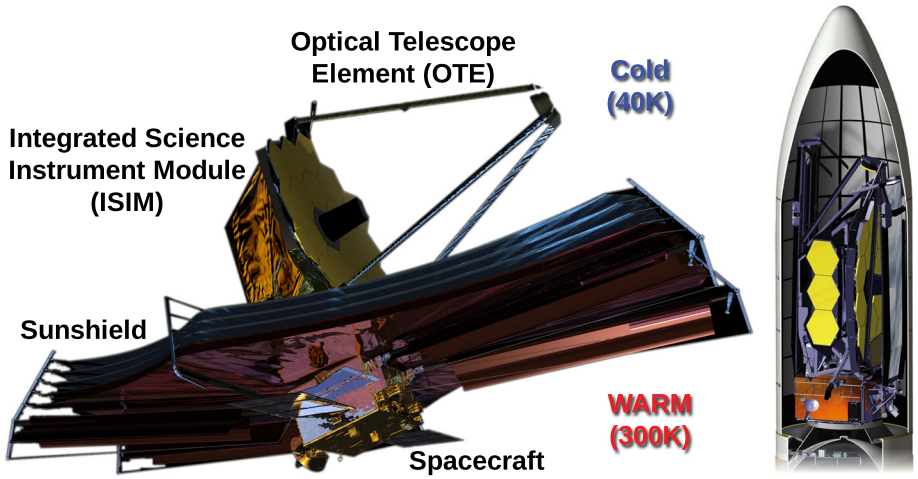

Figure 1.4: *Left: The composition of the James Webb Space Telescope. ISIM contains the four science instruments described in Section 1.2.2. The sunshield has about the size of a tennis court and divides the satellite into a cold (40K) and a warm (300K), sun facing, region (NASA). Right: the folded JWST inside the Ariane V launch vessel (Jakobsen & Jensen 2008).*

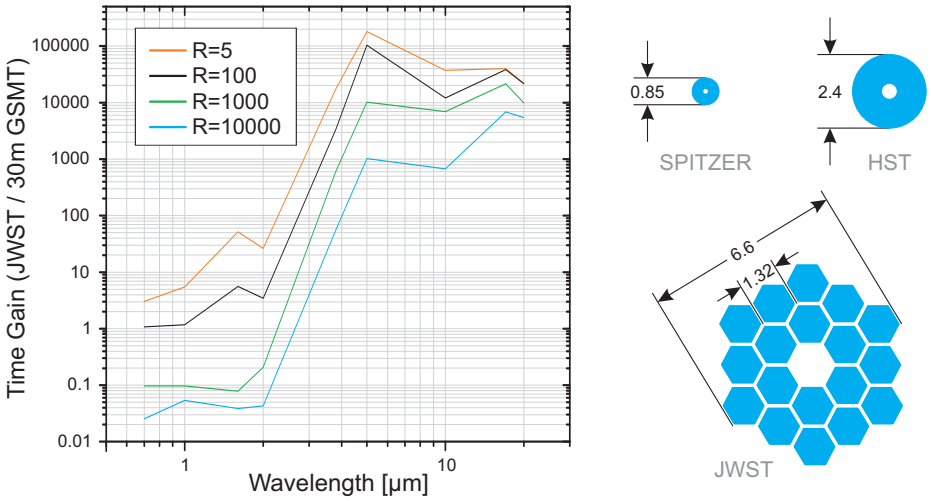

Figure 1.5: *Left: A comparison of imaging sensitivities between JWST and a tentative 30 m telescope (scheduled for ~ 2015-2020) is shown (Mountain 2005). The vertical axis displays the time gain in relative units (time gain = 1.0 means an observation with the same S/N on a point source will take the same time with both telescopes; time gain > 1 means JWST is faster). JWST's low thermal background becomes prominent at wavelengths > 2 μm. Right: The scales of the primary mirrors of HST, Spitzer and JWST are compared. The JWST primary mirror is made up of 18 hexagonal segments, each with a diameter of 1.32 m (flat to flat). In order to fit into the launch rocket, the mirror is foldable.*

Table 1.1: *The performance of the JWST (Gardner et al. 2006).*

Parameter	Capability
Wavelength	0.6 - 29 μm
Image Quality	Strehl ratio of 0.8 at 2 μm
Telescope FOV	Instruments share ~ 166 squarearcmin FOV
Orbit	Lissajous orbit about L2
Celestial Sphere	100% annually
Coverage	39.7% at any given time (Field of Regard)
	100% of sphere has at least 51 contiguous days visibility
	30% for > 197 days
	Continuous viewing zone < 5^o from each ecliptic pole
Efficiency	Observatory ~ 80%
	(20% overheads dedicated to slewing, calibrating, etc.)
	Overall efficiency > 70%
	(10% dedicated to std. star calibration, scheduling, etc.)
Mission Life	Commissioning in less than 6 months
	5 year minimum lifetime after commissioning
	10 year supply of fuel for position maintaining

team that is qualifying the performance of the instrument, I dedicate MIRI its own chapter in Chapter 2.

The Near Infrared Camera - NIRCam

NIRCam provides imaging in the wavelength range from 0.6 μm to 5.0 μm. The camera splits the incoming light into a short wavelength arm (0.6 - 2.3 μm) and a long wavelength arm (2.4 -5.0 μm) and is capable of performing simultaneous imaging in both arms. In addition to various narrow, medium and broad band filter observations, it will provide a coronagraphy mode. NIRCam's Field of view is 2.2 $\times$ 4.4 arcminutes (Burriesci 2005; Steakley 2005). NIRCam is provided by the University of Arizona.

The Near Infrared Spectrometer - NIRSpec

NIRSpec is a multi-object spectrometer in the near infrared wavelength. It will provide simultaneous spectroscopy of > 100 sources - selected with a microshutter array, and additional slit spectroscopy (with slit widths of 100, 200 or 400 milliarcsecs) of a 3 $\times$ 3 squarearcmin FOV. The achieved resolutions

are R ~ 100 (over the full NIR band from 0.6 - 5.0 μm) and R ~ 1000 (1 - 1.8 μm; 1.7 - 3.0 μm; 2.9 5.0 μm). A supplementary integral field unit (IFU) provides imaging-spectroscopy over a 3×3 squarearcsec FOV, at a spectral resolution of R ~ 2700 over the 3 NIRSpec bands (Bagnasco et al. 2007). NIRSpec is provided by ESA (with additional component contributions from NASA).

The Tunable Filter Imager - TFI

TFI is the science instrument attached to the fine guidance sensors (FGS) which are used for the pointing of the telescope. The tunable filter imager provides narrow band imaging over a 2.2 $\times$ 2.2 squarearcmin FOV (spectral R ~ 100). The filter-wavelengths can be selected in wavelengths between 1.6 - 2.6 and 3.1 - 4.9 μm (Rowlands et al. 2004). TFI/FGS are provided by CSA.

CHAPTER 2

The Mid Infrared Instrument

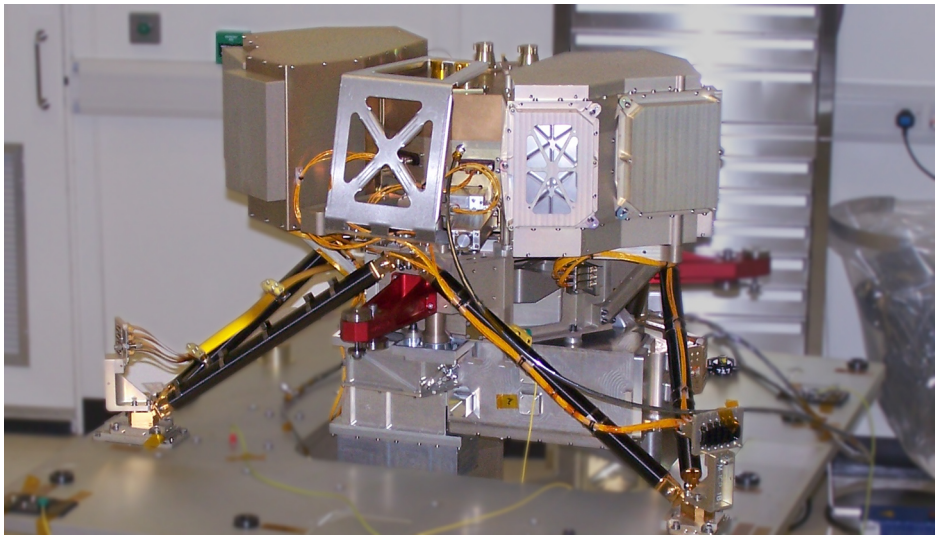

Figure 2.1: *The Verification Model (VM) of JWST's Mid Infrared Instrument (©Rutherford Appleton Laboratories).*

MIRI is a lightweighted, all aluminium, instrument that will provide imaging and spectroscopy over the 5 - 25 μm wavelength range (Wright et al. 2008b). Its design consists of two main modules, an imager and an integral field unit (IFU) spectrometer.

MIRI is mounted to the ISIM structure (via a carbon fiber hexapod) and thus is located in JWST's 40 K environment. The operating temperature of MIRI for science observations, however, is between 6 -8 K. For this reason, MIRI incorporates its own dedicated active cooler (located at the sun facing side of the sunshield). The organization of the optical system of the MIRI instrument is presented in Figure 2.2.

The MIR-instrument is developed in a 50/50 share between ESA and NASA. NASA provides the cryogenic cooler, the programming of the MIRI flightsoftware & the detectors (Raytheon MIR detectors), and ESA the optical system.

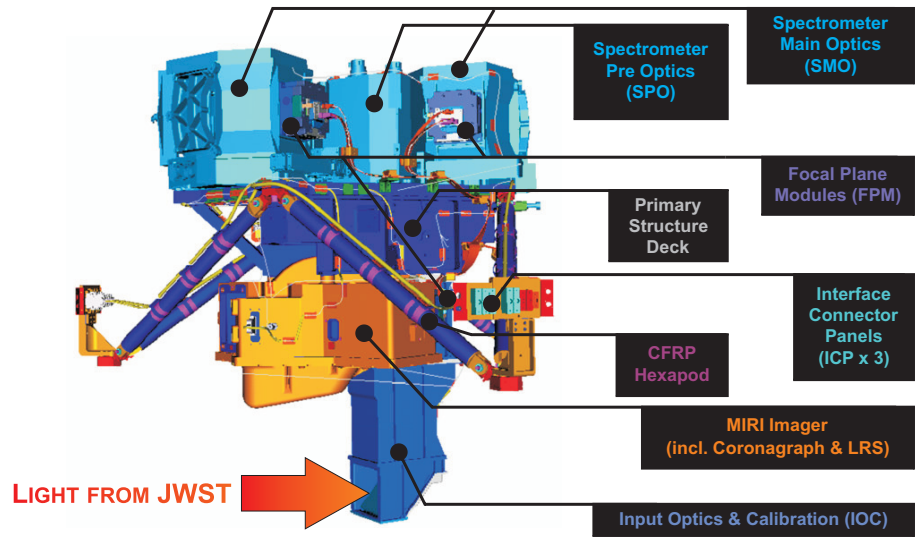

Figure 2.2: *The basic layout of the MIRI optical system (MIRI image from MIRI optical system critical design review, CDR).*

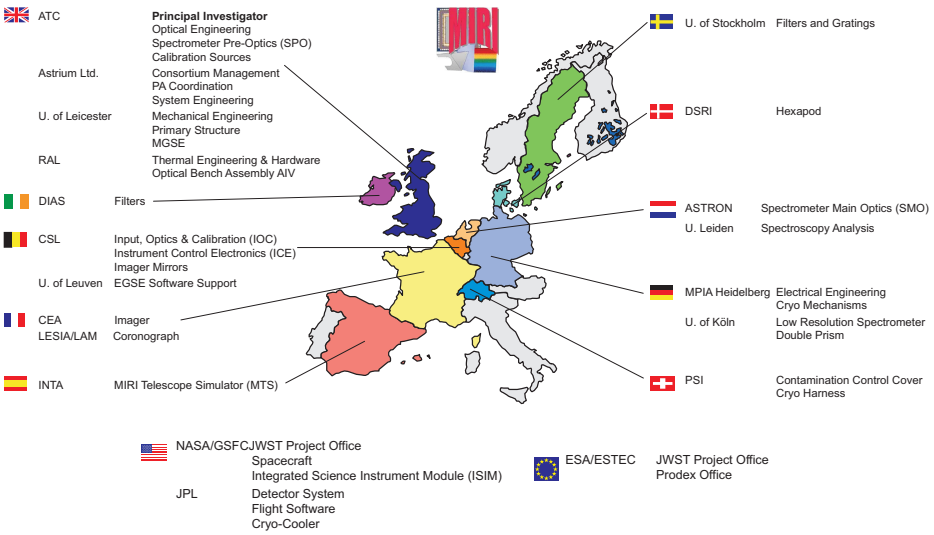

Figure 2.3: *The European Consortium (EC) involved in the development of MIRI. It consists of 21 institutes, distributed over 10 European nations. Concerning hardware, the EC provides the optical system (Figure 2.2), the cryo cooler is provided by the Jet Propulsion Laboratories. MIRI flight software is developed at NASA, with EC contributions in the form of performance and functional scripts (Image from MIRI optical system CDR).*

Due to the enormous costs, ESA has distributed the development of the MIRI instrument over institutes from all Europe. Figure 2.3 gives an overview over the contributions of the various nations. Almost each component of the optical system is provided by a different institute, requiring a lot of communication between the different members and meticulous documentation. Astrium has been appointed with the task of the overall management of the consortium (Wright et al. 2008a).

For the evaluation of the performance of MIRI, a dedicated test-team has been established inside the EC, with additional NASA personnel. At the time of writing of this thesis, the MIRI verification model (VM) functional and performance tests are carried out (August - October 2008). The cold test sequence alone requires a consecutive test-time of 2 months, with data being taken 24h a day (first results can be found in Lim et al. 2008).

2.1 The spectrometer

The medium resolution spectrometer (MRS) is an integral field spectrometer which provides spectroscopy from 5 - 25 μm with an average resolving power of R$\sim$2000 (Kroes et al. 2005). The MRS field of view is about 3.5 $\times$ 3.5 squarearcseconds.

The spectrometer is divided into the Spectrometer Pre-optics (SPO) and Spectrometer Main-optics (SMO, c.f. Figure 2.2). Spectral filters for pass-band selection and the image slicer are included in the SPO, the actual dispersion of the light is applied in the SMO via diffraction gratings. For optimized performance over the broad MIRI wavelength range, the spectrometer is split into four separate channels with an optimized spatial sampling.

The spectrometer will have a sensitivity (i.e. S/N of 10 after 10^4 s of integration) of $0.8 \cdot 10^{-20}$ W m^{-2} at 9.2 μm and $4.3 \cdot 10^{-20}$ W m^{-2} at 22.5 μm respectively. It will provide the following spectroscopy modes:

- $2000 < \mathrm{R} < 7000$ @ $5\mu m < \lambda < 10\,\mu m$;
- $1800 < \mathrm{R} < 6000$ @ $10\mu m < \lambda < 15\,\mu m$;
- $1600 < \mathrm{R} < 5000$ @ $15\mu m < \lambda < 27\,\mu m$.

2.2 The imager

The MIR-imager (MIRIM) provides not only, as the name might imply, the imaging capabilities of the MIR-instrument, but also coronagraphy and low resolution

Table 2.1: *MIRIM bands for imaging, coronagraphy and spectroscopy. In the MIRIM filterwheel, there are 18 different positions, with 10 imaging filters, 4 coronagraphy filters, one double prism, a neutral density filter, an alignment lense and a closed position.*

Mode	Center	Bandwidth
Imaging	5.6	1.2
Imaging	7.7	2.2
Imaging	10.0	2.0
Imaging	11.3	0.7
Imaging	12.8	2.4
Imaging	15.0	3.0
Imaging	18.0	3.0
Imaging	21.0	5.0
Imaging	25.5	4.0
Imaging	25.5	4.0
Coron.	23.0	4.6
Coron.	10.65	0.53
Coron.	11.4	0.57
Coron.	15.5	0.78
Spect.	7.5	5.0

spectroscopy (LRS) (c.f. Table 2.1, Amiaux et al. 2008).

The detector is a 1024×1024 pixels array, with a sampling of 0.11 arcsec/pixel. It will be Nyquist sampled at 7 μm. The FOV of the imaging mode is 1.25×1.88 squarearcmin. The coronagraphic mode has a dedicated field on the MIRIM detector, with one region for Lyot and three 4-Quadrant-Phase-Mask coronagraphy (each region is optimized for a respective wavelength).

The low resolution spectroscopy mode is described in detail in Chapter 3. In particular, Figure 3.5 shows the optical layout of the imager, with the filterwheel in the LRS-position, and a raw frame of the VM MIRIM detector to illustrate its illumination and the dedicated regions.

CHAPTER 3

The Low Resolution Spectroscopy Double Prism Assembly

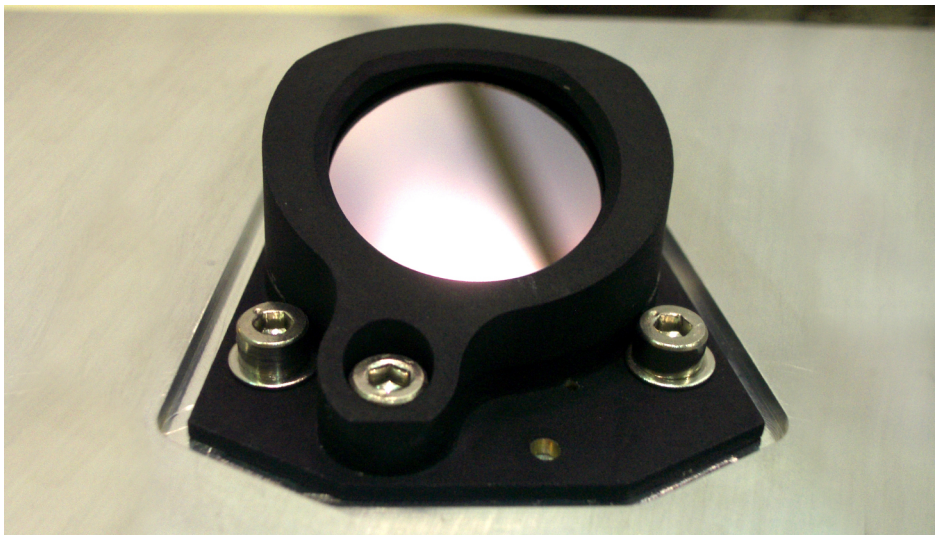

Figure 3.1: *The flight model of the Low Resolution Double Prism Assembly during its assembly.*

3.1 Introduction

The purpose of the Low Resolution Double Prism Assembly (LRSDPA) is to position two prisms, made of Zinc-Sulfide and Germanium, accurately in the filterwheel of the MIRI imager. The low resolution spectroscopy mode of the MIRI imager then will allow to perform prism slit-spectroscopy in the wavelength-range from 5-10 microns at a resolution of R=100. This mode is particularily aiming at spectroscopic analyses of very low surface brightness objects, such as deeply embedded (proto-)stars, or the first light-emitting galaxies that re-ionized the universe shortly after the big bang.

A general problem in the design of sientific satellites is the limitedness of available room. The other main challenge is that the prisms, intrinsic fragile crystals, will be exposed to extremely high levels of vibrations during the launch of the rocket. The double prism assembly compensates for this and provides a safe mount of the prisms, with as few induced stress into the optical component as possible. Springs provide a safe fixation - without overload - of the prisms, while gold-foils provide a smooth contact between crystal and Aluminium parts.

Starting with a scientific motivation on why the low resolution spectroscopy mode is essential for the science aims of JWST, the following chapters will explain in detail how the prisms are mounted, what critical aspects I had to consider in the development of the design and what test campaigns we made to qualify the performance of the LRSDPA. This chapter has been published in part in Fischer et al. (2008), Rossi et al. (2008), and in several documentation papers for the European MIRI consortium.

3.2 Science Drivers

For an extensive discussion of the scientific objectives of JWST, I refer to Gardner et al. (2006). The natural field of appliance for a sensitive MIR spectrometer is to spectroscopically study higher-redshifted counterparts of the galaxies in our local universe. For example, at a redshift of z = 3, the near infrared J, H and K-bands ($\lambda = 1.25 - 2.4\,\mu$m) are shifted into the 5 - 10 μm band of the LRS mode. These observations yield information on the evolution of galaxies and AGN over cosmic timescales. Hence, local spectroscopic infrared studies (e.g. Rodríguez-Ardila et al. 2000a) can be expanded to larger lookbacktimes with a reasonable amount of integration time compared to ground-based MIR telescopes, which suffer from the high thermal background of the atmosphere and the telescopes.

However, one of the most ambitious scientific objectives of the James Webb Space Telescope is the detection of the first bright objects in the universe - which ended the cosmic 'Dark Ages': At about 180 million years after the Big Bang (Barkana & Loeb 2001), the initially hot universe expanded and cooled down below the sublimation temperature of hydrogen molecules. This allowed for the formation of the very first stars in the universe, which consisted only of hydrogen and helium. Due to the lack of sufficient cooling mechanisms in these zero metallicity stars, their effective temperature is of the order of $10^5\,K$ (Bromm et al. 2001, e.g.). On the one hand, this causes the Jeans mass to be much higher than for solar mass metallicities. Hence, zero metallicity stars favor masses of $> 100\,M_\odot$. On the other hand, this means that these sources are very effective in ionizing hydrogen and helium. However, the high effective temper-

atures imply also low UV / optical fluxes: The spectral energy distribution of these stars at temperatures of $\sim 10^5\,K$ follows that of a black body of corresponding T_{eff}. Here, UV and optical band fall into the Rayleigh-Jeans limit, where the flux of the bolometric luminosity function scales with T_{eff}^{-3}. Most recent results from the Hubble Ultra-Deep Field observations predict that this process of re-ionization was ignited at redshifts of $z_{reion} = 15 \pm 5$ (Panagia et al. 2005); WMAP observations of the cosmic microwave background result in a redshift of $z_{reion} = 10.9^{+2.7}_{-2.3}$ (Spergel et al. 2007). At these redshifts, the restframe UV / optical gets shifted into the mid-infrared. Still, the faintness of these stars makes observations challenging, even for JWST. Panagia (2003) discuss that JWST will not be able to determine metallicities for low-metallicity starburst objects at a spectroscopic resolution of R=1000. Here MIRI's double prism low resolution spectroscopy mode (R=100) becomes crucial due to its increase in sensitivity. For the brightest zero-metallicity star clusters and dwarf galaxies, the LRS mode is able to not only determine redshifts, but also to give estimates on their metallicity. For example, as can be seen in Figure 3.2, the [OIII]- and HeII lines are sensitive indicators to changes in metallicities and at the expected redshifts readily accessible for the LRS mode.

3.3 Design Drivers

The fundament of the LRSDPA are the requirement specifications defined by the French imager team (Section 3.3.1).[4] The design presented in this thesis is the result of a redesign of the LRSDPA's demonstration model structure (Fischer et al. 2006c): Initially, the accelerations expected at the level of the optical elements of the MIRIM filterwheel were of the order of 20 gRMS (c.f. Section 3.3.1). An anomaly during vibrational tests of the demonstration model of the filterwheel disk required a redesign of the filterwheel that affected the vibrational loads on the optics significantly (the load increased to 55 gRMS). At this stage, the demonstration model of the LRSDPA, designed for the initial levels, was already manufactured. During the demonstartion model vibration test campaign of the LRSDPA, one of the two prisms (the Germanium prism) was not able to withstand the final applicable axial random vibrations (Figure 3.3).

[4]The responsabilities of the development of the LRSDPA have been shared between University of Cologne (UoC), which conducted the development of the design and the manufacturing of all LRSDPA parts except the prisms, and the Centre Spatial de Liège (CSL), which provided the interface to the discussions with the commissariat à l'énergie atomique (CEA), the procurement of the prisms and the procurement of the coating of all components. The qualification campaign oh the LRSDPA has been performed in a team effort between UoC and CSL.

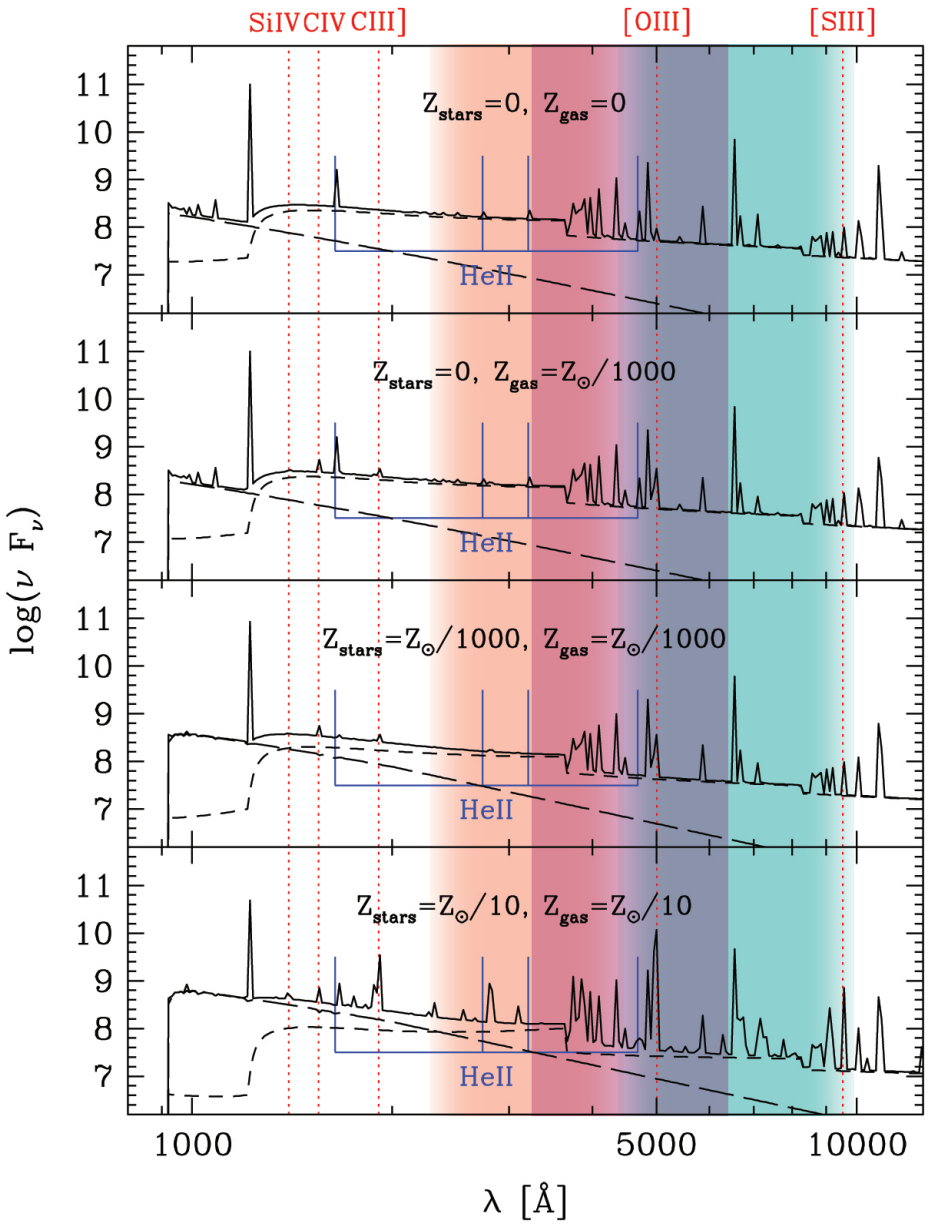

Figure 3.2: *Taken from* Panagia *(2003): The synthetic spectrum of a zero-metallicity HII region (top panel) is compared to that of HII regions with various combinations of stellar and nebular metallicities (lower panels). The long-dashed and short-dashed lines represent the stellar and nebular continua, respectively. In addition, the 5-10μm band corresponding to a redshift of $15^{+5\,(red)}_{-5\,(blue)}$ is overlayed.*

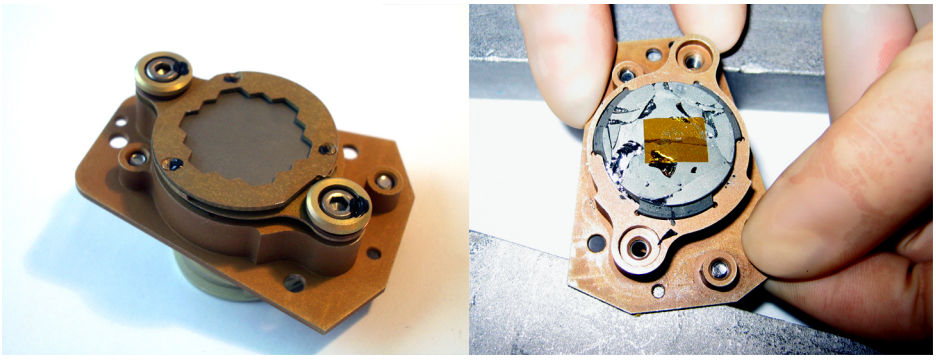

Figure 3.3: *The LRSDPA demonstration model (DM) before (left) and after (right) the axial random vibrations. Both images show the Germanium side of the LRSDPA, on the right hand side, the cover has been removed. The DM was designed for vibration levels of 20 gRMS. Due to a change in the filterwheeldesign, the vibration levels changed to a maximum of 55 gRMS in axial direction (Section 3.3.1). These high accelerations have shattered the prism completely.*

The redesign has addressed this problem and optimized the prisms' mechanical robustness against vibration loadss. Its success has been proven by the successful qualification of the vibratonal test campaign (Section 3.4.2). Naturally, some of the requirements are much more crucial and design-driving than others. The positioning accuracy of the prisms inside the holder, the enormous levels of accelerations and the tight allocated outer envelope all have serious impacts on the final design. The compliance of the design to these most critical requirements is described in detail in sections 3.3.2, 3.3.3 and 3.3.4.

3.3.1 Requirements

General criteria concerning design, performance and qualification of space equipment are defined by the European Cooperation for Space Standardization (ECSS) guidlines - e.g. structural aspects to be considered in the design can be found in ECSS-E-30, Part 2.

While I always have taken these general rules into account, LRSDPA specific requirements have been defined by CEA, in conformity to their optical design of the MIRI imager, of which the LRSDPA is an official subcomponent. These requirements are described in detail in Dubreuil et al. (2008) and listed as brief overview in table 3.1. Some requirements are only of a formal nature, such as that CEA are provided with all test results. Mandatory specifications deal with dimensions, positioning and according tolerances of the two prisms (Section 3.3.4). However, some minor requirements cannot be met, e.g. due to the small available room, the size of the screws mounting the LRSDPA to the filter-

wheel had to be decreased to M3 screws (cf. spec 77), and a small exceedance out of the allowed outer envelope is inevitable. Any of these discrepancies to the requirements has been discussed and agreed upon with the imager team of CEA.

For additional qualifications, on the other hand, the ECSS standards always form the main guideline. For example, the qualification of a modified screw that is in use to mount the LRSDPA onto the filterwheel, has been performed in accordance to ECSS-Q-70-46A.

Table 3.1: *Requirement Specifications of the LRSDPA, defined by CEA (Dubreuil et al. 2008).*

Spec No.	Requirement	Value
Spec 01	Dimensional Parameters given at 20^o C	
Spec 02	The prisms are unpolished along the generating direction	
Spec 03	(Ge) Material is Ge Standard Optical Grade	
Spec 04	(Ge) The optical requirements apply to the useful optical aperture taking into account the 3.8 % pupil shear	
Spec 05	(Ge) Entrance face angle	$2.7337^o \pm 0.017^o$
Spec 06	(Ge) Refractive index value -@5m, 7K	3.851 ± 0.001
Spec 07	(Ge) Refractive index homogeneity -@5m, 7K	$\Delta[n] < 10^{-5}$
Spec 08	(Ge) Flatness of the entrance face	λ / 30 (@ 633 nm) RMS
Spec 09	(Ge) Thickness of the prism	$7\,\text{mm} \pm 0.05\,\text{mm}$
Spec 10	(Ge) Output face angle	$-14.4830^o \pm 0.017^o$
Spec 11	(Ge) Flatness of the ouput face	λ / 30 (@ 633 nm) RMS
Spec 12	(Ge) Scratch / Dig requirement	60-40
Spec 13	(ZnS) Material is MultiSpectral Grade	
Spec 14	(ZnS) The optical requirements apply to the useful optical aperture taking into account the 3.8 % pupil shear	
Spec 15	(ZnS) Entrance face angle	$-22.3270^o \pm 0.017^o$
Spec 16	(ZnS) Refractive index value -@5m, 7K	2.208 ± 0.001
Spec 17	(ZnS) Refractive index homogeneity -@5m, 7K	$\Delta[n] < 10^{-5}$
Spec 18	(ZnS) Flatness of the entrance face	λ / 30 (@ 633 nm) RMS
Spec 19	(ZnS) Thickness of the prism	$13\,\text{mm} \pm 0.05\,\text{mm}$
Spec 20	(ZnS) Output face angle	$311.02687^o \pm 0.017^o$
Spec 21	(ZnS) Flatness of the ouput face	λ / 30 (@ 633 nm) RMS
Spec 23	(Ge) Positioning Δx, Δy	$\pm 100\,\mu$m
Spec 24	(Ge) Positioning Δz	$\pm 70\,\mu$m
Spec 25	(Ge) Positioning $\Delta\alpha$, $\Delta\beta$	± 1.6 arcmin
Spec 26	(Ge) Positioning $\Delta\gamma$	± 15 arcmin
Spec 27	(ZnS) Positioning Δx, Δy	$\pm 100\,\mu$m
Spec 28	(ZnS) Positioning Δz	$\pm 70\,\mu$m
Spec 29	(ZnS) Positioning $\Delta\alpha$, $\Delta\beta$	± 1.6 arcmin
Spec 30	(ZnS) Positioning $\Delta\gamma$	± 15 arcmin
Spec 31	(Holder) Positioning Δx, $\Delta y\,\Delta z$	$\pm 60\,\mu$m
Spec 32	(Holder) Positioning $\Delta\alpha$, $\Delta\beta$	± 30 arcmin
Spec 33	(Holder) Positioning $\Delta\gamma$	± 34 arcmin

Spec No.	Requirement Value
- - - - - - - - - -	
Spec 34	The material used for the AR coating shall avoid hygroscopic material and if possible radioactive material.
Spec 35	To avoid straylight, the useful area of the AR coating shall cover the whole optical apertures of the faces of the prisms with a margin of at least 300 μm.
Spec 36	A minimum transmission of 80% is required for the double prism at 7K between 5 μm - 10 μm
Spec 37	Below 5 μm, the specifications are driven by the straylight analysis
Spec 38	Above 14 μm, the transmission of the double prism shall be less than 10^{-4} to avoid straylight towards the detector unit
Spec 39	DPA components shall perform without permanent degradation after exposure to two times their mission Total Ionizing Dose
Spec 40	A material certificate of the prism materials will be delivered with the different models
Spec 41	The prisms holder will be made in aluminium alloy 6061 T6
Spec 42	A material certificate of the Aluminium will be delivered with the different models
Spec 43	The blank holder will be tempered between 77 K and 423 K
Spec 44	A description of this stabilisation treatment will be provided for CEA
Spec 45	The mass of the DPA shall be 69 g ± 20%
Spec 46	This mass will be measured for each model
Spec 47	The position DPA center of mass shall be determined by calculations
Spec 48	The DPA moments of inertia shall be determined by calculations
Spec 49	The Double Prism Assembly shall withstand a Quasi-Static Load of 200 g along each axis
Spec 50	The Double Prism Assembly shall have a first resonant frequency greater than 200 Hz.
Spec 51	The first resonant frequencies will be determined by Finite Element Analysis
Spec 52	A technical note containing the whole results of this analysis will be provided to CEA
Spec 53	The first resonant frequencies shall be checked by low level sine vibrations tests
Spec 54	The levels applied will be a constant acceleration of 0.5 g between 5 and 2000 Hz, with a sweep rate of 2 octaves per minute
Spec 55	The results of these vibration tests will be provided to CEA
Spec 56	Dynamic responses shall be determined by sine and random vibration tests
Spec 57	Random vibrations qualification will be performed with qualification levels (cf. spec 90)
Spec 58	The levels will applied along the 3 orthogonal axis of the DPA
Spec 59	Qualification test duration is 2 minutes
Spec 60	the heat conduction from the interface with the filterwheel to the prisms shall be as easy as possible
Spec 61	Conductive surfaces will be coated with Alodine 1200
Spec 62	Contact surfaces under bolts will be coated with Alodine 1200
Spec 63	Non operational temperatures range from 4 K to 364 K

Spec No.	Requirement	Value
- - - - - - - - - -		
Spec 64	Operational temperatures range from 6.85 K to 15.5 K	
Spec 65	10 thermal cycles between 6 and 313 K, minimum temperature rate of 20 K / hour	
Spec 66	The whole results of these thermal cycling tests will be provided to CEA	
Spec 67	The AR coated prisms have to work under vacuum at a temperature of 7K	
Spec 68	All non-contact surfaces of the holder shall be black anodized	
Spec 69	Diaphragms shall be implemented in the design of the holder	
Spec 70	Position of prisms wrt dowel pins	$\pm 100\,\mu$m
Spec 71	Position of prisms' bearing surfaces	$\pm 20\,\mu$m
Spec 72	Flatness of prisms' bearing surfaces	$\pm 5\,\mu$m
Spec 73	Angular position of the flat surface	$\pm 0.25^o$
Spec 74	Size and the shape of the hole in the filter wheel disk defined by UoC	
Spec 75	The fixation of the DPA on the wheel disk shall be ensured by 3 bolts	
Spec 76	The position of the 3 bolts is given in a CEA interface drawing	
Spec 77	The 3 fixation bolts will have a diameter of 4 mm	
Spec 78	The tightening torque of the 3 bolts will be calculated	
Spec 79	The alignment of the DPA shall be ensured by 2 pins with a diameter of 2 mm	
Spec 80	The pins will be mounted in interference fit in the wheel disk structure	
Spec 81	The position of the pins is given in a CEA interface drawing	
Spec 82	The holder will have corresponding holes,one circular, one oblong	
Spec 83	Bolts and pins are provided by CEA	
Spec 84	The position of the interface surface between the prism holder and the filter wheel disk is defined in a CEA interface drawing	
Spec 85	The roughness Ra of the interface surface shall be less than 1.6 μm	
Spec 86	Flatness of holder-filterwheel interface surfaces	$< 20\,\mu$m
Spec 87	The design of the Double Prism assembly shall respect the room available around the prisms	
Spec 88	The envelope available for the DPA will be described in a CEA interface drawing	
Spec 89	The DPA design shall respect the CEA Interface drawing	
Spec 90	The DPA design shall consider the design random vibration levels	

Definition of random vibration spectral densities

During the launch of the rocket, the burning of the fuel creates soundwaves which travel through the rocket and are responsible for creating vibrations. Initially, these random vibrations are only of low magnitude, but when transmitted to the satellite, each component starts vibrating itself, such that the subcomponents experience higher degrees of vibration. This is especially important for the LRSDPA, which is integrated into the filterwheel of the MIRI imager and

is the lowest order of sub-components. Due to the amplification through higher order sub components, and especially the flexibility of the filterwheel disk, the initial 3-4 gRMS of the rocket are amplified to *~50 gRMS at the level of the LRS-DPA*.

One important aspect of the requirements is that two of the above specifications define random vibration power spectra[5]. Specification 57 defines spectral density *qualification levels*, whereas specification 90 defines the *design levels*, cf. Figure 3.4. The reason for this is that the design levels have been established shortly before the demonstration model vibration test campaign, when the demonstration model already was manufactured. After surviving both lateral directions, the Ge prism broke during the axial direction random vibrations, demanding for a redesign. During the following non conformance review (Renotte et al. 2006), the board was convinced that a redesign of the LRSDPA alone was not enough and the levels had to be re-evaluated. To keep the schedule and not to produce a delay affecting the delivery of MIRI and eventually the schedule of the whole JWST, it was agreed that for the design-phase, the 'design levels' form the base for all calculations, whereas the (at that time not available) 'qualification levels' would be deduced from a close to final filterwheel design. For this procedure, the liability of the design levels was crucial - the final qualification levels must not exceed the design levels.[6]

3.3.2 Design Overview

Optical Design

The optical design of the MIRI imager, which includes the optical design of the LRSDPA, has been developed by CEA, i.e. Didier Dubreuil, Sebastien Poupar, Samuel Ronayette and Jerome Amiaux.

The great two advantages of the low resolution spectroscopy double prism assembly which motivated its implementation into JWST are that it

1. yields a very effective light-throughput and allows spectroscopy of *very* faint targets;

[5]The term *power spectral density* is historically driven, originating from times when accelerations were measured electronically and derived from the measured power. When looking at accelerations, the term *acceleration spectral density* is more accurate.
To derive peak levels of accelerations from random vibration spectral densities, a $3\,\sigma$ noise of the total gRMS value is considered. This means that with respect to the design levels, the LRSDPA will experience peak excitations of 166 g (!) within a 3σ probability.

[6]The European PI, Gillian Wright, took over the responsability for this (Wright 2007).

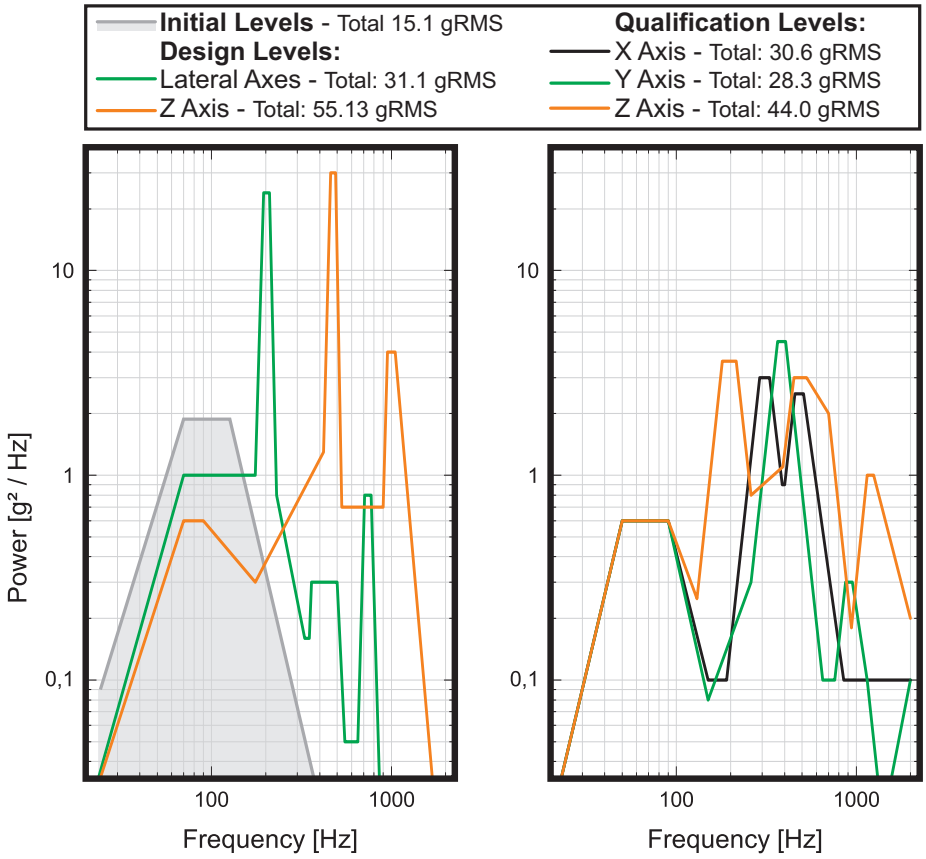

Figure 3.4: *Comparison between Design (left, according to specification 90) and Qualifiation (right, specification 57) random vibration power spectral density levels. The black and green colored lines represent excitation in the lateral axes of the LRSDPA, orange the vertical axis. For the qualification levels, the filterwheel has been notched (excitation has been cut off at certain frequencies) to protect the optical components, with the aim of resulting in the lowest possible excitation at the location of the LRSDPA. Hence the peaks containing most of the energy on the left have been reduced, which can be seen in the overall (integrated) power, which diminishes from 55.1 gRMS to 44.0 gRMS for the vertical excitation direction. The fact that the curves on the left and the corresponding curves on the right are not resembling each other much is not important for the LRSDPA, because in this frequency range, it behaves completely rigid (i.e. it has no Eigenfrequency). See Section 3.4.2 for results of the Qualification test campaign. In addition, the gray curve in the left diagram shows the initial levels for which the demonstration model had been designed (same excitation for all directions).*

2. provides spectral dispersion witout altering the beam angle what allows a similar treatment like a photometric filter, i.e. it can be implemented into an imager without the need for additional optics.

The use of a grism, although more compact, would lead to an unrealistically low number of grooves per mm to achieve the desired resolution (4 grooves per mm would be required). The optical layout of the low resolution spectroscoy mode is presented in Figure 3.5. The first of the two prisms is made of Germanium (Standard Grade), the second prism's material is Zinc Sulfide (Multi-Spectral Grade). Characteristic for both prisms is an extremely high refractive index in the mid infrared (at $\sim$ 50 K and 7.5 μm: $n_{Ge} = 3.92$, $n_{ZnS} = 2.22$ see Figure 3.6).[7] The diameter of the prisms are 23.4 mm (Ge) and 24.5 mm (ZnS). To reduce the amount of straylight in the spectrum, the two optical surfaces of each prism are coated with an antireflective coating optimized for the wavelength range from 5 μm - 10 μm. In addition, the optical design foresees diaphragms in the shape of the footprint of JWST's primary mirror on the front and exit faces of the prism. One of these diaphragms is completely sufficient, and in the LRSDPA this diaphragm is incorporated into the cover of the Ge prism. For sensitivity as well as straylight reasons, the surfaces of all mechanical parts are black anodized. The pixel scale of the resulting spectrum is roughly 28 pixels/μm. According to the Rayleigh criterion, which defines the minimum separation of two resolved spectral lines to the full width at half maximum (FWHM) of the line, the spectrum will show a resolution of 100 at 7.5 μm. This implies that the spectrum will be Nyquist sampled (2 pixels sample the FWHM). The sensitivity of the spectrometer aims at $0.6 \cdot 10^{-20}\, W/m^2$ for line flux and 1.35 μJy on the continuum flux (10σ detection after 10000s). The operating temperature of the double prism is, like the operating temperature of the whole MIRI instrument, $\sim$ 7 K.

Structural Concept

The goal of the structural design is to induce as little mechanical stress as possible into the optically active volume of the prisms, while poviding an accurate alignment. Therefore, a semi-kinematical mounting of the prisms via an interface-flange attached to the prisms is chosen. In particular, the design accomplishes that *under all appearing accelerations, the LRSDPA behaves completely rigid, i.e. no displacement of a prism (which would inevitably lead to its*

[7] However, a disadvantage of especially the ZnS crystal is a large spread of refractive inhomogeniety which claims much of the tolerance budget distribution of the requirements specifications (table 3.1).

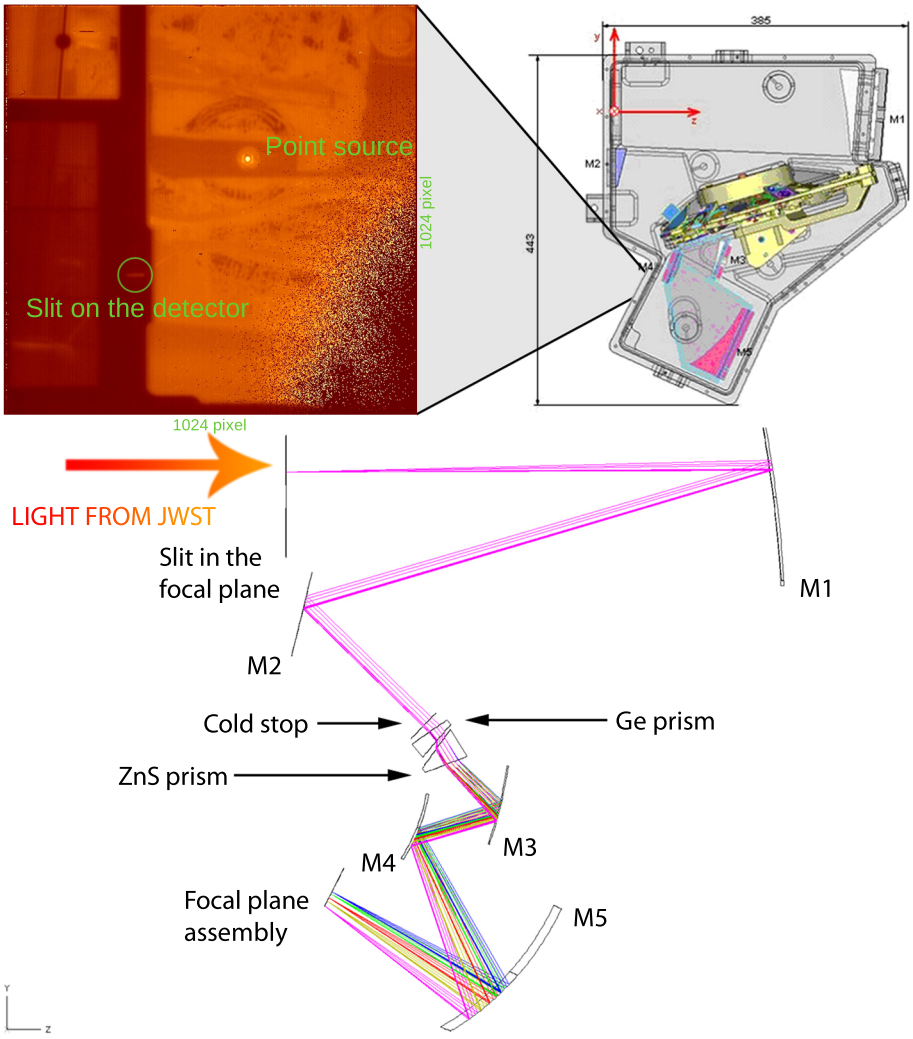

Figure 3.5: *Optical Layout of the MIRI LRS mode. The mid infrared light enters the imager from a pick of mirror through the LRS slit. After several reflections and collimation, the light enters the double prism assembly (entrance Ge prism, exit ZnS prism), gets spectrally dispersed, and after 3 more reflections is focussed onto the detector. Note that the double prism light dispersion does not alter the angle of the beam, what allows for an implementation into an imaging unit. On the top right, the imager CAD model with its filterwheel is shown in the same orientation. The top left displays a MIRIM VM raw frame (without background subtraction). The detector is illuminated by a point source, and the region of the LRS slit is indicated. The coronagraphy region is located to the left of the detector. The VM detector has a bad response at the bottom right corner.*

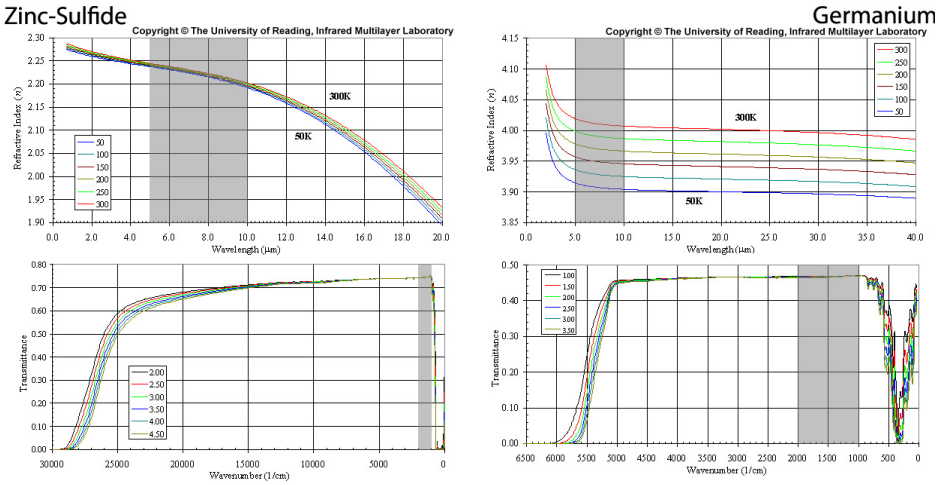

Figure 3.6: *Temperature dependent refractive index (top) and transmissivity curves (for different thicknesses, but at a temperature of 290 K, bottom) for the two prism materials Zinc Sulfide and Germanium. The LRS wavelength range is marked in gray. (Plots © by University of Reading, Infrared Multilayer Laboratory)*

destruction) occurs.

Figure 3.7 shows an exploded view of the LRSDPA. All individual components of the LRSDPA are shown in the order of their implementation. The structural concept is summarized as follows (any tolerancing is explained in detail in Section 3.3.4):

- The main mounting structure houses the two prisms and provides the interface to the filterwheel. The LRSDPA is attached to the filterwheel via 3 M3 hexagonal socket head screws (steel AISI 316 A4). The alignment is secured by two dowel pins in the filterwheel.

- Most components of the LRSDPA (with the exception of the prisms themselves, the screws, the springs and two gold-foils located on the prisms flanges) are made of Al 6061 T6. The Aluminium parts have been thermally tempered to improve the structural hardness prior to fine machining (cooled down to 77 K for >20 h, then cycled several times between 423 K and 290 K).

- The prisms' optical alignment is provided by the fit of the prism into the holder. No further manual adjustments / alignment are required.

- The two prisms each have a large flange attached to the optically active volume. The interface to the holder is completely realized using only this

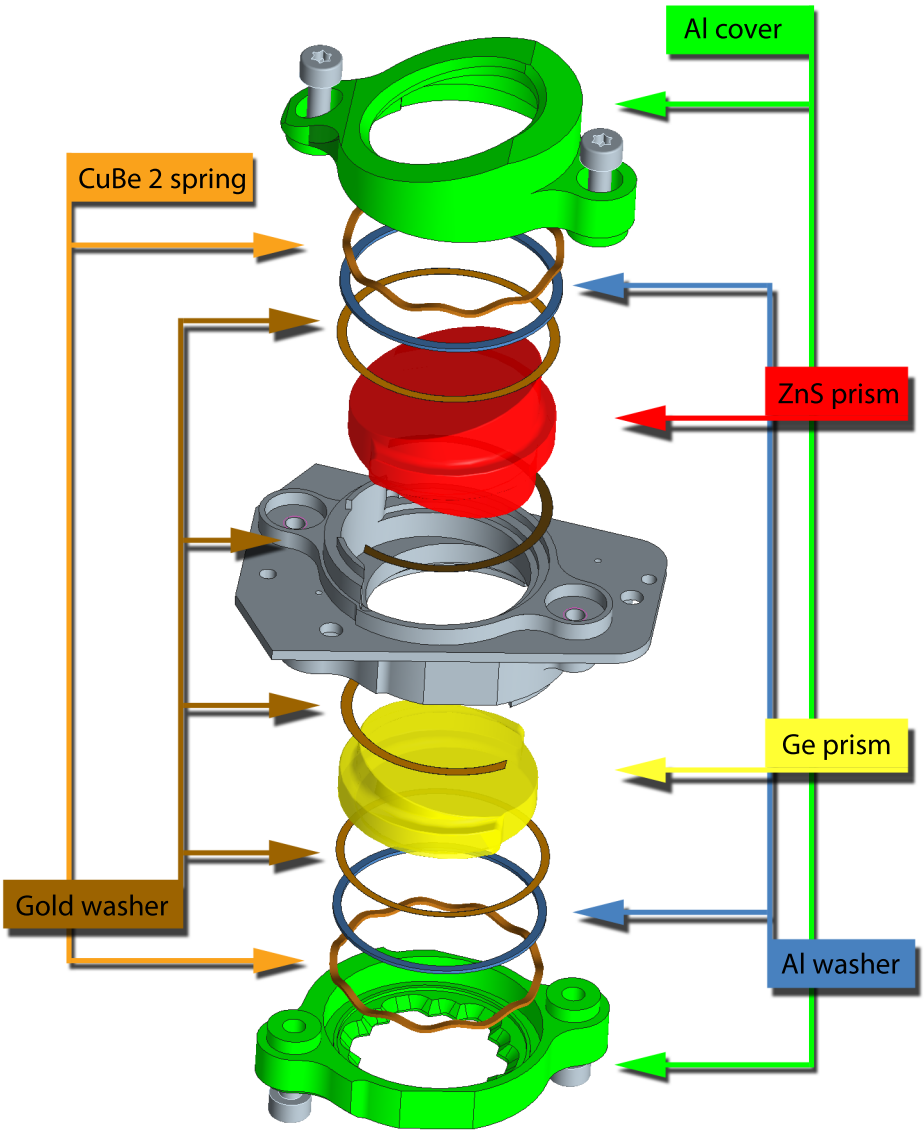

Figure 3.7: *An exploded view of the LRSDPA and its components.*

flange-area. In particular, the entrance and exit faces of the prisms are free from any contact.

- In order to avoid the creation of microcracks, which could propagate through the crystal during vibrations or thermal cycling, the surfaces of the prisms are lapped where this is feasible. This includes the flange and the main body of the prism (in fact, this is in contradiction to specification 02, but highly favorable to improve the prisms structural capabilities).

- A hard Aluminium-crystal contact is not desired. Gold foils with a thickness of 25 μm are placed on bottom and top of the prisms' interface flanges. Since the prism shape will be imprinted onto the Gold washers, the washers can be used only once. Should the LRSDPA be dismounted and reassembled, new washers have to be used.

- The semi-kinematical mounting is realized with one CuBe 2 ondulated spring per prism. The springs contract to a height of 1.5mm under their respective preload. The overall contraction is only $0.100\,\text{mm} \pm 0.05\,\text{mm}$.

- The spring compensates a quasistatic force of $3 \cdot 55$ g in axial direction directly. $3 \cdot 33.1$ g quasistatic forces in lateral directions are compensated via static friction. Since the prisms differ in size and mass, different springs for the Ge prism and the ZnS prism are needed.

- According to simulations, both prisms will survive the expected accelerations with a positive margin of safety > 2.4 (3.4 for the Ge prism, 3.8 for the ZnS prism, see Section 3.3.3).

- Due to the small available space, the springs have only 6 waves. In order to avoid point-loads induced onto the prisms, an Al6061 T6 washer (0.5mm thickness) is placed between prism and spring.

- To minimize straylight, diaphragms are needed at the outer surfaces of the prisms. A mask representing the beam (including pupil shear) is included in the cover of the Ge prism. On the exit surface of the ZnS prism, an elliptically shaped mask, surrounding the telescope footprint, is sufficient for the avoidance of straylight and allows for an technically easier manufacturing.

- The LRSDPA approaches the allowed outer envelope defined in [AD17] to a mimimum distance of 25 μm - with one exception: The LRSDPA inevitably exceeds its allocated envelope at one point on the ZnS side of the holder by 0.3mm. This protrusion has been accepted by CEA.

Table 3.2: *Material properties of the materials in use for the LRSDPA. Contraction refers to a cooldown from 290 K to 10 K and is given in per 10^4. Source: Database of material properties, www.matweb.com.*

Material	Density [g / cm^3]	Contraction (per 10^4)	Poisson Ratio	Young's Modulus [10^10 Pa]
Al6061 T6	2.71	41.4	0.3	6.89
Steel AISI 316 A4	7.8	30	0.29	21.50
CuBe 2	8.81		0.341	11.0
Ge std-grade	5.323	9.3	0.28	10.27
ZnS MS-grade	4.09	9.5	0.29	7.45

Material	Ultimate Tensile Strength [N / mm^2]	Specific Heat [J / g / K]	T. Conductivity [W / m / K]
Al6061 T6	430	0.964	180.07
Steel AISI 316 A4	580	0.500	16.3
CuBe 2	205	0.389	259
Ge std-grade	95±48	0.310	58.61
ZnS MS-grade	69	0.515	27.2

Based upon calculations, the mass of the LRSDPA is 75.9 g. The qualification model's mass has been measured to 75.3 g. Considering all manufacturing steps and tolerances, this is a very accurate result. Based upon calculations, the center of gravity is located at

$$(-0.17444, -151.02637, 91.85781)\,\text{mm}$$

with respect to the global MIRI imager coordinate system (Figure 3.5). Based upon calculations, the principal moments of inertia are

$$(8.5307, 12.2903, 12.87266)\,\text{kg/mm}^2.$$

Due to the compactness of the LRSDPA, its Eigenfrequencies are high. The simulations presented in Section 3.3.3 predict a first Eigenfrequency of the LRSDPA lies at a frequency of 6.04 kHz (Table 3.3). This is conform with the qualfication tests, where in a frequency-sweep from 20-2500 Hz, no Eigenfrequency has been found. For these calculations, I have made the assumption that the LRSDPA behaves as one rigid component, where no movement of any sub-part is allowed. As long as the excitation loads do not exceed the design loads, this assumption is reasonable. The mass participation factors given in table 3.3 provide an indication for the significance of the vibration. An Eigenmode with a high mass participation factor implies that the mode can readily be excited along that direction.

3.3.3 Geometric Elements Method Analyses

During the design phase, I studied the characteristic response of the two prisms to the expected maximum acceleration levels using the software *Pro/Mechanica*. The simulation technique applied by Pro/Mechanica is a geometric elements method simulation (GEM simulation). This means that convergence of the simulation is acquired by increasing the polynomial order of the mesh which represents the structural part (in contrast to finite model simulations, where convergence is achieved by decreasing the size and increasing the number of elements). Simulations of the complete LRSDPA in assembly-mode were too time-consuming and did not converge. Hence, the prisms are investigated individually.

Ultimate ambition of the design of the two prisms is that simulations verify the prisms' ability to withstand appearing accelerations and induced stresses by a safety factor of 2.4 concerning the ultimate stress limit (Astrium / ESA agreement).[8] The actual prisms are mounted using a spring which presses onto the prism's flange. For the GEM-study, this semi-kinematic mount has been idealized:

- The prism is constrained versus displacement in x- direction[9] via the underside of the prism's interface flange and in y- and z-direction via the vertical edge of the same flange.

- The required preload, which in reality is provided by the CuBe 2 spring, is applied axially onto the flange. According to the definition of the random vibration design levels (chapter 3.3), 55 gRMS in axial and 33.1 gRMS in radial direction must be expected. For the calculation of the preload of the spring, the following aspects are considered:

  - The radial fixation of the prism is accomplished via static friction, and here a conservative coefficient of static friction of $\mu = 0.25$ is used to represent the prism-goldfoil-Aluminium contact.[10]
  - A safety margin of an increased load of 10% is multiplied to the random levels.

[8] For optical materials, there is no general ECSS safety factor defined, here case-by-case margins have to be agreed upon. For comparison, ECSS-E-30, Part 3 suggests a saftey-factor of 1.5 concerning ultimate stress limits for any metallic materials used in mechanisms.

[9] For each prism, a dedicated coordinate system was used for the simulation. The x-axis of this coordinate system coincides with the generating axis of the prism's cylinder and the z-axis lies in the symmetry-plane of the prism.

[10] Since 33.1 gRMS / 0.25 > 55 gRMS, the *radial* random vibration levels are driving the preload of the spring!

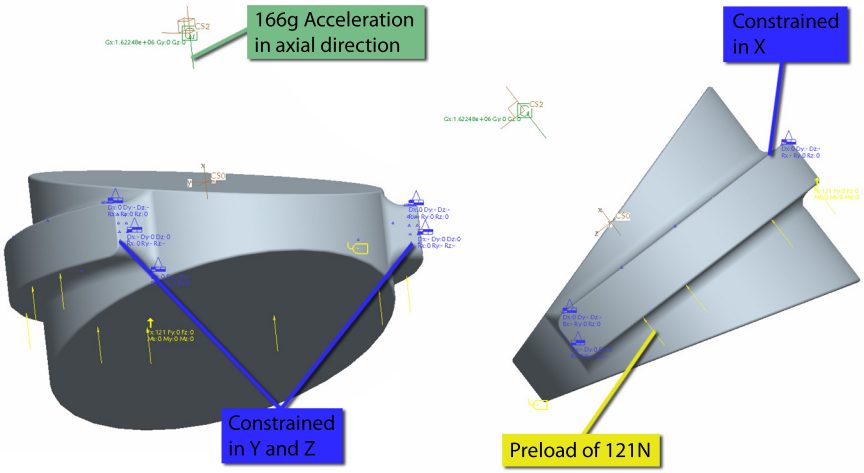

Figure 3.8: *The constraints and loads used in the GEM analysis of the ZnS prism to idealize the interface of the prism to the holder and the preload of the CuBe 2 spring.*

  - Due to manufacturing and tolerancing budget, only 85% of the preload are effectively mounting the prism.

  This leads to a preload of:.

$$F_{\text{preload}}[N] = \frac{33.13\,\text{gRMS} \cdot 3 \cdot 1.1}{\mu} \cdot \frac{1}{0.85} \cdot 9.81\,m/s^2 \cdot mass_{prism}\,[kg]$$

- In addition, 166 g (= 55.13 gRMS · 3) gravity are considered in axial direction.

In this way, preload and gravity are acting in the same direction, inducing the largest amounts of stress into the prisms (i.e. worst case study). For both prisms, convergence of the simulation was reached within 10% in the criteria of edge displacement, element strain energy, and global RMS stress. This is sufficient for a rough estimate of the prisms survivability during random vibrations. The maximum polynomial order for the simulations is 9 (see Figures 3.10 & 3.13).

The ZnS Prism's GEM Analysis

The weight of the ZnS prism is $24.4 \cdot 10^{-3}$ kg, which results in a preload of *121 N* for the ZnS prism. This preload is applied axially, in +X direction, onto

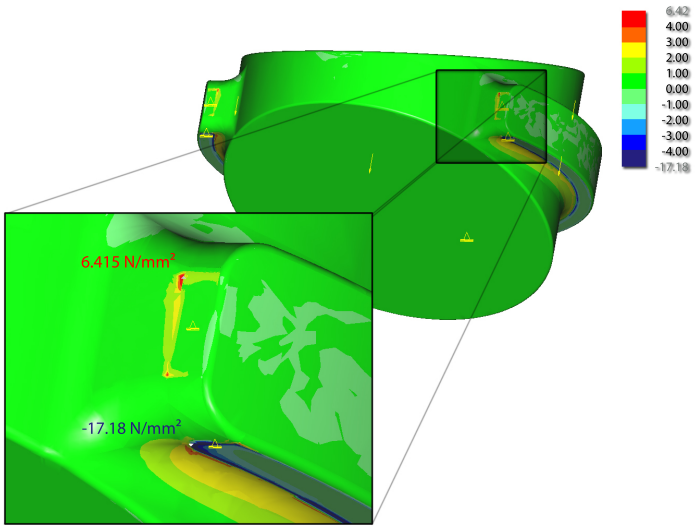

Figure 3.9: *The Maximum Principal Stresses are shown color coded in units of MPa. Highest levels of stress are located at the prism's flange, whereas the main body of the prism is kept free of stress. With respect to an ultimate tensile strength for ZnS of 68.9 MPa, the prism will survive the applied loads within a safety factor of 3.8.*

the bearing surface of the prism's flange that is in contact with the spring; 166g gravity are working in the same direction (Figure 3.8).

The ultimate tensile strength of ZnS multi spectral grade is *68.9 MPa*. The result in Figure 3.9 shows that the highest stress-values occur at the edge of the flanges surfaces which provide contact to the holder, near its front-edge. However, the maximum principle stresses do not exceed 18 MPa (maximum model value is 6.4 MPa, minimum model value is -17.2 MPa). According to this, the ZnS prism will survive the applied loads within a safety factor of 3.8 (a safety factor of the demanded 2.4 results in an effective stress limit of 28.7 MPa). The mesh and the polynomial order of the simulation are displayed in Figure 3.10.

The Ge Prism's GEM Analysis

The weight of the Ge prism is $18.6 \cdot 10^{-3}$ kg, which results in a preload of *86 N* for the Ge prism. The preload is applied axially, in +X direction, onto the bearing surface of the prism's flange that is in contact with the spring; 166g gravity are working in the same direction (Figure 3.11).

The ultimate tensile strength of Ge standard grade is (95 ± 16) MPa ($1\,\sigma$ error). To be conservative within a $3\,\sigma$ error, we consider an *ultimate tensile*

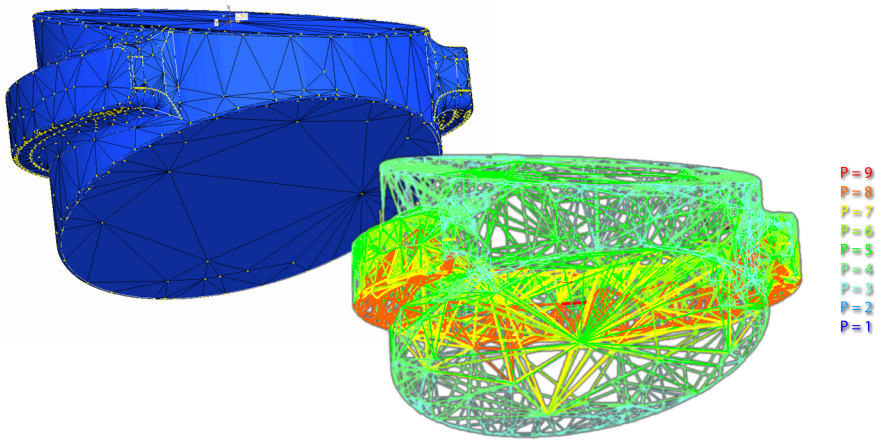

Figure 3.10: *The mesh and the according polynomial order of the ZnS GEM study are shown. The flange-area, where most of the stresses are concentrated, required the highest order of polynomial to achieve convergence.*

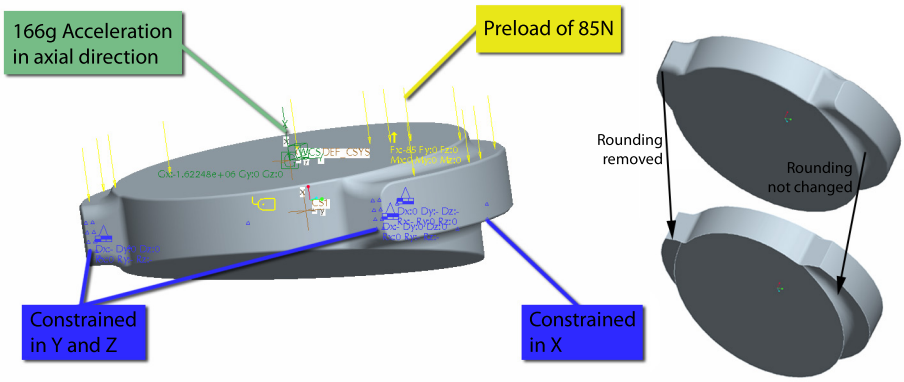

Figure 3.11: *The constraints and loads used in the GEM analysis of the Ge prism to idealize the interface of the prism to the holder and the preload of the CuBe 2 spring. On the right, the simplified prism model which is used to improve the convergence of the design study is shown. The large roundings at the front face of the flange have been removed. It was carefully paid attention not to artificially (and unrealistically) increase the contact surfaces of the flange. Only those surfaces are constrained/loaded which have contact in the model with included roundings. The actual stress distribution hence should be more uniform than the distribution presented in the results of this simulation.*

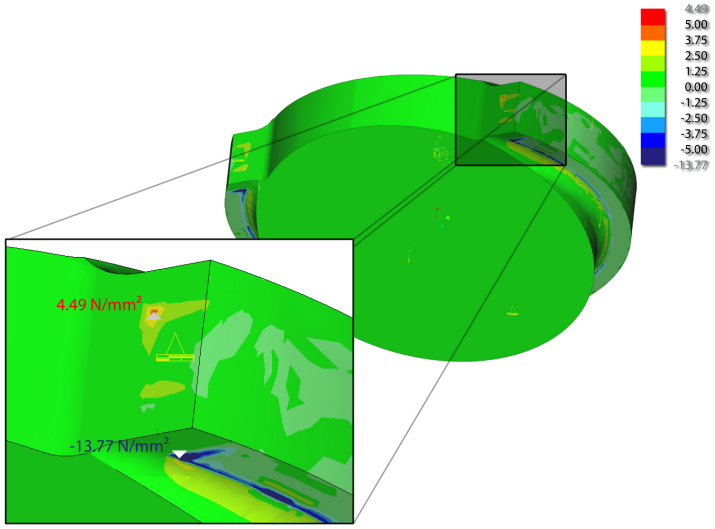

Figure 3.12: *The Maximum Principal Stresses are shown color coded in units of MPa. Similar to the ZnS prism analysis, highest concentrations of stress are located at the prism's flange, while the main body of the prism is kept free of stress. With respect to a 3 σ ultimate tensile strength for Ge of 47 MPa, the prism will survive the applied loads within a safety factor of 3.4.*

strength of 47 MPa. With a SF of 2.4, we aim at a stress limit for our study of 19.6 MPa. In Figure 7, the maximum principal stresses are shown. The stresses are distributed similar to the distribution in the ZnS prism, at the inner edge of the constrained contact areas (near the front face of the flange). The simulation geometry is somewhat idealized due to a rounding at the edge of the flange causing a singularity during the run (Figure 3.11). Hence, the real-life situation with rounded edges should have an even better stress distribution than the simulation shown here. The maximum principal stresses do not exceed a value of 14 MPa (model max. value is 4.5 MPa, model min.value is -13.8 MPa), equal to a safety factor of 3.4 with respect to the 3 σ ultimate tensile strength limit.

GEM analysis of the LRSDPA Eigenfrequencies

To be sure that no catastrophic excitation of the the LRSDPA in one of its Eigenfrequencies occurs, the Eigenfrequencies have to be simulated prior to any testing. For this simulation, it has been assumed that the complete LRSDPA behaves rigid, i.e. no individual movement of any part is allowed. This is reasonable as long as the design levels are not exceeded. The resulting first three Eigenfrequencies are presented in Table 3.3. The first Eigenfrequency only happens at

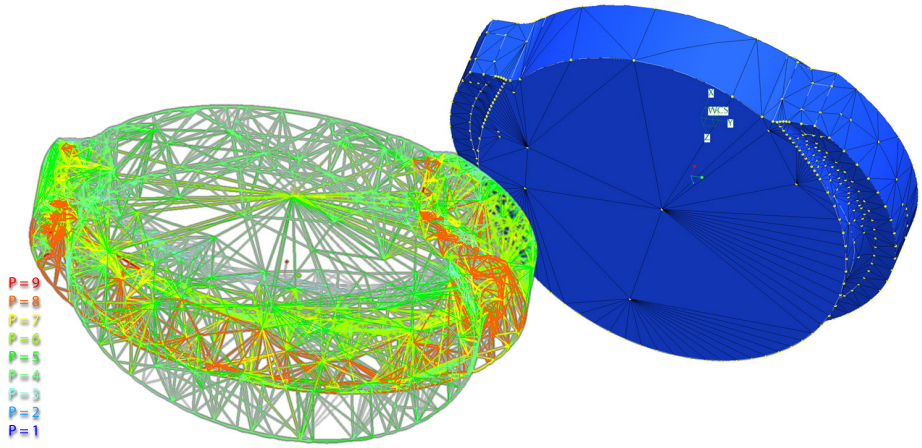

Figure 3.13: *The mesh and the according polynomial order of the Ge GEM study are shown. The flange-area, where most of the stresses are concentrated, required the highest order of polynomials to achieve convergence.*

a frequency > 6 kHz. Within the range where the filterwheel transmits significant amounts of accelerations (20-2000 Hz), no Eigenfrequency-excitation of the LRSDPA is expected.

3.3.4 Tolerancing

My design foresees that the requirements of positioning of the prisms are met just by integrating the prism into the holder, no further alignment of the prism is necessary (and possible). The positioning requirements are defined for cold conditions (8 K) of the LRSDPA. Since no metrology of the alignment of the

Table 3.3: *Modal Modes and Mass Participation Factors of the LRSDPA. Z is the vertical axis (along the prism generating axis, X and Y the lateral axes. From the mass participating factors, one can see that the 1st Eigenmode is an oscillation along the axial direction, whereas the 2nd and 3rd Eigenmodes are almost completely oscillating in the lateral direction.*

Eigen-mode	Frequency [kHz]	Participating mass factors X [%]	Y [%]	Z [%]
1	6.403	13.6	4.8	1.7
2	6.582	0.0	17.7	28.6
3	8.110	0.1	28.5	1.8

prisms in an assembled LRSDPA at can be achieved at cold conditions, it is important to prove that the strategy of radial alignment by design is in accordance with these requirements. How these requirements are realized is described in this chapter. I have performed the distribution of the tolerance budget between the different components in close communication with AMOS, the commercial supplier of the prisms, and the workshop of the 1st Institute of Physics. For most dimensions, the philosophy was to allow the manufacturing of the prism crystals to constrain the distribution of the tolerance budget, i.e. the larger budget is allocated to the prism manufacturing.

To meet the required *vertical* positioning accuracy of 0.07 mm, the holder provides a rigid contact to the prism (i.e. the prism's flange) with a respective bearing surface inside the holder. The holder's bearing surfaces are machined to a precision of 10 μm with respect to the dowel pin holes, which is the accuracy-limit that can be reached with the 5-axis CNC milling machine of the 1st Institute of Physics (UoC). The bearing surface of the prisms' interface flanges have a tolerance of 0.03mm with respect to its optical surface. Considering the flatness of the contact surfaces, 0.005 mm each, the prisms are placed in z-direction to an accuracy of ±0.05 mm. In *lateral* direction, the prisms are positioned against displacement via their cylindrical shape. The machining tolerances are calculated such that the positioning at 8 K fulfills the required $\pm\,0.100\,mm$ with an additional restriction that a warm prism still fits into a cold holder[11]. AMOS is able to machine the diameter of the prism up to an accuracy of $\phi\,^{+0.005}_{-0.020}$ mm, where the smaller upper limit again avoids the risk of a too small gap between holder and prism. This transfers to the tolerances for the respective hole of the Ge prism in the holder as follows (all dimensions are given in mm):

Warm			$\longleftrightarrow$	*Cold*
ϕ_{prism}	=	$23.400\,^{+0.005}_{-0.020}$	$\underset{\alpha_{Ge}\,@\,8\,K}{\longrightarrow}$	$\phi_{prism} = \begin{smallmatrix}23.365\\23.340\end{smallmatrix}$
				$\downarrow$
$\phi_{hole,max}$	=	23.596	$\underset{\alpha_{Al}\,@\,290\,K}{\longleftarrow}$	$\begin{cases}\Delta x = \Delta y = 0.100\\ \phi_{hole,max} = \phi_{prism,min} + \Delta x = 23.440\end{cases}$
$\phi_{hole,min}$	=	23.561	$\underset{\alpha_{Al}\,@\,290\,K}{\longleftarrow}$	$\phi_{hole,min} = \phi_{prism,warm\,max} = 23.405$

Analogous calculations for the ZnS prism lead to a respective hole with a diameter of $\phi_{hole} = 24.680\,^{+0.027}_{-0.012}$ mm.

The rotational movement around the axis of the prism (*roll*) is restricted by the front face of the prism's flange. Figure 3.14 displays a schematic view of the

[11] To avoid any risk of thermally induced stresses due to differential thermal expansion between the Aluminium holder and the prism materials.

worst possible alignment of the prism inside the respective hole in the holder. At ambient temperatures, the maximum gap between the two cylinders, including all machining tolerances and their respective worst case of combinations (e.g. smallest prism with largest hole), calculates for the ZnS prism to

$$\begin{aligned}\Delta x &= 8.012_{Al} - 7.980_{ZnS} + 0.5[(24.680 + 0.027)_{Al} - (24.50 - 0.02)_{ZnS}] \\ &= 0.1455\end{aligned}$$

and, corresponding to the nomenclature of Figure 3.14,

$a = 7.980;\ b = 28.9\,/\,2;\ c = 8.012 + 0.1455.$

This transfers, with a cooldown to a temperature of 8 K, to:

$$\begin{aligned}\Delta x &= 0.037 \\ a &= 7.9694;\ b = 28.861\,/\,2;\ c = 7.9952 \\ &\rightarrow \\ \alpha &= arcsin(a\,/\,b) = 33.5477^o \\ \gamma &= arcsin(c\,/\,b) - \alpha = 0.12^o\end{aligned}$$

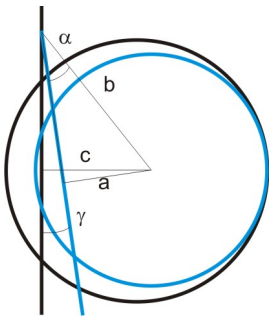

Figure 3.14: *Radial positioning. The worst case condition of positioning of the prism is shown (for rotation around z axis, z axis is perpendicular to view plane). Blue is the prism, black the holder.*

Similar calculations for the Ge prism result in a possible roll around its axis of $\gamma = 0.19^o$. Around the other two axes, the possible roll is easily calculated by the tangent of the flatness of the contact surfaces and the diameter of the prisms' flanges. Table 3.4 gives an overview over all positioning requirements and design positioning accuracies.

Besides the demand for high accuracy positioning, there is another critical aspect concerning the manufacturing tolerances. Taking all tolerances into account, the spring which mounts the prism onto the holder has to be contracted sufficiently. Otherwise, its purpose of fixing the prism against movement during launch vibrations, is not guaranteed, and with the enormous expected accelerations, any movement of a prism can eventually lead to the prism's destruction[12].

Still, this poses extremely high demands on the manufacturing accuracy.

[12] Although it seems that the current design of the prisms is indeed rather robust, and small amounts of movement do not critically affect the integrety of the prism, see chapter 3.4.2.

Table 3.4: *The required positioning accuracy is compared to the achieved accuracy by the design. These values are for cold conditions and hence cannot be verified through measurement at ambient temperatures. However, careful transfer of these requirements to ambient temperatures (see text for details) provides that metrology of the individual LRSDPA components (cf. chapter 3.4.1) can verify the compliance to the requirements. The positioning accuracy concerning roll α is a bit larger than the roll-accuracy concerning β, because the prism's flange is not fully closed.*

Description	Requirement	Achieved Accuracy Ge Prism	Achieved Accuracy ZnS Prism
$\Delta x,\ \Delta y$	$\pm 100\,\mu$m	$\pm 100\,\mu$m	$\pm 100\,\mu$m
Δz	$\pm 70\,\mu$m	$\pm 50\,\mu$m	$\pm 50\,\mu$m
$\Delta\alpha$	$\pm 0.027^o$	$\pm 0.021^o$	$\pm 0.020^o$
$\Delta\beta$	$\pm 0.027^o$	$\pm 0.026^o$	$\pm 0.026^o$
$\Delta\gamma$	$\pm 0.250^o$	$\pm 0.19^o$	$\pm 0.12^o$

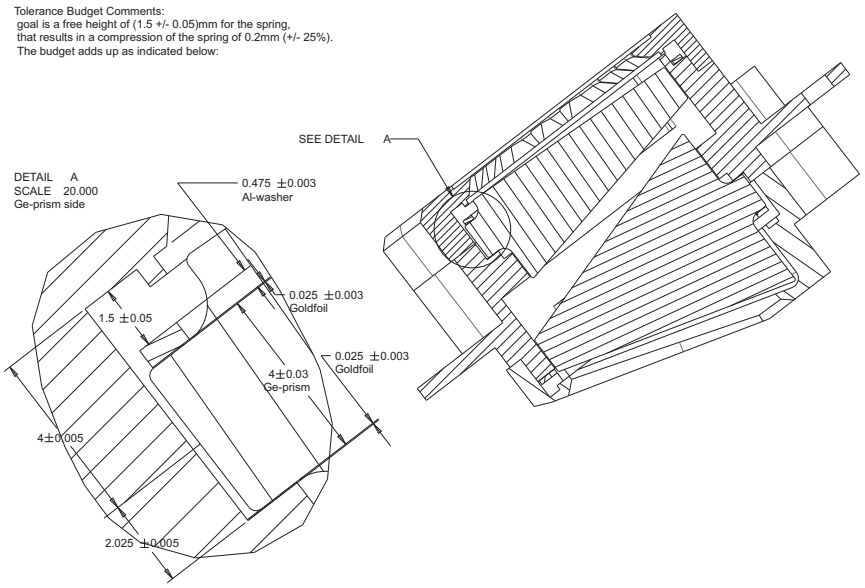

Figure 3.15: *The overall tolerance budget distribution for the (significant) vertical dimensions of all participating components are shown, exemplary for the Ge-prism (ZnS prism is analogous).*

3.4 Qualification Campaign

A lot of effort has been put into the qualification of the LRSDPA hardware. Alltogether, 4 different assemblys have been built and tested:

- the demonstration model (DM), which failed the vibration along the z-axis and demanded for a redesign in 2006. It was thermally and mechanically representative, but the prisms were neither coated nor polished, and all Aluminium parts were coated with Alodine1200 (i.e. no black coating);

- the qualification model (QM), which was the result of the above mentioned redesign. In contrast to the DM, here the prisms are polished to avoid microcracks, but still no antireflective coating is applied. The holder is partly covered with a black anodization and Alodine1200;

- the flight model (FM), which will be integrated into the satellite, and its identical counterpart, the flight spare (FS).

From a structural point of view, QM, FM and FS are all identical. Similar to the description of the design (Section 3.3), I will concentrate on the qualification of the final design, i.e. QM, FM and FS.

With the delivery of the LRSDPA to CEA, it has to be demonstrated that all specifications given in table 3.1 are fulfilled. In particular, this means that the manufacturing has to be evaluated, and it has to be verified that the LRSDPA will survive the launch and the cooldown of the satellite with vibration tests and thermal cycling between ambient and cryo temperatures (i.e 8 K). Further control of the performance of the LRSDPA is achieved with optical qualification. Figure 3.16 gives a schematic view of all qualification procedures provided with the LRSDPA assembly, integration and verification (AIV) test campaign.

The first spectrum of the low resolution mode is only provided along the MIRIM flight model tests. These tests are scheduled for the end of 2008 and cannot be presented here.

3.4.1 Manufacturing Verification

Crucial for the LRSDPA is that the different components meet their specified dimension limits. In this section, 3D metrology results of the 3 structural main components (two covers and a mount structure), and characteristic plots of the CuBe 2 springs of the LRSDPA are presented.

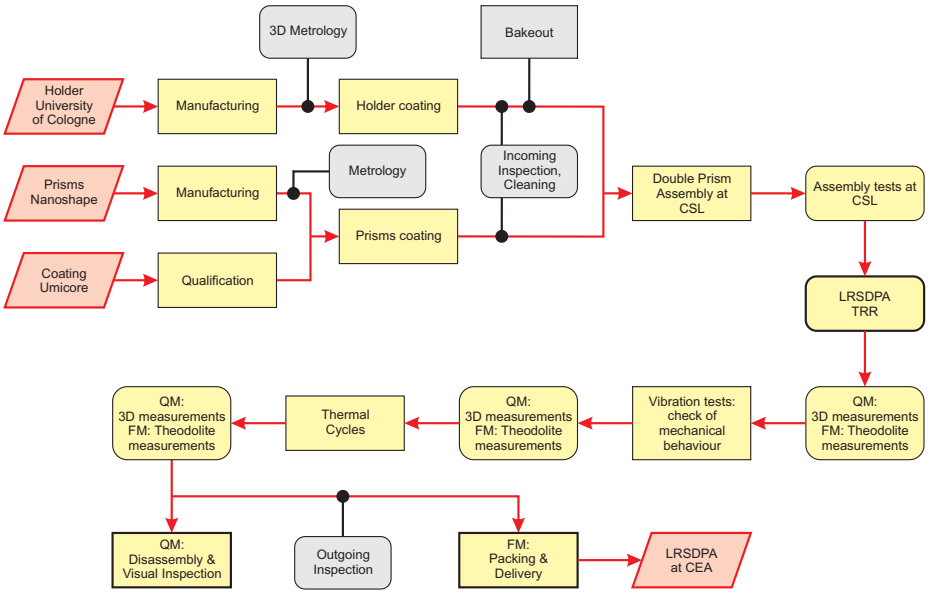

Figure 3.16: *Flowchart presenting the manufacturing, assembly, integration and verification (AIV) plan of the LRSDPA QM, FM & FS.*

3D Metrology

To achieve a machining precision of 5 μm on the complicated structure of the mount and covers, exceptional experience and manufacturing skills are required, in addition to a high precision 5-axis drilling machine. During all machining steps, metrology was obtained using a 0.75 mm rubin-ball head inside the same machine that was used to drill the parts from solid. Indeed, even though all machining steps were optimized to require as few manual intervenings as possible (in fact, the holder only had to be removed from the machine once), it was determined that even slight daily temperature-changes due to the surrounding ongoing work in the workshop caused uncontrollable manufacturing-defects and we decided to schedule the manufacturing work of the LRSDPA to night shifts and weekends.

However, to control the manufacturing accuracy and avoid systematic errors, it was necessary to obtain metrology in a way independent of our drilling machine. The detailed structures and small surfaces of the holder make ordinary metrology impossible. The only possibility to achieve a complete metrology of the Al parts of the LRSDPA was a 3D scanning. These measturements were performed at the *Institut für Bildsame Formgebung*, University of Aachen, using an ATHOS SO 3D camera system. The achieved measurement accuracy of this

type of metrology is of the order of 5 μm - 10 μm.

Alltogether, we produced 6 sets of LRSDPAs out of which the best 3 sets were selected for QM, FM and FS according to their metrology results.

Prior to the 3D measurements, the blank Al-part is covered with a thin layer of white charcoal (see Figure 3.17).[13] The part is mounted onto the Athos reference table, and a (time-variable) wireframe is projected onto the part. The part is photographed using a CCD camera-system. Afterwards, the images are electronically combined and a 3D model is reconstructed. This 3D model is compared to the nominal design via a 3D-CAD file (iges-files for holder, Ge-cover and ZnS-cover, files of 14-6-07).

It should be noted that the diameter of the M3 holes in the holder had to be increased after the metrology was achieved, in order to compensate for the tolerances of the respective holes in the filterwheel disk. Since the placement of the LRSDPA is ensured by the two dowel-pins, the change at such a late stage in development is not critical for the LRSDPA.

The model is referenced to the 3D-CAD file such that the accordance between both models is optimized (i.e. most surfaces show 0 discrepancy, see following figures). The values given in Table 3.5 represent averaged values over the corresponding surfaces. However, the flatness of the interface flunge represents the difference between minimum and maximum measured data. For the covers, only two dimensions are identified as critical for the design (Figure 3.18).

Only small differences in all 6 holders were determined. Especially the bearing surfaces of the prisms were of outstanding quality for all parts. The largest notable discrepancy between the different parts is the flatness of the interface flange. Accordingly, the selection of the models for QM, FM and FS were mostly based on the quality of the interface flange. The selection of the QM, FM and FS covers was mainly based upon a as flat interface surface to the holder as possible.

[13] In the course of the anodization process, the to-be-coated surface is roughened by a very agressive chemical attack which can affect a partial degradation of the accurateness of other surfaces. However, to avoid a contamination by charcoal, the metrology had to be performed on the blank Al parts, *before* the black anodization. Indeed, the bearing surfaces of the holders suffer from a partial roughening. There is no possibility, however, to determine the amount of this degradation. By hand correction under a microscope had to be applied to make sure that there are no peaks on these surface higher than 3 μm which could lead to a point load onto the prism's flange. Since the 3D metrology shows that the FM, QM and FS blank parts all are of equal quality (Table 3.5), the final selection of which part becomes QM, FM and FS, was decided upon the quality of the black anodization, with the best one being FM and the worst one being QM. Note that it appears that the quality of the anodization correlates with the wavefront error performance of the assembled prisms (Section 3.4.3).

Table 3.5: *Metrology results of the QM, FM and FS parts. The presented values represent averaged values over the corresponding surfaces,with the exception of the flatness of the interface flunge which represents the difference between minimum and maximum measured data. In case of a deviation to the nominal value that exceeds the tolerance margins, the deviation is still considered as not critical for the LRSDPA. The quality check of presented parts is considered as succesful.*

Dimension	Nominal	DM68011	DM68013	DM68015
Inner diameter (ZnS side)	$24.68^{+0.027}_{-0.012}$	24.68	24.68	24.70
x/y prism bearing surface (ZnS side)	8.05 ± 0.01	7.90/8.00	8.05/8.05	7.90/8.05
Z prism interface surface (ZnS side)	2.79 ± 0.02	2.79	2.79	2.78
Cover interface surface (ZnS side)	1.209 ± 0.005	1.21	1.21	1.21
Inner diameter (Ge side)	$23.58^{+0.016}_{-0.010}$	23.60	23.57	23.58
x/y prism bearing surface (Ge side)	8.55 ± 0.01	8.55/8.55	8.55/8.55	8.55/8.55
Z prism interface surface (Ge side)	5.98 ± 0.02	5.98	5.96	5.96
Cover interface surface (Ge side)	2.025 ± 0.005	2.02	2.02	2.02
Flatness of the interface flunge	0.02	0.01	0.02	0.03
	Nominal	ZNS066	ZNS068	ZNS069
Inner free height	4.820 ± 0.005	4.82	4.82	4.82
Height of sinks	Max 1.980	1.97	1.97	1.95/1.96
	Nominal	GE044	GE045	GE048
Inner free height	4.00 ± 0.005	4.00	3.99	4.00
Height of sinks	Max 1.980	1.95	1.95	1.94/1.95

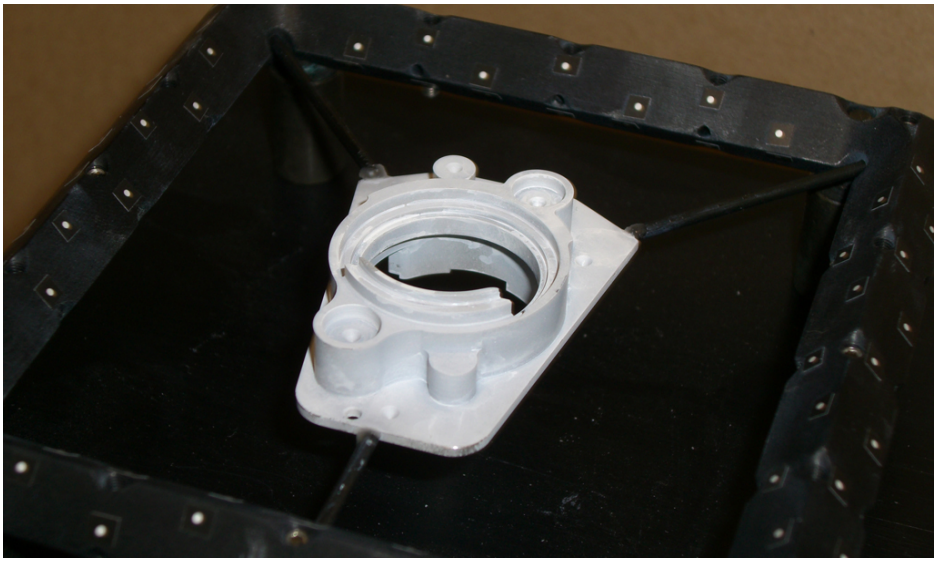

Figure 3.17: *Setup for the 3D metrology. A holder, covered with a thin layer of white charcoal, is mounted to the Athos Camera System. The white dots on the frame are used for referencing during the reconstruction of the 3D model.*

Spring Verification

Besides manufacturing errors in the production of the different parts, the most critical item of the LRSDPA concerning failure management is the performance of the springs mounting the prisms to the holder.

To avoid a qualification of the springs, the supplier provided us with certificates demonstrating that all springs are in accordance to their specifications. However, during the course of the QM vibration test campaign (Section 3.4.2, it showed that the springs in use were not providing the specified load, leading to a movement of the Ge prism during vibrations. Following this, a test setup was installed at the Ph1 workshop to verify the spring performance. It could be demonstrated that out of the batch of 10 springs we bought (5 springs per prism), only 2 springs were within the specifications.[14] Due to the time-pressure of the program, we decided to produce a demonstration batch of CuBe 2 springs in the local workshop of the institute. After the springs of this demonstration batch proved to be well conform with their requirements, ESA, Astrium, CSL and UoC jointly decided that the best solution was that UoC provides the springs

[14]This was either caused by a manufacturing error, or the springs changed in their performance due to handling. Since it was only decovered 1 year after the procurement, the source of the error was untracable.

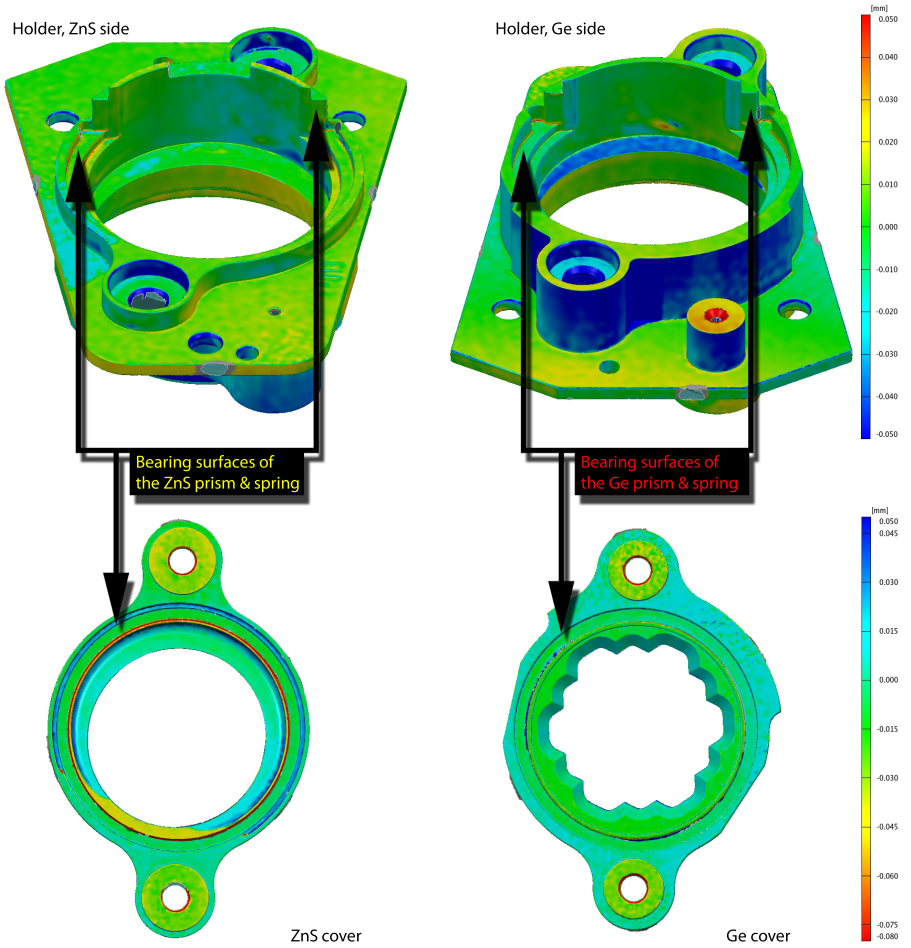

Figure 3.18: *Exemplary results of the 3D metrology of the holder (top) and the covers (bottom left: ZnS, right: Ge). Colour-coded is the deviation (in mm) between nominal 3D-file and the digitized actual part. In the case of the presented Ge cover (GE047), the deviation on the interface surface which provides the contact to the holder is ~ 20μm, hence it has been rejected for further usage. The presented holder and ZnS cover are among the sets delivered to CSL (DM68013, ZNS069). The thin layer of charcoal (Figure 3.17) can produce some unrealistic local results, such as the (red) spot in the top right view of the holder. The evaluation of such local deviations always was discussed with experienced personnel of the University of Aachen.*

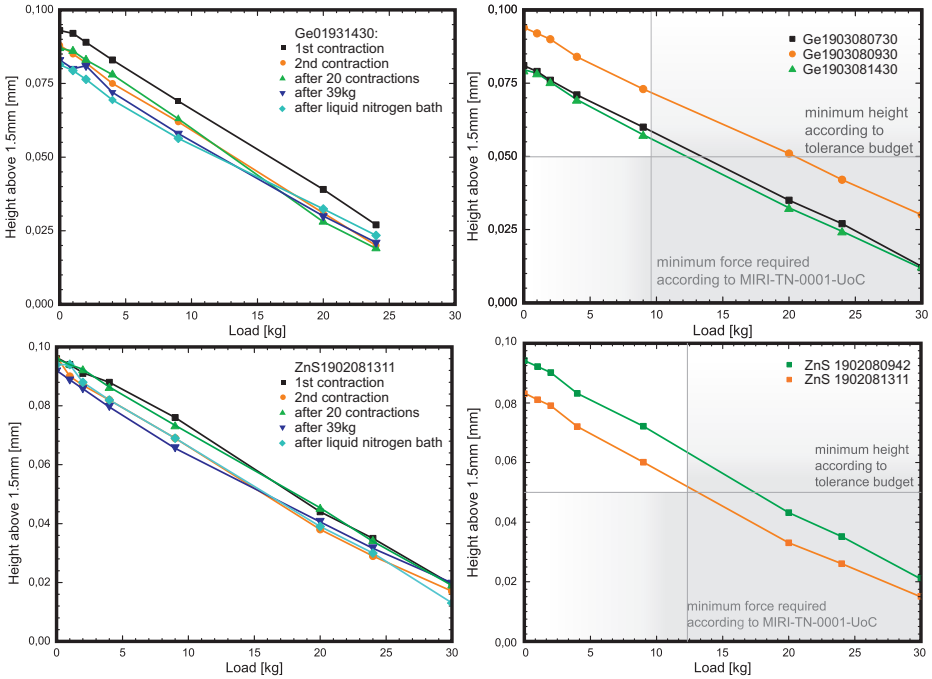

Figure 3.19: *Characteristic contraction-force diagrams. The diagrams on the left present the influences the different tests had on the springs (Ge spring on top, ZnS spring on bottom). After a first contraction to the nominal height of 1.5mm, one can see that, if any, only the shock-cooling with liquid nitrogen had a noticable effect on the performance. On the right, the final force contraction diagrams for the FM and FS springs are presented. The grey lines indicate the requirements the springs have to meet.*

for the LRSDPA themselves.

To evaluate the the newly produced springs, we conducted different tests that could affect the characteristic spring performance:

- Contraction of the spring to 1.500 mm;
- (Over-) Loading the spring with 39 kg for a time period > 1 day;
- Shock cooling the spring in liquid nitrogen.

Before and after all of these tests, characteristic diagrams of the springload as a function of compression were taken. After all these tests, the exact free height of the spring was adjusted by fine polishing. The interim and final characteristic diagrams are presented in Figure 3.19 and show that the change caused by the different tests is of minor degree and in particular the final springs all meet there requirements of the design and its tolerance budget.

3.4.2 Vibration Tests

Several vibration tests of the LRSDPA shall demonstrate that the LRSDPA will survive the launch of the satellite (qualification tests) and that the FM and FS are free of any defects (acceptance tests; specifications 53-59 in table 3.1). Hence, full vibration levels are always applied onto the LRSDPA QM, while -3 dB reduced levels are applied onto FM and FS.[15] In addition to the random vibration levels that are explained in Section 3.3.1, sine-vibrations, i.e. a sinusoidal accelerations from 20-100 Hz, with a sweep rate of 2 octaves per minute and an acceleration of 20 $g_{qualification}$ acceleration are applied onto the LRSDPA. Prior and following each vibration test, low level sine vibrations[16] monitor the characteristic acceleration response of the LRSDPA and should reveal any change in geometry of the LRSDPA. All of these tests are applied to the LRSDPA in its three main axes.

First QM vibration campaign

In February 08, the (first) qualification vibration test campaign was started. With the procurment of the QM prisms from AMOS, the LRSDPA was assembled by CSL staff in a class 100 cleanroom. After initial visual inspection, we mounted the LRSDPA via an interface plate onto the CSL shaker table (Figure 3.20) that is located in the large class 10000 CSL facility hall. Since the QM prisms are not coated, the QM is not fully optically representative and cleanliness is not an important issue. For the vibration campaign of FM and FS, however, a class 100 cleanroom is installed surrounding the shaker table. Due to our experience with the random vibration tests of the DM, we decided that it would be wise to do complete test sequences at reduced levels of -6 dB and -3 dB for a duration of 1 minute first. Although time consuming and therefore costy - the installation and setup of the shaker table had to be performed twice - the following problems proved it to be worth the effort. Starting with vibrations in Y-direction (see Figure 3.20 for definition of the axes), the first high-level sine vibrations were finished succesfull. However, during the first random vibration test, the sensors glued onto the holder were showing an unexpected response (Figure 3.21), with extremely high excitation in transeverse direction. *A direct vibration test at full*

[15] The dB values refer to the gRMS values. Random vibration acceleration spectral densities are given in power (i.e. amplitude squared), hence dB calculate to

$$\mathrm{dB}_{ab} = 10 \cdot \log_{10} \frac{G_a^2}{G_b^2}$$

[16] Sine sweep from 20 Hz - 2000 Hz with an acceleration of 0.5 g and 2 octaves per minute

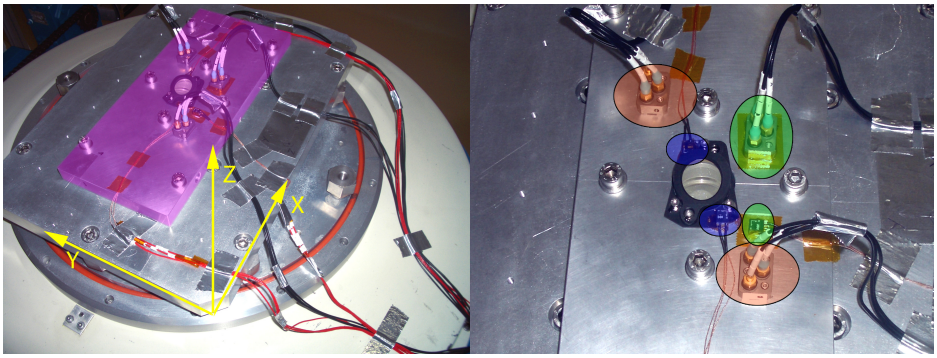

Figure 3.20: *The setup of the shaker table and the LRSDPA for the vibration tests. The images show the shaker table in its vertical (z axis) orientation. For horizontal vibrations, the shaker is turned 90°. No matter in which direction the vibrations are applied, the LRSDPA and all sensors remain fixed on the interface plate (pink in left image). The color-highlight on in the right image refers to the purpose of the individual sensors: Red marked sensors are used to control the input vibrations to the shaker in a closed loop; blue marked sensors are glued onto the LRSDPA in order to verify the vibrations the LRSDPA is 'seeing'; green marked sensors are used to monitor the reaction of the interface plate.*

levels would probably have destroyed the QM prisms already at this early stage, and the true reason of failure would never have been determined.

Nobody could think of any physical reason that would lead to such a strange, linear response of the LRSDPA, even the vibration experts at ESA and in the MIRI consortium were puzzled by these curves. It was concluded that the feedback had to be caused by malfunctio caused by the accelerometers.

However, CSL was offering extensive test time on their shaker table, and we decided to investigate the problem further. With more and more tests, we excluded malfunctioning sensors, interface problems between black coating and accelerometer or intrinsic holder response and isolated the root of the problem until only a problem with the LRSDPA itself was left open. After one week of tests, a disassembly of the LRSDPA immediately revealed that the LRSDPA was not correctly assembled. Besides traces of a jamming of the ZnS cover in the holder, like scratches and galling marks, too long screws were used to mount the ZnS cover onto the holder. In this way, the spring of the ZnS prism was not compressed up to its specification, and the applied accelerations caused the ZnS prism to move inside the LRSDPA. Figure 3.22 shows how severe these movements. A fine layer of ZnS-dust which was rubed off from the prism's main body and contaminated the holder completely. The prism itself, amazingly, showed only two small broken pieces at the prism's flange, indicating that indeed, the design of the prism is quite robust.

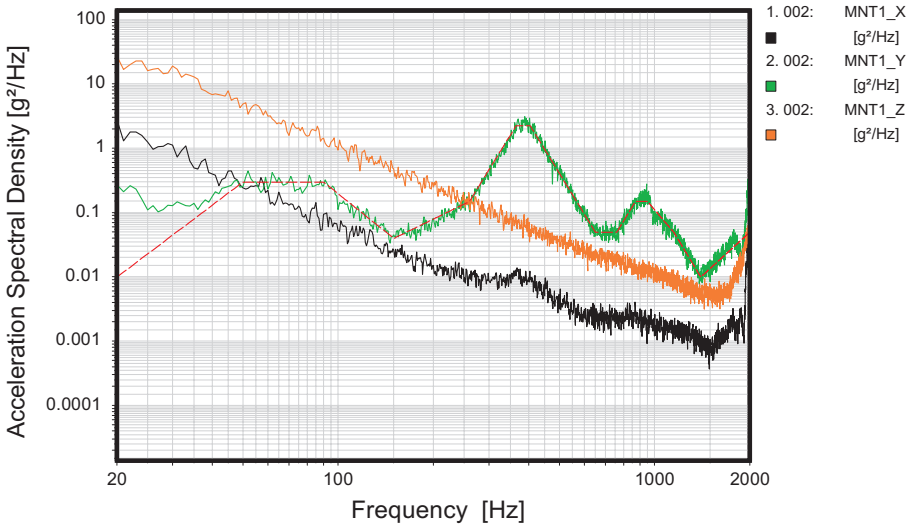

Figure 3.21: *The response measured by one of the two accelerometers glued onto the LRSDPA is shown. The excitation is applied in Y direction (Figure 3.20), at -3 dB with respect to the qualification levels. The red, dashed line represents the input excitation. The solid green line represents the in-axis response at the level of the LRSDPA. At high frequencies, the response follows the input excitation, while at low frequencies, the LRSDPA is exposed to an increased amount of vibrations. For the transverse directions, the response is almost linear; the response in vertical direction is even higher than the in-axis response! The amplification at low frequencies is neither caused by an Eigenfrequency of the LRSDPA in this frequency range (low level sine did not show any Eigenfrequencies between 5-2500 Hz, conform to the simulations), nor is it caused by the interface plate (the amplification is only seen by the two sensors glued onto the LRSDPA).*

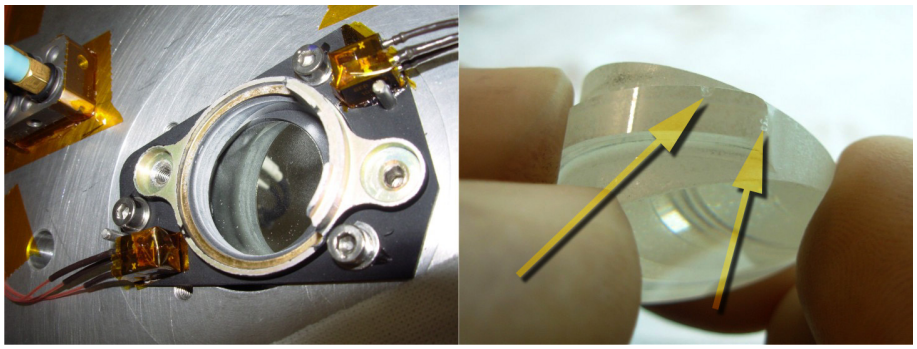

Figure 3.22: *The QM holder and ZnS prism after the initial random vibrations. On the left, the ZnS side of the holder is shown (the Ge prism can be seen at the bottom of the holder). White dust has contaminated the interior of the holder. Coarser dust grains can be spotted on the Ge surface. On the right, the arrows point to the two broken pieces at the ZnS prism's flange.*

In general, a lose part that is vibrated and hits another component is similar to a shock-excitation what causes an amplified excitation at *high* frequencies. In the beginning, this fact lead us to the conclusion that the linear, low-frequency amplified feedback of the accelerometers was unphysical, and we excluded the connection to a lose part inside the LRSDPA. However, it seems that the high-frequency vibrations caused by the moving prism simply overload the accelerometers.

In between all of these tests, metrology of the position of the prisms inside the holder was obtained at AMOS (cf. AIV plan, Figure 3.16). For this measurement, a feeler head sensor scans the surfaces of the prisms at several points. None of these measurements revealed a movement of the ZnS prism, hence we considered these measurements as futile and canceled them for the following tests. Since this was a contact measurement, it was not considered for the FM anyways.

Fortunately, both prisms were still intact and could be used to continue with the vibration test campaign. Yet, it was unclear if these tests did not introduce microcracks into the prisms which could lead to a failure in the following tests. An advantage of the QM ZnS prism, however, is that it is transparent at visible wavelengths, and no cracks could be spotted at visual inspection. Nevertheless, a possible failure would always have had to be interpreted in consideration of this overtesting.

QM vibration campaign, continued

After cleaning of all parts and production of new gold-foils (cf. Section 3.3.2), Damian Moratschke (lead technician of the LRSDPA efforts at the 1. Physikalische Institut) and I correctly re-assambled the LRSDPA QM. Vibration tests in X- and Y- direction were successful, both random and high level sine vibrations showed no indication of mis-behaviour. Successful high level sine vibrations in vertical direction were followed by reduced random vibrations, when, at -6 dB, the LRSDPA accelerometers showed a similar response to the first vibration tests (Figure 3.23). Now knowing that this indicates that something could be moving inside the LRSDPA, we immediately aborted the test. However, to clearify which prism was responsible for the anomaly, we removed the ZnS prism and performed a short vibration of holder + Ge prism. Since the characteristic signal remained, this time it was the Ge prism that was moving. Despite disassambly and a detailed inspection, no direct sign of movement of neither the ZnS nor the Ge prism could be spotted. Since the amount of transverse excitation was by orders of magnitudes lower than in the case of the ZnS prism, and with the experience that Ge crystal is a very fragile material, we concluded that there probably

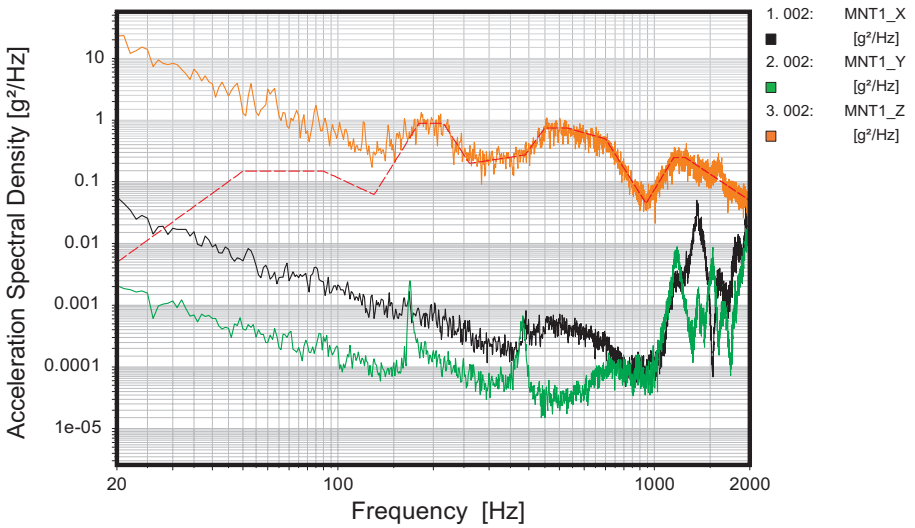

Figure 3.23: *The response measured by one of the two accelerometers glued onto the LRSDPA, during vertical excitation at - 6dB random vibrations, is shown. Color code is similar to Figure 3.21, only this time, Z-axis represents in-axis excitation. The behaviour at low frequencies is strikingly similar to that presented in Figure 3.21, only that the transverse directions are not completely dominated by the linear response.*

was a movement of the prism, but to a much lower degree than during the first run. The only possibility to allow for such a movement was that the springs did not deliver sufficient pressure to compensate for a movement.

Measurements of the force-contraction correlation of the springs in use indeed revealed that the springs (which had been procured by a commercial supplier) were not conform to their specifications. New springs were thus manufactured at the workshop of the 1st Institute of Physics (Section 3.4.1). Since we noticed that the interface plate of the shaker table had an Eigenfrequency at ca. 1980 Hz, we also produced a new, thicker interface plate (which would also be used during the FM acceptance tests). After a successful vibration test of the new springs with Aluminium dummy prisms[17], -3 dB random vibrations of the real prisms were performed. The outcome was successful, and qualification of the LRSDPA at full levels followed. Since the QM was dismounted beween the tests, we again performed a full qualification, with high level sine vibrations as well as vibrations in the horizontal directions. All tests were successful, i.e they

[17]It should be noted that we also vibrated the combination of these dummy-prisms together with the old springs, but it was not possible to reproduce the linear feedback of the accelerometers. The hardness of the prisms' crystals is much higher than that of Aluminium, probably the characteristic response is intrinsic to the holder-prism combination.

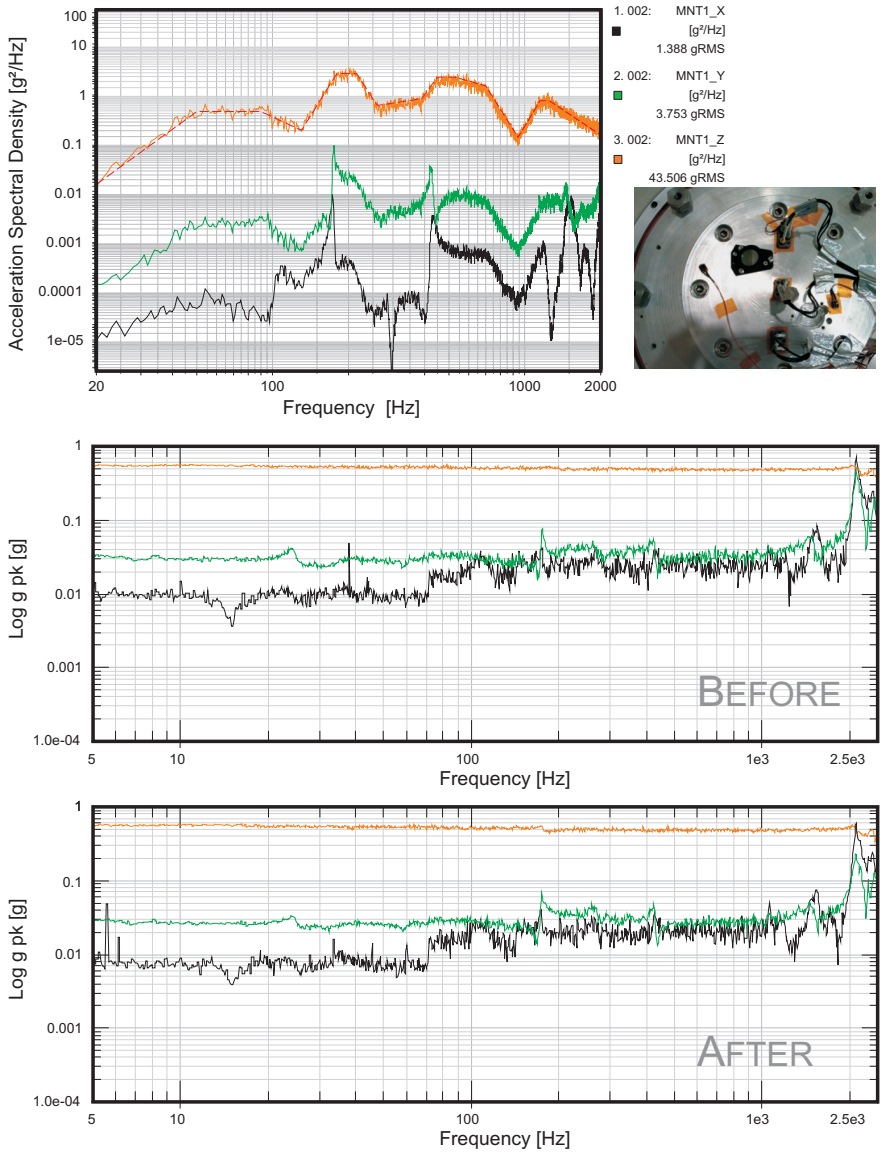

Figure 3.24: *Final, full level random vibrations of the QM in vertical direction. The top diagram displays, similar to Figure 3.23, the acceleration power spectral density. The in axis excitation matches the input excitation perfectly, and the excitation in transverse direction is not significant (cf. integrated gRMS values). In addition, the response to low level (0.5 g) sine vibration in Z-direction are presented; the curves in the middle diagram have been taken before, in the bottom diagram after the random vibrations. The accelerometers on the interface plate show identical features in transverse direction, what implies a correlation to the control of the shaker table. The random vibrations caused no significant changes. The photo on the top right hand side shows the setup with the new interface plate (mounted to the shaker via 8 M10 bolts).*

did not show any unexpected feedback (cf. Figure 3.24, and from the outside view, the prisms were still intact. Final success was pending on the final detailed inspection. In order not to interfere with the flight representative test campaign, a disassembly of the QM is only possible after the thermal cycling. The final disassembly after these cryogenic tests revealed that the prisms were completely intact, no additional broken pieces, and no dust contaminated the LRSDPA. This was of particular interest, because dust can have significant impact on the optical performance of the LRSDPA, and in a worst case scenario could even contaminate the whole MIRI instrument.

The vibration test campaign of the FM at acceptance level (i.e. all test levels are reduced by 3 dB) was successfully completed on the 20th of May 2008, without any problem.[18]

3.4.3 Optical Tests

Two optical measurements of the LRSDPA have been performed in order to characterize the alignment of the prisms and the wave front error (WFE) of the prisms' outer optical surfaces. Since these measurements have been carried out in the assembled state, no information on the two optical surfaces inside the holder can be obtained. All measurements have been performed before and after the vibration tests to monitor any significant impact on the optical performance.

The alignment has been evaluated using theodolyte measurements. Three theodolytes have been used simultaneously in order to be able to measure the angles of the prisms with respect to each other directly. The results are presented in Table 3.6. It showed that the measurements with respect to the interface structure were depending on the process of assembly of the LRSDPA onto the interface, hence these values have a larger uncertainty than the actual measurement error suggests. The alignment of the QM prisms is largely out of its specifications. This is probably caused by

- the worst quality prisms out of the batch of prisms produced (although each prism alone meets its requirements);
- the bad quality of the bearing surfaces of the holder which were attacked strongly by the black anodization;
- the excessive overtesting of the QM due to the several vibration campaigns with moving prisms.

[18] After the QM vibration test campaign, which took more than 1.5 months, the full sequence of the FM test campaign was finished in 1 day.

Table 3.6: *Theodolyte measurements of the angles of the prisms, assembled in the holder. The values are given for before and after the* final *vibration sequence. The most important value is the alignment of the Ge-surface with respect to (WRT) the ZnS-surface (ZnS-Ge), since values given with respect to the interface are highly dependant on the process of assembly onto the interface. The QM is largely out of the specifications, which is probably caused by a combination of the quality of the prisms, the quality of the bearing surfaces of the holder, and the many vibration tests of the QM (see text for details). For the FM, the alignment of the two prisms with respect to each other meets the requirement within 2". The requirements, are given for 8 K, while the measurements are performed at ambient temperatures. The design foresees that the final alignment is achieved due to the shrinkage caused by the cooldown. The vibrations do not have any influence on the positioning.*

Model	WRT	before vibrations	after vibrations	requirements
QM	Ge-If	2°44'49"±1"	2°44'42"±3"	2°44'02"±1'
	ZnS-If	16°39'52"±6"	16°39'50"±1"	16°39'52"±1'
	ZnS-Ge	13°55'03"±6"	13°55'07"±3"	13°53'24"±2'
FM	Ge-If	2°45'31"±2"	2°45'38"±3"	2°44'02"±1'
	ZnS-If	16°38'53"±3"	16°39'01"±2"	16°39'52"±1'
	ZnS-Ge	13°53'22"±4"	13°53'23"±4"	13°53'24"±2'

The WFE of the prisms has been evaluated using a fizeau phase shift interferometer. The reconstructed height profiles of the QM prisms are shown in Figure 3.25, the corresponding RMS values are presented in Table 3.7. The QM Ge prism's wave front error is completely out of the specification. Obviously, the above mentioned problems of the QM affect the wave front of the Ge prism extremely. The WFE of the ZnS prism, on the other hand, is not severley degraded, the RMS value of ~30 nm is similar to the values of the FM. Knowing of the QM Ge prism values, we took intermediate WFE measurements of the FM during its assembly, with a gap between the covers and the holder of 0.05mm. For both prisms, a RMS value of 18-20 nm was obtained, what means that the deformation of the wavefront is caused in part by the pressure wo which the prism is exposed to by the spring (the GEM analyses of the prisms that I performed using Pro/Mechanica are not sensitive enough to evaluate a deformation on nm-scales, so the deformation could not be cross-checked with simulations). However, the 30 nm RMS obtained for the FM have been (at the time of writing of this thesis still unofficially) agreed to by CEA, the official request for a waiver has been raised.

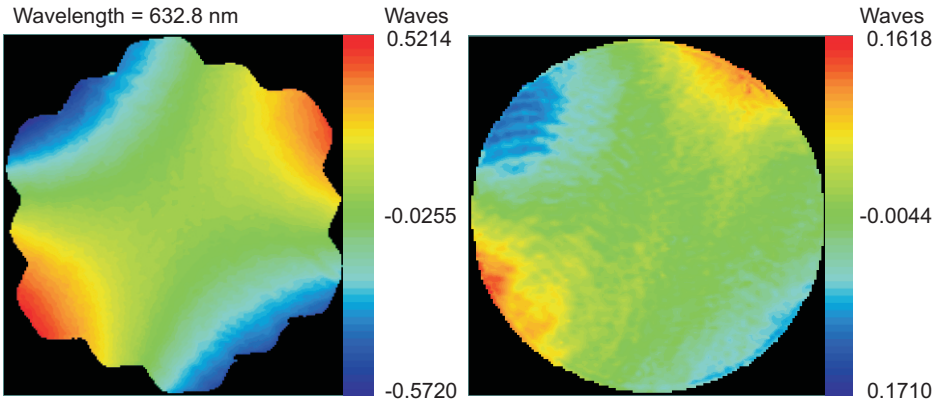

Figure 3.25: *Reconstructed wave front errors from fizeau phaseshift interferometer measurements of the QM prisms, assembled in the holder. The Ge prism's wave front error is shown on the left, ZnS on the right. The symmetric structure in the deformation suggests a relation of the deviation to the mount. Important is the RMS value in these images. Results are presented in Table 3.7.*

Table 3.7: *Fizeau phaseshift interferometer measurements of the prisms, assembled in the holder. The RMS values have an error of about ± 3 nm. The QM Ge prism is largely out of specs, probably due to similar reasons as mentioned in Table 3.6. However, the effect is definitely related to the force of the spring pressing onto the prism, as intermediate measurements during the assembly revealed. The situation for the FM is much better, but still out of the specified 21 nm. A waiver has been raised to CEA to increase this margin and is awaiting final approval.*

Model	surface	before vibrations	after vibrations	requirements
QM	Ge input optical surface	RMS = 118 nm	RMS = 133.8 nm	21 nm
	ZnS output optical surface	RMS =30.3 nm	RMS = 29.5 nm	21 nm
FM	Ge input optical surface	RMS = 31.1 nm	RMS = 35.1 nm	21 nm
	ZnS output optical surface	RMS =30.8 nm	RMS = 26.3 nm	21 nm

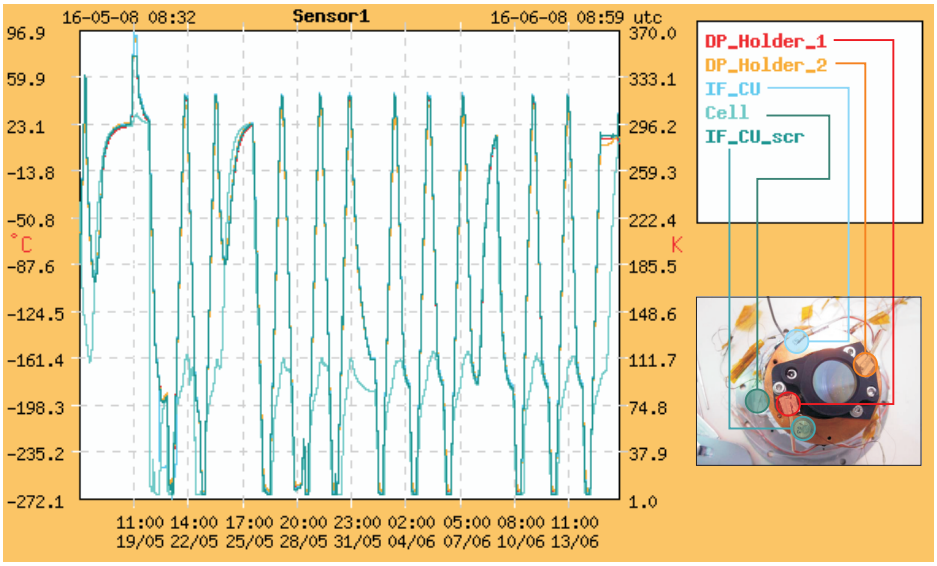

Figure 3.26: *Qualfication thermal cycles. The QM has been thermally cycled 10 times continuously between 300 K and 6 K. On the bottom right, the setup with the LRSDPA mounted onto a Copper-interface and the location of the 5 temperature sensors is shown. The FM was exposed to only 2 cycles, but with the same cooldown rates and temperature limits.*

3.4.4 Cryo Tests

Cryo tests shall demonstrate that the LRSDPA will survive the cooldown of the telescope to its operating temperature of 8 K (MIRI operating temperature).

For the qualification campaign of the LRSDPA, 7 thermal cycles between 313 K to 6 K have been performed. For the FM, the acceptance test consists of only 2 cycles.[19] The minimum rate of temperarture change for these tests is 20 K/h (i.e. it is allowed to cool down faster, but not slower to provide in-space representative conditions). The only success criterium for the thermal cycles is that the prisms remain intact. Figure 3.26 shows the thermal cycles the QM has been exposed to.

The final disassembly of the QM after the cryo tests showed that both prisms were completely unharmed, no dust was found inside the mount (c.f. Figure 3.22) and therewith the qualification campaign was successfully finished.

[19] After delivery to CEA, the LRSDPA FM will be exposed to 14 more thermal cycles in the course of the continued acceptance tests at filterwheel-, imager-, MIRI optical system-, MIRI- and JWST-level.

Part II

Host galaxies of active galactic nuclei in the near infrared

CHAPTER 4

Host Galaxies of Active Galactic Nuclei

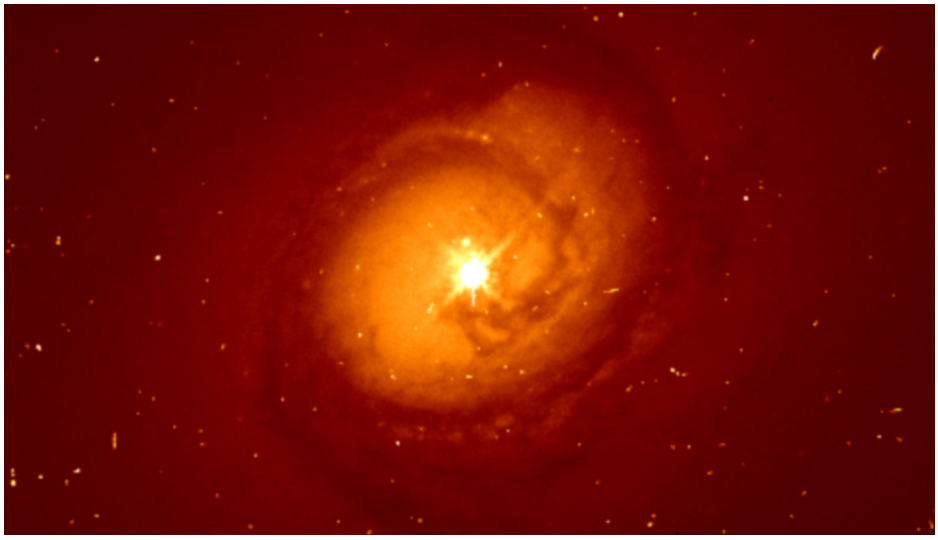

Figure 4.1: *Hubble ACS image of HE 1237-0504, a prominent source of the nearby/borderline QSO sample. Data from the ESO Science Archive Facility.*

One of the major achievements in astrophysics of the last years is the realization that every galaxy with substantial bulge-component harbors a massive black hole in its core. In principle, this makes every center of such galaxies a potential active galactic nucleus. However, the majority of these nuclei exhibit a low luminosity or almost no activity at all.

Although the detailed physics of AGN-evolution are still unclear, several links between galaxy and QSO-evolution have been revealed.[20] Early in the field of AGN-studies, the idea that interaction can trigger the AGN activity was suggested. There are indications to an evolutionary scenario from ULIRGs to QSOs (Sanders et al. 1988), in which strong interaction between galaxies is responsible for gas-infall towards the nuclear region and the ignition of the AGN. But observations of QSOs and their host galaxies remain, even with most modern tele-

[20] A brief overview over the taxonomy of active galaxies is presented in the glossary.

scopes, challenging. While the cores of AGNs/QSOs at redshifts z > 1 have been subject to several studies, revealing e.g. luminous accretion onto (super) massive black holes, disentangling host properties from the strong nuclear emission has shown to be problematic for the more distant QSOs and Seyfert galaxies. Hence, the importance of interaction for the activity-phenomenon in general is still a hot topic, with contradictory results from different studies. The determination of host properties and their connection to the AGN phenomenon is thus easier accomplished by studying QSOs in the nearby universe, where hosts can be observed spatially resolved. But the fraction of galaxies that produce QSO-level activity in the local universe is only 0.1 percent. Due to the small number of QSOs and luminous Seyfert galaxies in the nearby universe (e.g. the closest QSO-classified object in the SDSS has a redshift of 0.078), there have not yet been reported any systematic studies on a significantly large and complete sample of nearby QSOs without selection biases which would allow extrapolations on the further distant QSO-population. Jahnke et al. (2004) analyzed multicolor data (*BVRi*, *JHK*) of 19 low redshift (z<0.2) QSO hosts using various ground based telescopes. They found that the disk dominated host galaxies show colors similar to average colors of inactive galaxies of the same type, whereas bulge dominated host galaxies appear significantly bluer in *V*-*K* than their inactive counterparts and similar blue as the dis dominated hosts, suggesting a connection between galaxy interaction, induced star formation and nuclear activity. Dunlop et al. (2003) on the other hand deduced from extensive Hubble Space Telescope data on 33 radio-selected galaxies/QSOs at 0.1 < z < 0.25 that interaction does not play a significant role and denies a ULIRG-QSO evolution.

In order to study host galaxy properties of QSOs, we created a sample selected from an extended list of the Hamburg/ESO Survey (HES: e.g. Reimers et al. 1996; Wisotzki et al. 1996, 2000). [21] The only selection scheme for our sample was their small cosmological distance: only objects with z < 0.06 were chosen. This limit grants an observability of the prominent CO(2-0) stellar (rotational-vibrational) absorption band in the *K*-band.

Many other QSO samples (e.g. PG Bright Quasar Survey, 10k catalog, 2dF QSO Redshift Survey) apply a 'point-like morphology' selection onto their QSO identification routines, resulting in a significant incompleteness at low redshifts. HES does not discriminate against extended objects and hence shows a high volume density of luminous type I AGN at low cosmological distances, i.e. HES builds a good foundation for the study of nearby QSOs.

[21] HES is a wide angle survey for optically bright QSOs, with a well defined flux limit of $B_J < 17.3$, varying from field to field, and a redshift coverage of $0 < z < 3.2$. QSO candidates were identified in digitized objective prism plate data by applying color- and spectral feature based selection criteria.

In the redshift volume of $0.01 < z < 0.06$, a total of 99 objects can be found in the HES catalog. These sources build our nearby QSO sample and represent some of the closest known QSOs for which detailed astrophysical studies (i.e. spatially resolved imaging and spectroscopy) of the host galaxies' physical properties are still possible. It clearly probes the lower luminosity QSO population ($-18 < M_B < -23$, hence the nomenclature 'borderline QSOs'), but it is remarkably different from local Seyfert galaxies and more luminous PG QSOs, as our studies of the molecular gas content revealed (Bertram et al. 2007).

Due to its redshift limit, this sample is intrinsically well suited for studies in the near infrared. In the following chapters, I present near infrared observations of some of these sources. In Chapter 5, results from K-band slit spectroscopy and seeing limited JHK imaging are shown. This chapter is based upon the results published in Fischer et al. (2006b) and Fischer et al. (2006a). In Chapter 6, I discuss in detail near infrared integral field data of HE 0036-5133, a source that is also selected from the nearby/borderline QSO sample (paper in prep.).

Throughout this thesis, I use H_0=75 km s^{-1} Mpc^{-1} and a flat universe with Ω_M=0.3, Ω_{vac}=0.

CHAPTER 5

ISAAC's view on nearby borderline QSOs

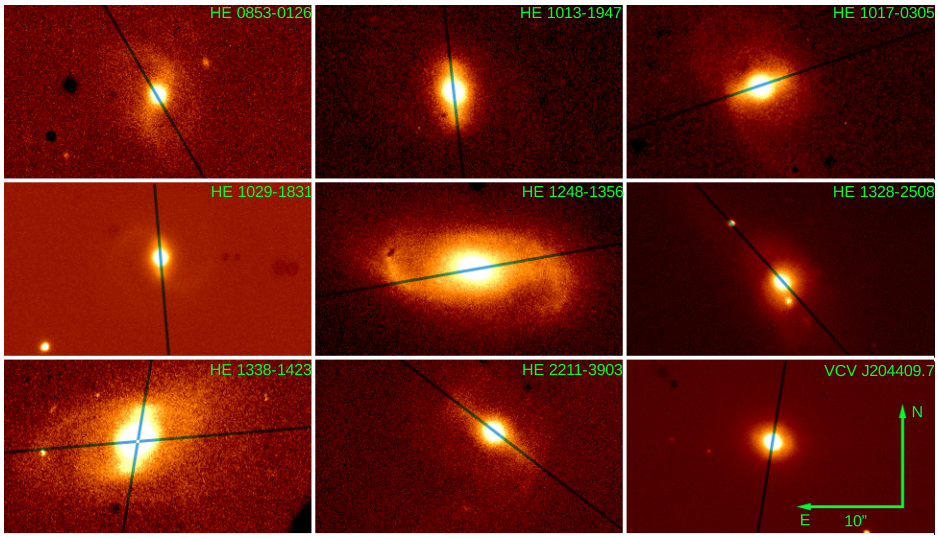

Figure 5.1: *The ISAAC H-band images of the 9 observed AGN. Additionally indicated are the slit positions of the spectroscopy run (the slit width was 1″). For HE 1248-1356 the Ks-band image is shown.*

The global importance of determining physical properties of host galaxies is described in Chapter 4. A major advantage of observations in the NIR is that in this wavelength regime extinction is much smaller than in the visible ($A_K = 0.112A_V$, Rieke & Lebofsky (1985)), and that it traces the mass dominating stellar population. E.g. Reunanen et al. (2002) present NIR-spectroscopy of two Seyfert 1, three Seyfert 2 and one Seyfert 1.5 and show that in Seyfert 2 galaxies Fe II is generally stronger than Brγ or H_2 lines, while apparently in Seyfert 1 galaxies Brγ is stronger. Rodríguez-Ardila et al. (2004) also studied H_2 and Fe II line emission in a sample of 22 (mostly) Seyfert galaxies and concluded that these lines originate in different regions due to systematically different linewidths. They detected molecular Hydrogen in 90% of their sources,

with the majority being excited by thermal excitation processes. They also find a correlation between H_2/Brγ and Fe II/Paβ which can be useful to distinguish emitting line objects by their level of nuclear activity.

Here, the first near infrared (NIR) observations on 9 Seyfert 1 galaxies selected from the nearby QSO sample are presented.

Low resolution (R=500) spectroscopy in the Ks-band (2.2μm) yields analysis of several diagnostic lines such as hydrogen recombination lines (Paα & Brγ) and rotational-vibrational molecular hydrogen lines. The stellar CO absorption bands (^{12}CO(2−0)) allow analysis of dominating stellar spectral classes and of stellar dynamics. Moreover, J- (1.25μm) H- (1.65μm) and Ks-band imaging provides information on extinction in the galaxy and on whether the nuclear or the stellar component dominates the galaxy's radiation.

Section 5.1 of this chapter describes the details of the performed NIR observations as well as the data reduction and calibration procedures for imaging and spectroscopy. In Sect. 5.2, general spectroscopic results and in Sect. 5.3 results of the photometry are presented. Sect. 5.4 gives a short discussion on the individual sources and is followed by a general summary and conclusion in Sect. 5.5.

5.1 Observation, reduction and calibration

9 AGN drawn from the Nearby Borderline QSO sample were observed in seeing limited mode[22] with the Infrared Spectrometer and Array Camera (ISAAC) mounted to ANTU (UT1) at the Very Large Telescope (VLT) in Chile of the European Southern Observatory (ESO) during April the 18th-20th 2003. ISAAC's 1024×1024 pixel detector provides a pixel scale of 0.1484″/pixel with a field of view (FOV) of 152 ×152 arcsec^2. Our data consist of H- and Ks-band imaging and Ks-band low resolution long slit spectroscopy with a 1″ slit, resulting in a resolution of R=$\lambda/\Delta\lambda$=500.

The 9 observed sources are selected from the Nearby Borderline QSO Sample to comply to observational constraints; all targets are classified as Seyfert 1/narrow line Seyfert 1 galaxies.

Data reduction was carried out with IRAF & IDL using standard procedures.

Table 5.1: *Integration times (t_{int}) and seeing conditions for the photometric and spectroscopic observations. For spectroscopy, also the position angle PA of the 1″ slit is listed. In all tables and figures throughout this thesis, the source VCV(2001) J204409.7-104324 is labeled as VCV J204409.7...*

Source	Imaging				Spectroscopy		
	H-band		Ks-band		Ks-band		
	t_{int}	Seeing	t_{int}	Seeing	t_{int}	Seeing	PA
HE 0853-0126	7.2s	1.0″	7.2s	0.9″	3900s	1.8″	34°
HE 1013-1947	7.2s	1.0″	7.2s	0.8″	2700s	1.6″	2°
HE 1017-0305	8s	1.0″	8s	0.8″	2700s	0.7″	108°
HE 1029-1831	8s	0.9″	8s	0.7″	2700s	1.8″	-1°
HE 1248-1356	12s	1.7″	8s	0.6″	2880s	1.7″	103°
HE 1328-2508	8s	0.6″	8s	0.5″	2880s	2.7″	40°
HE 1338-1423	8s	0.5″	8s	0.4″	2880s	0.8″	162°
HE 2211-3903	8s	0.6″	8s	0.6″	3840s	0.8″	52°
VCV J204409.7...	8s	0.6″	8s	0.7″	1440s	2.6″	165°

5.1.1 Imaging

The main objective of the observing run was to obtain spectroscopic data, therefore only a small fraction of the observation time was assigned to imaging. The images of each object were taken using position jittering in an ABBA source pattern, integration times are shown in Tab. 5.1. The background was subtracted from the individual frames by subtracting consecutive frames from each other. After shifting the resulting frames with respect to one reference frame, a median image was created. Since visual inspection of the flat fields showed that the ISAAC detector pixels do not add significant multiplicative signal variations to the images, no flat field was applied. The resulting images are shown in Fig. 5.1.

The images were flux calibrated using the data from the 2 Micron All Sky Survey (2MASS). With H- and Ks-band 2MASS-flux values for apertures with a diameter of 14″(see Tab. 5.2) zero points (ZP) were calculated for each object. The H-band 2MASS and ISAAC filter match perfectly. Compared to the ISAAC Ks-band filter, the 2MASS filter is slightly broader on the blue side. If the sources show a flat spectrum, the transfer into the 2MASS system does not

[22] Atmospheric turbulences produce variations in the refractive index of the air. During the passage of light through the Earths atmosphere, these variations distort the incoming plane wave fronts from their straight propagation. This effect is called seeing.

Table 5.2: *The 2MASS flux in magnitudes for a 14″ aperture for J-, H- and Ks-band*

Source	J-band	H-band	Ks-band
HE 0853-0126	14.02±0.04	13.36±0.06	12.82±0.07
HE 1013-1947	13.53±0.03	12.86±0.04	12.30±0.04
HE 1017-0305	13.29±0.03	12.52±0.03	12.03±0.04
HE 1029-1831	12.30±0.02	12.21±0.02	11.70±0.03
HE 1248-1356	12.24±0.01	11.49±0.01	11.15±0.02
HE 1328-2508	12.17±0.01	11.41±0.01	11.02±0.01
HE 1338-1423	12.65±0.01	11.80±0.01	11.06±0.02
HE 2211-3903	12.69±0.01	11.80±0.02	10.96±0.01
VCV J204409.7...	11.74±0.01	10.95±0.01	10.11±0.01

result in any error. By the means of the slope of our K-band spectra, we estimate that the relative flux error through calibration does not exceed 3%. From the background noise, the flux calibration and taking into account that the images were not flatfielded, a conservative error-estimation for H- and K-band fluxes is 10%. In addition to our own ISAAC data we relied on J-Band 2MASS images to generate a 2-color diagram. Due to high noise in these images, the error is estimated to 15%. Hence the errors for the extracted colors are $\Delta m_{H-Ks} = \pm 0.14^{mag}$ and $\Delta m_{J-H} = \pm 0.18^{mag}$.

5.1.2 Spectroscopy

If the host galaxies showed prominent structures already in the acquisition images, an alignment of the slit along this structure was preferred. The slit angles are indicated in Fig. 5.1 and presented in Tab. 5.1, together with the integration times and the seeing conditions for the spectroscopy.

Similar to the imaging, the sky-subtraction was achieved with a nodding technique and no flatfielding was applied. The individual spectra were corrected for slit-curvature, shifting and creating a median then resulted in the final spectrum. Telluric correction was performed with B-type stars of which observations directly followed or preceded the observations of the targets. Hydrogen absorption lines in the telluric star's spectrum were removed by fitting a Lorentz-profile to the line prior to the telluric correction. After division by the spectrum of the telluric standard, the galaxy's spectrum was multiplied by a blackbody of temperature equal to the effective temperature of the star.

The spectra were wavelength calibrated using OH-lines from the sky. Flux-calibration was applied with the zero points calculated from the imaging.

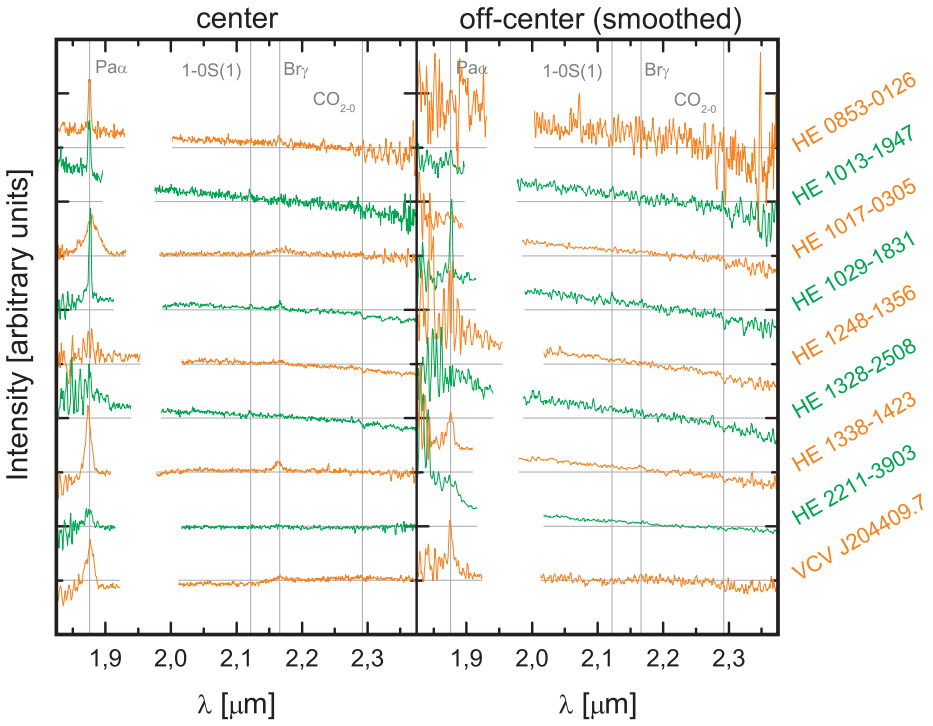

Figure 5.2: *Ks-band spectra of the 9 AGN, extracted at the central region (left) and at a distance of 1.5 seeing-FWHM (right, 3-pixel-boxcar-smoothed). Indicated are the detected lines in this sample, the Paα and Brγ lines as well as the CO absorption and the H_2 (1-0)S(1)-emission line. The spectra are presented in restframe and the region at ~2 μm is blanked out due to imperfect atmospheric correction. The normalization was carried out at 2.2μm in observer frame. Note that the features at > 2.25μm in HE 0853-0126 probably are not CO absorption features but noise caused by the atmosphere. See section 5.4 for spectra integrated over the whole galaxy. Remarkable are the red continua in most central regions.*

In most of the observations, the seeing was much larger than the used slit width of 1″(see Table 5.1). Hence, the contribution of the AGN to the spectra is diluted and overall the observed spectra will be more influenced by their host-galaxy properties. Any flux measurements along the slit depend on the seeing.

5.2 Spectroscopy

With the integration times given in Tab. 5.1, we achieved signal-to-noise ratios (S/N) on the continuum of 15-40 (the values represent the central spectrum with the highest signal).

Table 5.3: *Hydrogen recombination lines in the 9 AGN. Listed Paα and Brγ fluxes are for spectra integrated over the entire galaxy. The widths of the broad and the narrow component of the Paα line are for the central spectra. For investigations of the spatial dependency of the line fluxes along the slit, see respective diagrams in Section 5.4.*

Source	Paα [10^{-23} W m^{-2}]	FWHM$_{broad}$ [km s^{-1}]	FWHM$_{narrow}$ [km s^{-1}]	Brγ [10^{-24} W m^{-2}]
HE 0853-0126	3.3(±3.6%)		523(±20%)	[4.0(±16.3%)]
HE 1013-1947	13.3(±2.5%)	3190(±20%)	437(±20%)	7.6(±14.6%)
HE 1017-0305	28.9(±3.3%)	3736(±20%)		42.7(±5.1%)
HE 1029-1831	56.9(±7.1%)	2081(±20%)	92(±40%)	49.1(±5.3%)
HE 1248-1356				
HE 1328-2508				
HE 1338-1423	63.6(±3.5%)	2249(±20%)	288(±30%)	82.7(±5.0%)
HE 2211-3903	54.0(±8.0%)			[21.3(±18.3%)]
VCV J204409.7...	102(±3.1%)	2353(±20%)	101.3(±5.0%)	

For a comparison between central and off-nuclear spectra, see Fig. 5.2. The spectra are integrated over apertures matching the FWHM of the seeing (see Tab. 5.1), centered on the nucleus (left) or at a distance of 1.5 times the seeing-FWHM (right). Because of low signal to noise in the off-nuclear regions, these spectra are smoothed with a 3-pixel boxcar. With respect to the continuum slope, most of the central spectra in Fig. 5.2 show a reddened continuum. The CO-detected galaxies appear bluer than the other galaxies (see Section 5.2.3). However, this effect cannot clearly be separated from the influences of the seeing (see Section 5.1.2).

For details on the analyses of the individual galaxies, as well as spectra integrated over the whole galaxy (i.e. 3 times seeing-FWHM), see Section 5.4.

5.2.1 Hydrogen recombination lines

Prominent gaseous diagnostic lines are the hydrogen recombination lines Brγ (λ2.1661μm) and Paα (λ1.8756μm). Assuming case B recombination, typical electron densities of 10^4cm^{-3} and temperatures of 10000K (Osterbrock 1989), line ratios of Paα/Brγ are calculated to 12/1. We calculated the extinction with an extinction law that follows $\lambda^{-1.75}$ (Draine 1989) and using the screen model (e.g. Thronson et al. 1990), values are shown in Tab. 5.3.

Paα and Brγ both are detected in seven of the observed galaxies (see Tab. 5.3). The shape of these lines varies strongly, though. The strong Paα emission allows (with the exception of HE 0853-0126 and HE 2211-3903) a separation into a broad and a narrow component. However, the broad components of HE

1013-1947 and HE 1029-1831 could be influenced by an unresolved He line (λ1.868μm), since the broad component is rather asymmetric towards the blue.

The broad components of HE 1013-1947 with a FWHM of 3190 km s^{-1}± 20% and HE 1017-0305 with a FWHM of 3740 km s^{-1}±20% show widths characteristic of ordinary Seyfert 1 galaxies. In the cases of HE 1029-1831, HE 1338-1423 and VCV(2001) J204409.7-104324, the broad components show widths around 2000 km s^{-1}, typical for a narrow line Seyfert 1 galaxy (e.g. Rodríguez-Ardila et al. 2000b).

Only the integrated spectra supplied sufficient S/N to calculate extinction in the galaxies within reasonable errors. Case B approximation is only valid for the narrow line region (NLR), but in our Brγ lines, no separation between NLR and broad line region (BLR) is possible. Although Paα and Brγ are detected in most of the sources, only in HE 0853-0126 and HE 1029-1831, where the line emission is clearly dominated by the NLR, case B is a valid approximation and conclusions on the extinction can be drawn. Using the screen model, and following an extinction law $\propto \lambda^{-1.75}$, the latter one shows a visual extinction smaller than 3^{mag}. For HE 0853-0126, I can only determine a lower limit of $A_V > 0$, i.e. there is some extinction.

Because of their low redshift, the Paα line in HE 1248-1356 and HE 1328-2508 is shifted into a region of low atmospheric transmission and high variability. This could explain why we did not detect this line in these sources.

5.2.2 Molecular hydrogen

In three sources, HE 1013-1947, HE 1029-1831 and HE 1328-2508, extended molecular hydrogen is detected in the rotational-vibrational H_2 emission line 1-0S(1) at 2.1218μm (see Figs. 5.8,5.12,5.16). It is thought that molecular Hydrogen can be found in 70-80% of all Seyfert 1 galaxies, Rodríguez-Ardila et al. (2000a) detected H_2 in 90% of a sample of 22 AGN (19 Seyfert 1). Comparingly, with expected H_2 (1-0)S(1)/Brγ line ratios between 0.6 and 2, our molecular Hydrogen detection rate appears lower. But due to the fact that only two of the five galaxies with Brγ show also a H_2-line, the small sample-size has to be taken into account. With the mere detection of the 1-0S(1) emission line, we cannot distinguish between any excitation-mechanisms.

5.2.3 Stellar CO absorption

The ^{12}CO(2 – 0) (λ2.295μm) absorption feature of red, evolved stars is by far the strongest absorption feature in the range of 1-3μm (Gaffney et al. 1995). The absorption is depending on the effective temperature of the star, but also on

its luminosity class (Kleinmann & Hall 1986). Absorption rises towards lower temperatures and from dwarfs to supergiants.

After Doyon et al. (1994) and Goldader et al. (1995), the spectroscopic CO index, corresponding to the equivalent width (EW, Origlia & Oliva 2000), can be used to determine the continuum-dominating stellar luminosity class. However, due to the possible contamination of the stellar light by non-thermal radiation, the calculated CO equivalent widths for the AGN in this chapter are lower limit estimates for the intrinsic CO band strength. In our sample, CO absorption is detected in five AGN at a 2σ level with respect to the continuum[23] (HE 1013-1947, HE 1017-0305, HE 1029-1831, HE 1248-1356 and HE 1328-2508). The EWs of the CO absorption are presented in table 5.4, together with additional upper limits for the remaining sources. With the exception of HE 1328-2508, all sources show the described effect that the equivalent width decreases towards the center (but to different extents). Therefore, it is difficult to draw conclusions on the underlying stellar composition (Origlia et al. 1993) since it is not clear whether the change in the CO absorption is caused by a rising non-stellar continuum and/or a change in spectral class. Assuming that the values deduced in the outer regions of the galaxy are rather free from non-stellar continuum, a depth of (6 ± 3) Å as it can be found in HE 1029-1831 and HE 1328-2508 corresponds to the value expected for that of K0-3 giants (Kleinmann & Hall 1986). The comparatively deep CO-absorption in HE 1248-1356 with a width of (11 ± 2) Å points to late K or early M giants. In starburst galaxies , deep CO absorption is linked to young red supergiants. A typical starburst galaxy such as M82 shows an equivalent width of (15 ± 1) Å (Tamura et al. 1991) which is significantly deeper than found in HE 1013-1947, HE 1029-1831 and 1328-2508. Their values are consistent with those found in ordinary elliptical and spiral galaxies (Frogel et al. 1978). Therefore, the absorption in HE 1248-1356 can most likely be attributed to ongoing starformation in its host galaxy. A narrow EW of ~3 Å as it can be found in the host of HE 1017-0305 is typical for G/K dwarfs (Kleinmann & Hall 1986). In HE 0853-0126, the absorption at wavelengths >2.25 μm is probably caused by atmospheric noise. The line-shape does not resemble that of stellar CO-absorption.

The CO(2-0) bandhead is also a useful feature for investigations of the underlying stellar dynamics. The observed CO absorption in the galaxy is (in a rough approximation) the convolution of the star that dominates the CO absorption with the line-of-sight velocity profile (LOSVP), so the LOSVP can either be determined by basic deconvolution processes, or via comparison to a convolved spectrum of a star or a stellar population. For best results with our galaxy

[23]The RMS is determined in the region from (2.00-2.29) μm (restframe).

Table 5.4: *The CO equivalent width in Å for the four sources with detected stellar CO absorption. The values in italics are upper limits.*

Source	Central EW_{CO}	Off-nuclear CO EW_{CO}
HE 0853-0126	(*7*)	(3 ± 1)
HE 1013-1947	4 ± 2	7 ± 4
HE 1017-0305	1.2 ± 0.2	3 ± 1
HE 1029-1831	5 ± 2	6 ± 3
HE 1248-1356	4 ± 1	11 ± 2
HE 1328-2508	6 ± 2	6 ± 3
HE 1338-1423	*1.3*	*4.9*
HE 2211-3903	*1.2*	*1.5*
VCV J204409.7...	*2.8*	*1.8*

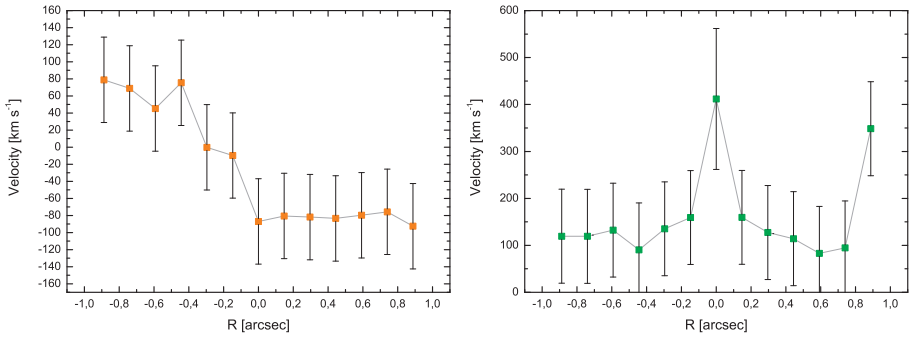

Figure 5.3: *HE 1248-1356: In a) the stellar velocity dispersion and in b) the stellar rotation curve is shown. In the central spectrum, the velocity dispersion is calculated to 411±150 km s^{-1}, see text for details.*

spectra of low resolution and S/N ratios, we fitted a stellar template spectrum, convolved with a Gaussian distribution (representing the LOSVP), to the galaxy spectrum (Gaffney et al. 1995) with the Nelder-Mead downhill simplex algorithm. Note that in this procedure, the selection of the correct stellar template is essential since template-mismatch produces significantly too high velocity dispersions. The characteristic for the selection of the stellar spectrum is an according equivalent width of the CO(2-0) absorption bandhead to the galaxy's spectrum (Gaffney et al. 1993). Hence our deduced velocity dispersion is an upper limit to the intrinsic velocity dispersion of the galaxy. For the analysis in this sample, we relied on spectra of K- and M- giants and supergiants in the K-band from Hinkle & Wallace (2001) (native resolution of R=3000)[24]. Convolution with a Gaussian distribution result in K-band stellar template spectra at a resolution of R=500.

Among the sources with detected CO absorption, HE 1248-1356 is the only object in our sample where the stellar velocity field is resolved. Fig. 5.3a) and 5.3b) show the resulting velocity dispersion and stellar rotational curve of HE 1248-1356. The seeing during the observations of HE 1248-1356 was 1.7″ (see Tab. 5.1). The deduced velocity dispersion of σ=400 $km\ s^{-1}$ yields an enclosed virial mass of $2{\cdot}10^{10}$ $M_\odot$ in the seeing disk (= 0.5 kpc), a typical value for Seyfert galaxies. However, this mass estimate has to be taken with caution because the seeing during observations was large and the shown data-points are strongly correlated. Depending on the exact shape of the rotation curve and the distribution of the velocity dispersion, σ is likely to increase under better seeing conditions (i.e. smaller R). Here clearly investigations under higher angular (and spectral) resolution are required.

5.3 Photometry

ISAAC H-band images of each source are presented in Fig. 5.1. The images clearly resolve structures of the underlying host galaxy like bars and spiral arms, even without a subtraction of the nucleus; for a morphologic classification of the individual host galaxies, see Tab. 5.5. The sample is mostly dominated by spiral galaxies. Since all our galaxies are lower luminosity AGN, this supports the theory that the probability to find disk dominated host galaxies increases towards lower luminosity nuclei (e.g. Jahnke et al. 2004, and references therein). For more details on the morphology, see Sect. 5.4.

In combination with the J-band data from 2MASS we derived colors for

[24]These sources can be found online in the SIMBAD database, which is operated at CDS, Strasbourg, France; url: http://simbad.u-strasbg.fr/Simbad.

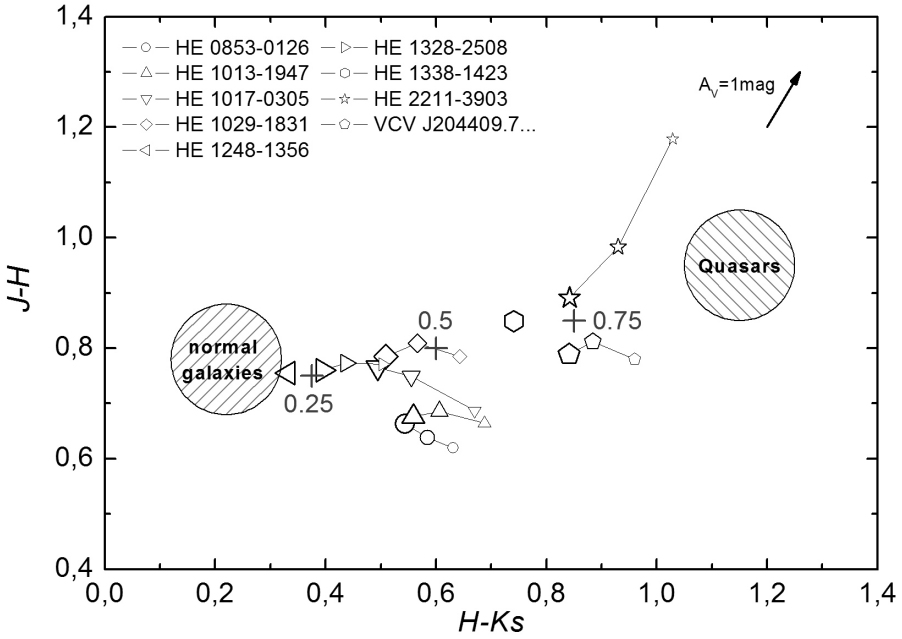

Figure 5.4: *The NIR 2-color diagram for the 9 Seyfert 1 galaxies. The three different sized data markers for each galaxy represent the flux measurements in apertures of 14″, 8″ and 3″, centered on the nucleus. Additionally, the regions of normal galaxies and Quasars and the arrow specifying a visual extinction of 1*^{mag} *are indicated in the graph. The locus of the three crosses (in gray) is based upon calculations by* Hyland & Allen *(1982) and refers to the radiation output from normal galaxies with gradually increased Quasar contribution (+*$_{0.25}$*: 25% nuclear radiation...).*

Table 5.5: *Morphology and redshifts. The morphological classifications are deduced in this study. The references for the redshifts are as follows:* [1]*: LEDA/SIMBAD 2002 comparison,* [2]*: QDOT all-sky IRAS galaxy redshift survey,* [3]*:* Wisotzki et al. *(2000),* [4]*: NED team.*

Source	morphological classification	redshift	references
HE 0853-0126	SBb/c	0.059903	[1]
HE 1013-1947	SB	0.055	[3]
HE 1017-0305	interacting (S)	0.0468	[4]
HE 1029-1831	SBc	0.040134	[1]
HE 1248-1356	Sa/SBa	0.014557	[1]
HE 1328-2508	interacting (S)	0.026485	[1]
HE 1338-1423	SB	0.041752	[1]
HE 2211-3903	SB	0.038473	[2]
VCV J204409.7...	E3	0.034373	[2]

each of the 9 AGN in apertures centered on the nucleus. In the NIR, colors of an active galaxy consist of several components: A stellar component, a Quasar-like component, an extinction-component and a component associated to hot dust. Hyland & Allen (1982) calculated mean colors of Quasars to $(J - H) = 0.95$ and $(H - Ks) = 1.15$ (corrected for redshift), while ordinary galaxies have colors of $(J - H) = 0.78$, $(H - Ks) = 0.22$ (Glass 1984). Wavelength dependent extinction is expressed by a shift along the direction of a vector representing a visual extinction of 1^{mag} (following $A_V : A_J : A_H : A_K = 1 : 0.282 : 0.175 : 0.112$ (Rieke & Lebofsky 1985; Binney & Merrifield 1998)). Re-radiation of hot dust at temperatures of ~300 K in the surroundings of the nucleus results in an increased flux especially in the K-band, so in the 2-color diagram this effect manifests itself in a horizontal shift in H-Ks (Glass 1984).

We measured the flux of each galaxy in apertures of three different sizes, always centered on the nucleus: One aperture size basically encloses the whole object (14″ diameter), one encloses only the nucleus (3″) and one intermediate size (8″) was chosen. A K-correction was not applied because at the redshifts of the sample its effect is contained in the photometric error bars. To compare the ISAAC seeing limited images (resolution: (0.6-1)″) to the 2MASS J-band images (resolution: (2.3-2.8)″) the ISAAC images were smoothed with a Gaussian distribution such that the H- and Ks-band images show resolutions corresponding to their respective J-band images. The smallest used aperture measures 3″, according to the resolution limit of the 2MASS data. The resulting 2-color diagram is shown in Fig. 5.4. For HE 1338-1423 and HE 1248-1356[25] only the color value extracted from the largest aperture is shown because the J-band colors in smaller apertures do not provide physical results.

As expected for Seyfert 1 galaxies (cf. Ward et al. 1982) the global colors of the 9 sources are located in between the regions of Quasar colors and colors of ordinary galaxies. They all are distributed along the line connecting the two extreme cases, thus indicating a varying importance of the Quasar component in each object. The colors of HE 2211-3903 and VCV(2001) J204409.7-104324 show that these galaxies are dominated by their non-stellar nucleus. A dominating stellar component in HE 1248-1356, HE 1328-2508, HE 1013-1947 and HE 1029-1831 could be connected with the detection of stellar CO absorption in the spectra of exactly these sources, because the strong contribution of the non-stellar nuclei in the other sources can prevent such detection. The continuum slopes of the K-band spectra demonstrate similar tendencies.

Rising influences of the nucleus are expressed in a shift of the color towards

[25] Due to unfortunate shifting in the observations of HE 1248-1356, no H-band image could be generated. Here we additionally relied on a 2MASS H-band image.

Table 5.6: *Measured $JHKs$ magnitudes of the aperture photometry in the $8''$ (first line) and $3''$ (second line) aperture (since the photometric calibration was performed in reference to the 2MASS $14''$ aperture data, according magnitudes can be found in Tab. 5.2). In addition, the $H-Ks$-colors of the host galaxy are presented (see text for details on the process of subtraction of the nucleus).*

Source	J-band	H-band	Ks-band	$H-Ks$
HE 0853-0126	14.451	13.813	13.228	0.31
	15.721	15.102	14.470	
HE 1013-1947	13.838	13.153	12.547	0.51
	15.005	14.342	13.653	
HE 1017-0305	13.690	12.941	12.386	0.55
	15.002	14.315	13.646	
HE 1029-18311	13.232	12.422	11.856	0.31
	14.337	13.551	12.909	
HE 1248-1356	(12.765)	(12.853)	(11.601)	-
	(14.132)	(14.588)	(12.856)	
HE 1328-2508	12.551	11.778	11.341	0.28
	13.865	13.094	12.591	
HE 1338-1423	(12.950)	(12.189)	(11.364)	0.48
	(14.120)	(13.588)	(12.671)	
HE 2211-3903	12.998	12.016	11.086	0.34
	14.220	13.041	12.012	
VCV J204409.7...	11.908	11.097	10.212	1.20
	12.934	12.154	11.193	

the region of Quasars with decreasing aperture size. This effect is superposed onto the effect of hot dust. All targets show increased nuclear radiation (in comparison to the stellar radiation) or re-radiation of hot dust but no significant amounts of extinction towards the nucleus, with the exception of HE 2211-3903 with a visual extinction of $\sim 2.5^{mag}$. Especially, HE 1017-0305 does not stand out with extraordinary amounts of extinction as the spectroscopically determined A_V would imply, but the photometric colors are averaged over larger apertures.

We also estimated H-K colors of the host galaxies by subtracting the contribution of the nucleus. Here we used the fact that the nucleus is unresolved, i.e. star like in extent. Hence the subtraction was performed by taking a star in the vicinity of the galaxy, shifting it to the center of the nucleus within subpixel accuracy and subtracting it scaled to the flux of the nucleus such that just no "hole" is produced in the galaxy. Ideally, this results in a smooth brightness distribution representing the contribution of the host galaxy. The flux of the host was determined in a $14''$aperture, values are shown in the last column of Tab. 5.6. The spiral galaxies show host-colors similar to or slightly redder than the colors of non-active spirals. The color of the elliptical galaxy VCV(2001) J204409.7-104324 is probably influenced by difficulties in removing the nucleus in the K-band. For HE 1248-1356 no host colors were calculated due to the lack of a high-resolution H-band image.

5.4 Notes on individual objects

The spectra, integrated over 3 times the seeing-FWHM, the line fluxes and the flux of the continuum of the objects, extracted along the slit, are presented in Fig. 5.5-5.22. In addition, a short discussion of each galaxy is given. Note that in most cases, the seeing during the spectroscopic observations was larger than the slitwidth (c.f. section 5.1.2).

- HE 0853-0126

  HE 0853-0126 shows a prominent bar structure (the slit was not placed along this bar because the structure was too faint to be resolved during acquisition). Two spiral arms can be seen reaching symmetrically out to the east and the west. The view on the galaxy is rather face-on. The region of the CO absorption is redshifted to the long wavelength cutoff of the K-band. In the resulting high noise, no CO absorption can be detected. Hydrogen recombination is seen in Paα and Brγ, a broad component in the Paα line is not detected, the galaxy is classified as Seyfert 1 in Wisotzki et al. (2000). A weak broad component could either be hidden in the noise

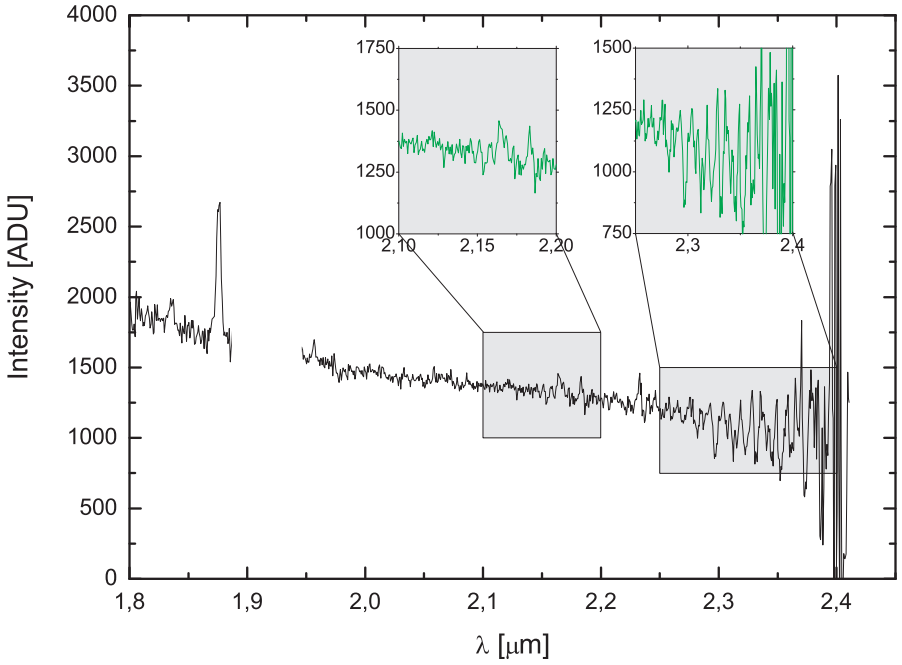

Figure 5.5: *The spectrum of HE 0853-0126, integrated over 5.3″(= 5 kpc). In addition to the overall K-band spectrum, the region of the Brγ line and the CO absorption are shown.*

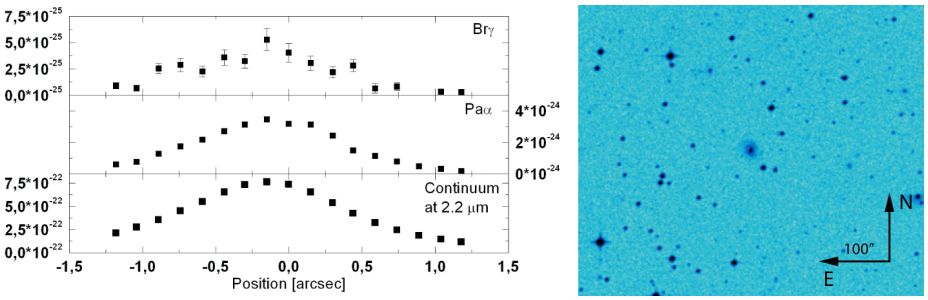

Figure 5.6: *Flux of HE 0853-0126. The flux of the Paα and Brγ line is given in units of $W\,m^{-2}$, the continuum flux is in units of $W\,m^{-2}\,\mu m^{-1}$. Where no errorbars can be seen, the data-marker's size exceeds the extension of the errorbars. On the right, a DSS2(red) image of the galaxy's large scale environment is shown.*

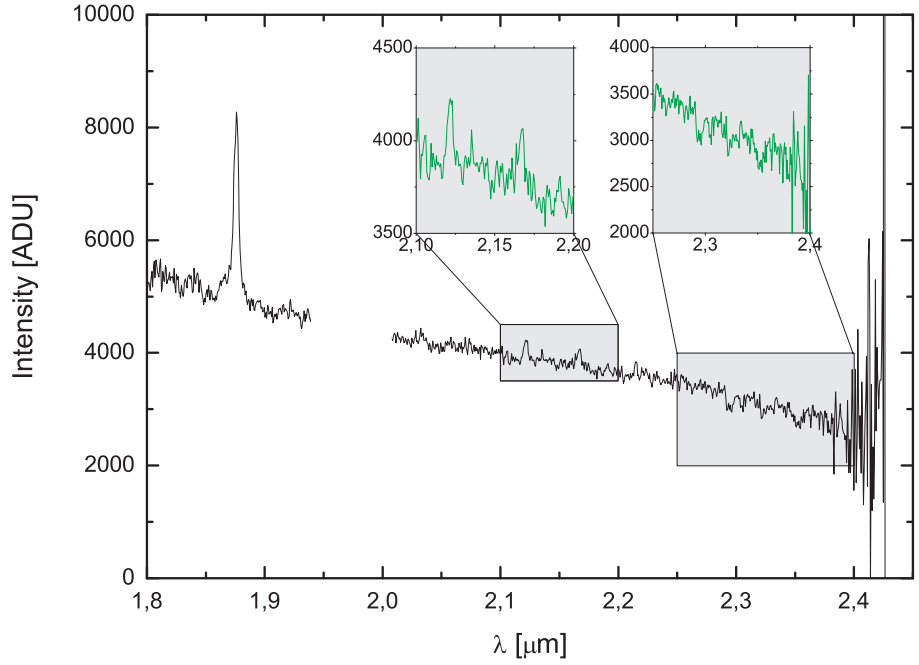

Figure 5.7: *The over 4.9″ (= 5 kpc) integrated spectrum of HE 1013-1947. In addition to the overall K-band spectrum, the region of the 1-0S(1)H_2 line and the Brγ line as well as the CO absorption are shown.*

of the spectrum, or the AGN is variable. In the region of (2.0-2.2)μm, the spectrum shows a S/N of 21 on the continuum. This causes high errors in the Brγ flux measurements and in the calculated visual extinction.

- HE 1013-1947

  The galaxy is a barred spiral galaxy and shows a very bright nucleus. Nagao et al. (2001) as well as Rodríguez-Ardila et al. (2000b) find HE 1013-1947 to be a narrow line Seyfert 1 galaxy with a broad component in Hα and Hβ of about 1900 km s^{-1}, which is narrower than the line width we extracted using Paα.s The difference between the optical and NIR-linewidths could be explained by extinction effects. The slight blueshift of the center of the broad component versus the center of the narrow component could indicate that an unresolved He line (λ1.838μm) influences our measurement.

  The integrated spectrum in Fig. 5.7 also shows CO absorption at wavelengths ≥2.29 μm. In the central spectrum, the equivalent width of the

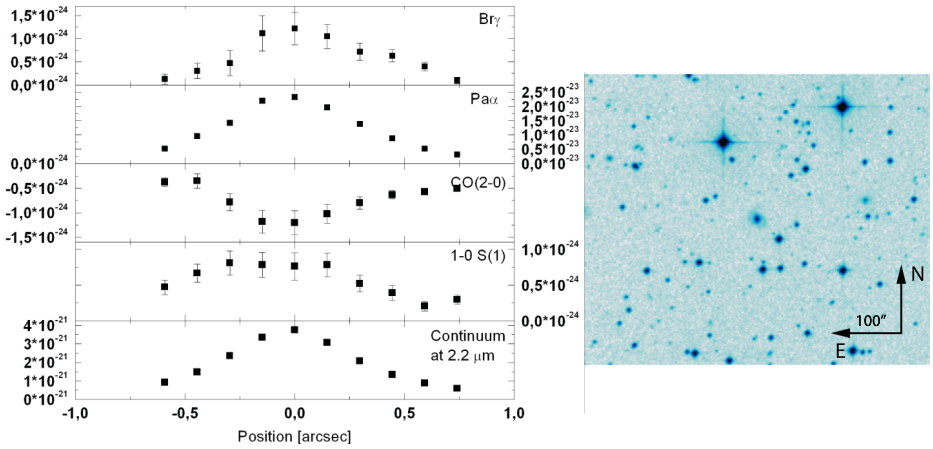

Figure 5.8: *Flux of HE 1013-1947. The flux of the Paα, Brγ, (1-0)S(1) H_2-line and the the flux deficit in* CO(2 − 0) *is presented in units of* $W\,m^{-2}$*, the continuum flux is in units of* $W\,m^{-2}\,\mu m^{-1}$*. On the right, a DSS2(red) image of the galaxy's large scale environment is shown.*

CO(2 − 0) absorption is (3.7 ± 2.4) Å, rising to an equivalent width of (7.5 ± 4) Å in the outer regions of the galaxy (see Tab. 5.4). The equivalent width at the center of the galaxy is diminished due to a larger contribution of the non-thermal continuum at the nucleus (the overall absorption in the CO(2 − 0) transition rises towards the nucleus, as can be seen in Fig. 5.8). An equivalent width of 7 Å corresponds to the value found for that of K0-3 giants (Kleinmann & Hall 1986).

The galaxy also shows extended H_2 emission in the (1-0)S(1) transition with a total flux of (7.4 ± 1)$\cdot 10^{-24}$ W m^{-2}, the line ratio to the Brγ line is calculated to 1.0 ± 0.2. According to Rodríguez-Ardila et al. (2000b), this ratio is a typical value for a Seyfert galaxy. Since this is the only detected molecular hydrogen line, excitation processes cannot be discussed.

- HE 1017-0305

  The radio quiet (Wadadekar 2004) galaxy shows a very prominent bar extending from east to west. Spiral arms are also resolved, but their shape is rather asymmetric which implies a disturbance possibly caused by a recent merger event. At a distance of 42″ to the NW of the object, the galaxy LEDA 1072782 with a redshift of z=0.04925 (Falco et al. 1999) can be found which supports the idea of an ongoing merger event. In Fig. 5.2, the continuum slopes at the center and away from the nucleus change significantly, with the spectrum being much bluer towards larger distances

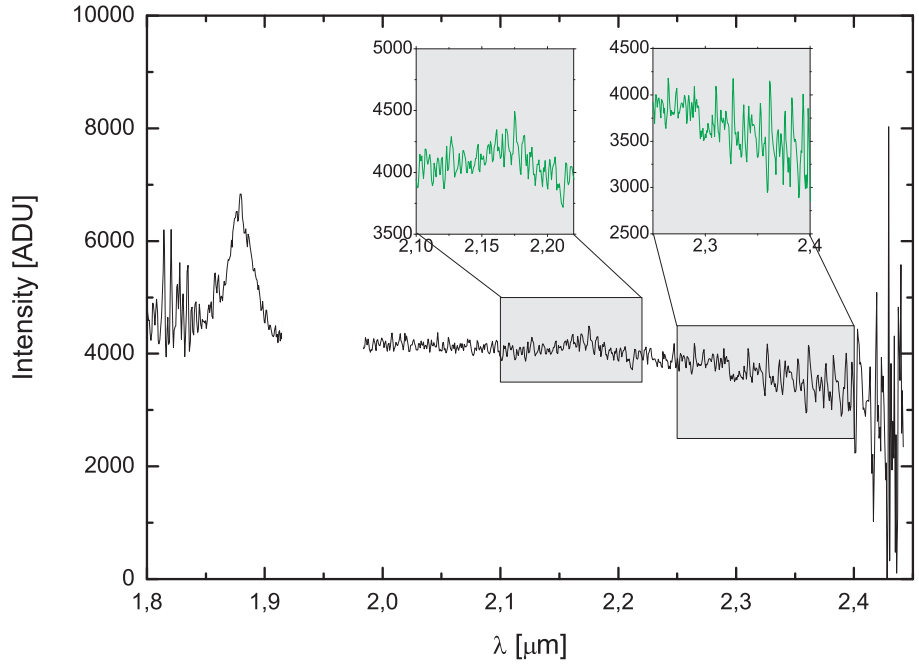

Figure 5.9: *The over 2.2″ (= 2.6 kpc) integrated spectrum of HE 1017-0305. In addition to the overall K-band spectrum, the region of the Brγ line and the CO absorption are shown.*

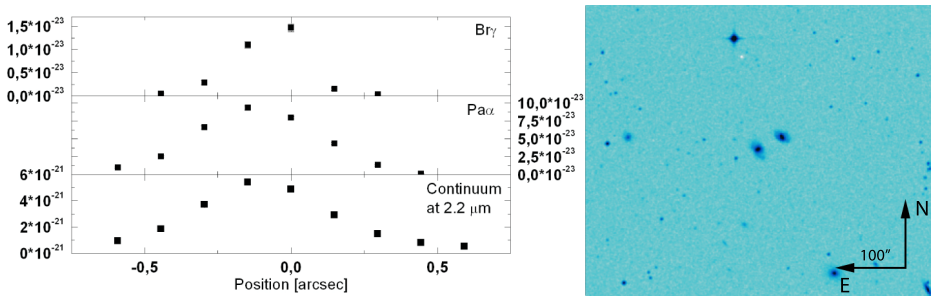

Figure 5.10: *Flux of HE 1017-0305. The flux of the Paα and Brγ line is given in units of $W\,m^{-2}$, the continuum flux is in units of $W\,m^{-2}\,\mu m^{-1}$. On the right, a DSS2(red) image of the galaxy's large scale environment is shown.*

from the nucleus. This is also represented by the calculated extinction of $(16 \pm 19)^{mag}$, but the high noise on the broad Brγ line (see Fig. 5.9) produces large errors in the measurement of its flux. In the region between 2 μm and 2.2 μm, the S/N on the continuum is 40. The two broad hydrogen recombination lines make HE 1017-0305 a typical representative for a Seyfert 1 galaxy. In the 2-color diagram (Fig. 5.4), the galaxy shows no strong amounts of reddening (note that due to the 2MASS-limited resolution, the extinction is derived from a larger area).

The upper limits for the IRAS fluxes (IRAS Vol. II catalog) yield an upper limit for the far-infrared luminosity of $L_{FIR}=6{\cdot}10^{10} L_{\odot}$, similar to the values found in starburst galaxies (Deutsch & Willner 1987).

There is an absorption feature detected at 2.3 μm, but its shape does not resemble a CO absorption band. Moreover the CO(3-1) and CO(4-2) absorption features are missing. Probably high noise in this region hides the absorption.

- HE 1029-1831

  The spiral arms and the bar structure are prominent features in the images, implying a face on view onto the galaxy. The flux ratios [NII]λ/Hα and [OIII]λ/Hβ indicate that HE 1029-1831 is an AGN. Using flux ratios of [SII]$\lambda\lambda$6717.31/Hα and [OIII]λ5007/Hβ, the galaxy is classified as HII/borderline galaxy, while the flux ratios of [OI]λ6300/Hα [OIII]λ5007/Hβ lead to a classification as AGN/borderline galaxy Kewley et al. (2001). In our spectrum, the Paα line can be separated into a broad and a narrow component with the broad component showing a width of 2081 km s^{-1} which is typical for a narrow line Seyfert 1 galaxy. This is consistent with the findings of Nagao et al. (2001) and Rodríguez-Ardila et al. (2000b) who determined the FWHM of Hα to be 1870 km s^{-1} and classified the object as a narrow line Seyfert 1 galaxy, too. As in HE 1013-1947, the broad component's shape looks slightly asymmetric what could be caused by an unresolved helium-line. The Paα/Brγ line ratio implies no significant reddening, which is consistent with the appearance of the continuum in Fig. 5.2 as well as with the results of the photometry (see Fig. 5.4).

  The equivalent width of the CO absorption feature decreases from (6 $\pm$ 3) Å at distances of 1″ away from the nucleus to (4 $\pm$ 2) Å at the center. The small variations of the equivalent width also substantiate only minor amounts of reddening. An equivalent width of 6 corresponds to equivalent widths found in early K0-3 giants (Kleinmann & Hall 1986).

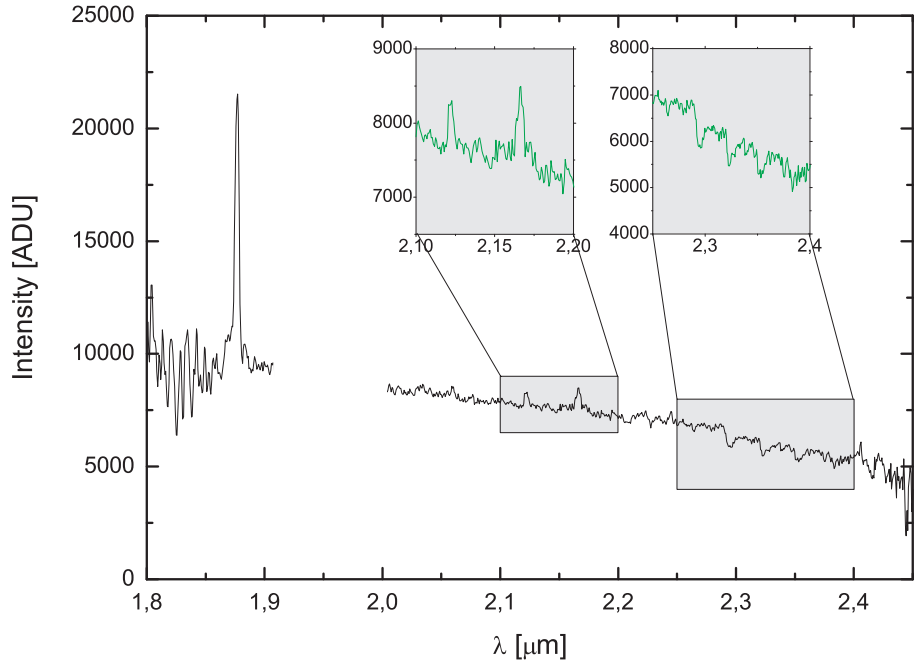

Figure 5.11: *The over 5.3″ (= 7.3 kpc) integrated spectrum of HE 1029-1831. In addition to the overall K-band spectrum, the region of the 1-0S(1)H_2 line and the Brγ line as well as the CO absorption are shown.*

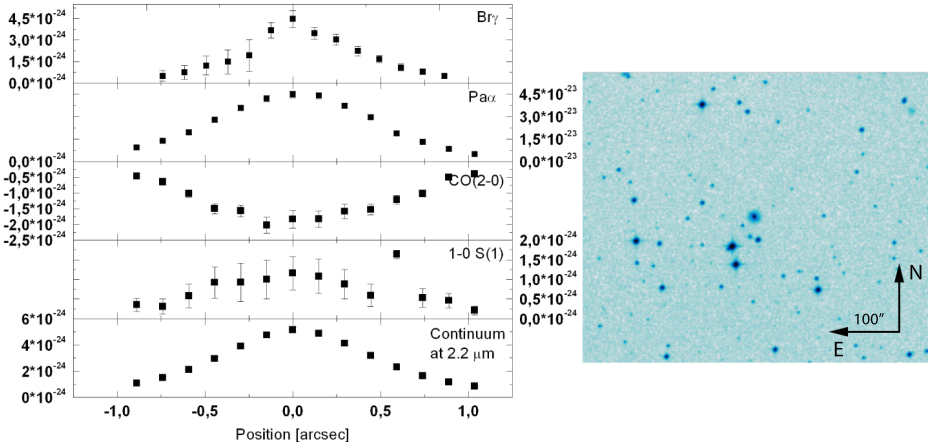

Figure 5.12: *Flux of HE 1029-1831. The flux of the Paα, Brγ, the (1-0)S(1) H_2-line and the flux deficit in CO(2 − 0) is presented in units of W m^{-2}, the continuum flux is in units of W m^{-2} μm^{-1}. On the right, a DSS2(red) image of the galaxy's large scale environment is shown.*

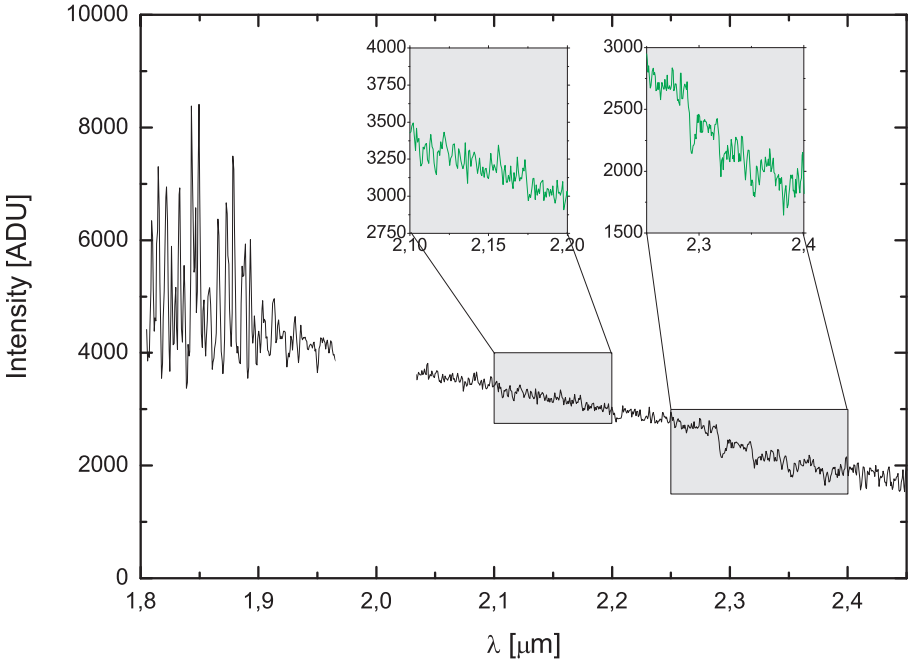

Figure 5.13: *The over 5.2″ (= 18.8 kpc) integrated spectrum of HE 1248-1356. In addition to the overall K-band spectrum, the region of the Brγ line as well as the CO absorption are shown.*

HE 1029-1831 also shows extended emission in the H_2 1-0S(1) transition with a total flux of (13.9 ± 1.4) $\cdot 10^{-24}$ W m^{-2} (see Fig. 5.12). The H_2 1-0(S(1)/Brγ line ratio is calculated as 0.29 ± 0.03. After Rodríguez-Ardila et al. (2004), a line ratio of 0.3 marks the transition from starburst galaxies to Seyferts, hence HE 1029-1831 shows only a comparatively small amount of activity for a Seyfert galaxy. In the 2-color diagram, the galaxy is located close to that of ordinary galaxies, revealing only small influences of the nucleus, too.

HE 1029-1831 is also an IRAS source with $F_{12\mu m}$ = (139 ± 39) mJy, $F_{25\mu m}$ = (411 ± 40) mJy, $F_{60\mu m}$ = (2545 ± 15) mJy and $F_{100\mu m}$= (3704 ± 333) mJy. This results in a far-infrared luminosity of L_{FIR}=1.9 $\cdot 10^{11} L_{\odot}$.

In summary, HE 1029-1831 probably is a luminous infrared galaxy with a weak narrow line AGN.

- HE 1248-1356

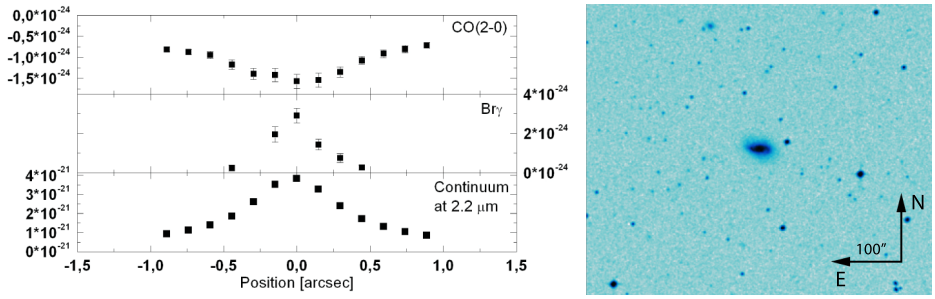

Figure 5.14: *Flux of HE 1248-1356. The flux of the Brγ line and the CO(2 – 0) flux deficit is given in units of W m^{-2}, the continuum flux is in units of W m^{-2} μm^{-1}. On the right, a DSS2(red) image of the galaxy's large scale environment is shown.*

This galaxy is the closest one of the observed sources. It shows very prominent spiral arms at the west and east, the galaxy is inclined (i=63±6) and the velocity curve calculated from the CO(2 – 0) bandhead (Fig. 5.3b) implies that the eastern arm is moving towards the observer. Rodríguez-Ardila et al. (2000b) as well as Maia et al. (2003) classified the object as a broad line Seyfert 1 galaxy. We do only detect a very faint but broad Brγ line (Fig. 5.14), though a weak Paα line could be hidden in the noise produced by atmospheric absorption (see Fig. 5.13). The CO absorption bands are very prominent features. The value of the CO-equivalent width at a distance of 1″ to the center is close to values typical for ongoing starformation. The depth decreases strongly towards the center, what indicates rising non-stellar continuum emission (Fig. 5.14). However, the slope of the continuum remains rather unaffected by this trend, the nuclear spectrum is already rather blue compared to the other observed sources.

- HE 1328-2508

  The galaxy shows strong signs of interaction, an indication of a tidal tail can be seen, extending towards NE. The bright nucleus is not located at the center of the galaxy, the source at a distance of 3″SE of the nucleus is either a foreground star or a second nucleus. We tried to subtract a point like source from this possible second nucleus with the same process as for the other nuclei. The contribution could not completely be removed here, which supports the theory of a real second nucleus (or at least an extended object along the line of sight). At 7″in the same direction, an additional source is located. This could be attributed to either a possible companion galaxy or a foreground star (cf. Jahnke & Wisotzki 2003). No Hydrogen recombination lines are observed and the spectrum shows stellar CO ab-

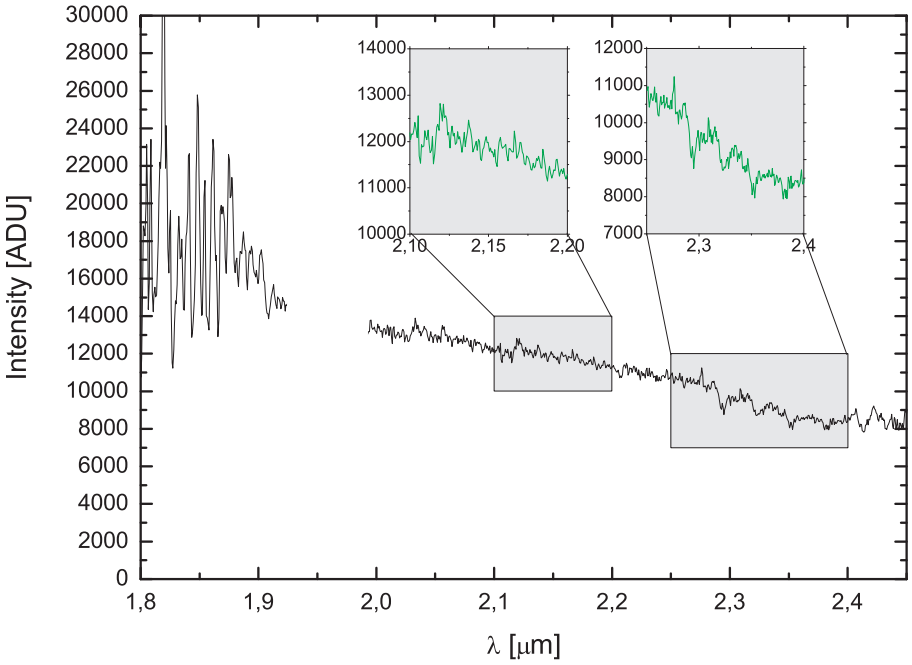

Figure 5.15: *The over 8.0″ (= 16.2 kpc) integrated spectrum of HE 1328-2508. In addition to the overall K-band spectrum, the region of the Brγ line as well as the CO absorption are shown.*

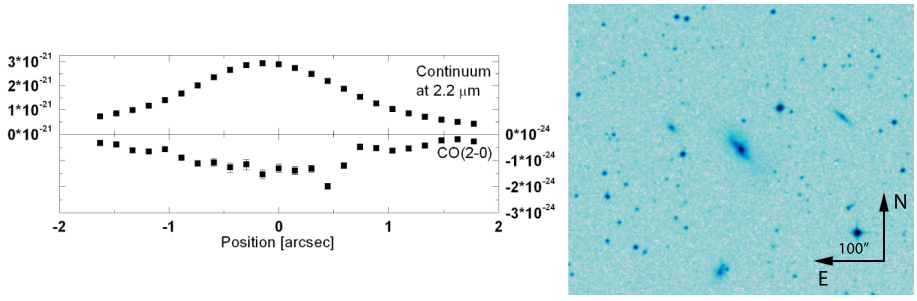

Figure 5.16: *Flux of HE 1328-2508. The flux of the* CO(2 – 0) *flux deficit is given in units of* $W\,m^{-2}$*, the continuum flux is in units of* $W\,m^{-2}\,\mu m^{-1}$*. On the right, a DSS2(red) image of the galaxy's large scale environment is shown.*

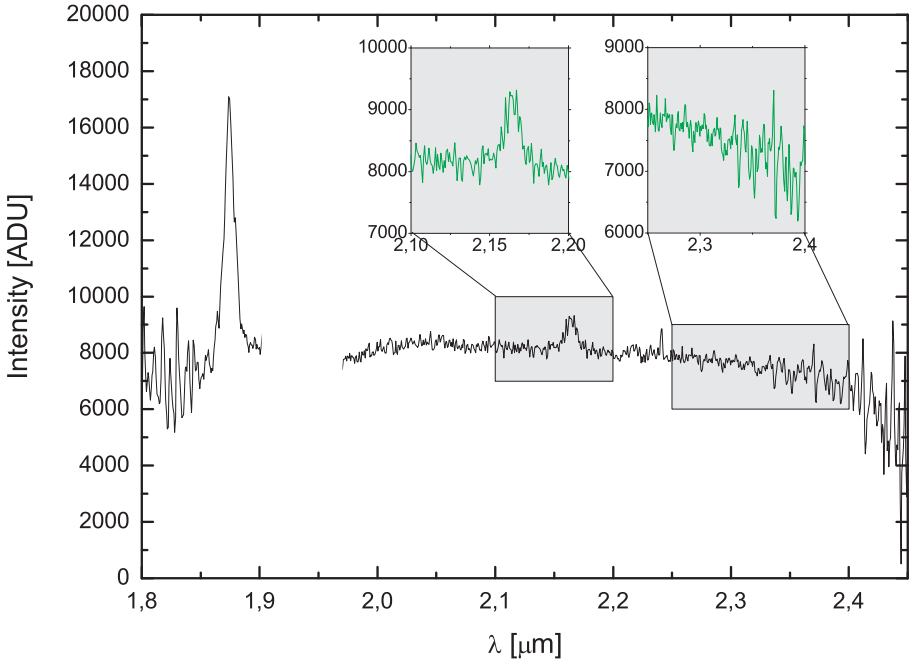

Figure 5.17: *The over 2.5″(= 3.3 kpc) integrated spectrum of HE 1338-1423. In addition to the overall K-band spectrum, the region of the Brγ line as well as the CO absorption are shown.*

sorption. In HE 1328-2508, however, the equivalent width of the CO(2-0) bandhead does not change with distance to the center as dramatically as it is observed in the other sources. In addition, the continuum slope shows no strong dependency on distance to the center. This could indicate only a small non-stellar contribution and is consistent with the location in the 2-color diagram near to the location of ordinary galaxies. The spectrum also shows molecular Hydrogen in emission at 2.122μm. Absorption makes the X-ray emission rather hard, its ROSAT hardness ratio (HR1) is determined to 0.63 ± 0.03 (Fischer et al. 1998).

- HE 1338-1423

  The ISAAC images resolve a clear bar structure and the host galaxy hence is classified as SB0 galaxy. Bade et al. (1995) derived a spectral power-law index from the RASS of 1.41±0.29. In comparison to the continuum, HE 1338-1423 shows very strong recombination lines. The equivalent widths are (218±4.4)Å for Paα and (18.1±0.1)Å for Brγ. The non-detection of CO-absorption, the strong change in continuum slope toward the center

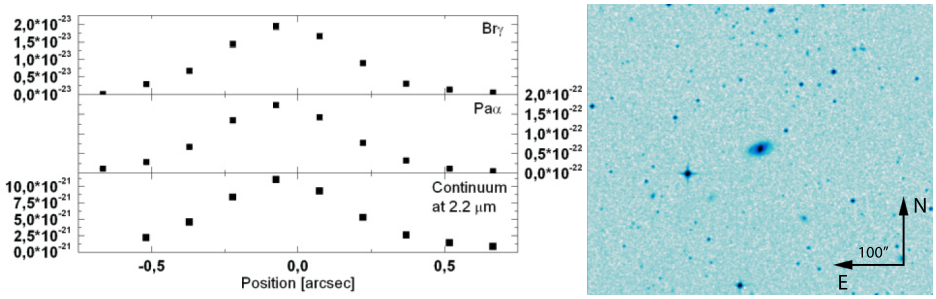

Figure 5.18: *Flux of HE 1338-1423. The flux of the Paα and the Brγ line is given in units of $W\,m^{-2}$, the continuum flux is in units of $W\,m^{-2}\,\mu m^{-1}$. On the right, a DSS2(red) image of the galaxy's large scale environment is shown.*

and the location in the 2-color diagram close to quasars all indicate to a strong non-stellar component. Our detected host galaxy colors are well in agreement with the results of Jahnke et al. (2004), who derived optical magnitudes of B=15.1, V=14.5, R=14.0 and I=13.4.

- HE 2211-3903

  The galaxy shows a bar extending from NE to SW and very faint indications of two spiral arms.

  Despite a high S/N ratio of ∼45, the only feature resolved in the spectra is the Paα line which shows a highly non-Gaussian shape, implying complicated kinematics in this galaxy. Continuum slope changes are similar as in HE 1338-1423. Maia et al. (2003) classified HE 2211-3903 as a Seyfert 1 galaxy via a broad Hα line.

  The upper limits for the IRAS fluxes in the IRAS Vol. II catalog (F60 is 0.77 Jy, F100 is an upper limit of 1.08 Jy) yield an upper limit for the far infrared luminosity of L_{FIR}=5.2·$10^{10} L_\odot$, similar to HE 1017-0305 and to the values found in starburst galaxies (Deutsch & Willner 1987).

- VCV(2001) J204409.7-104324

  The host is an elliptical galaxy with a very bright nucleus. J204409.7-104324 is better known as Mrk 509. It is an IRAS source with fluxes F12=0.34 Jy, F25=0.74 Jy, F60=1.42 Jy and F100=1.43 Jy resulting in a L_{FIR}=0.9·$10^{11} L_\odot$.

  Our colors are consistent with the results of Glass (2004), who classified Mrk 509 as Sy 1.5 galaxy and found average, de-reddened NIR colors of $J-H$=0.91, $H-K$=0.88 and $K-L$=1.35, significantly redder than

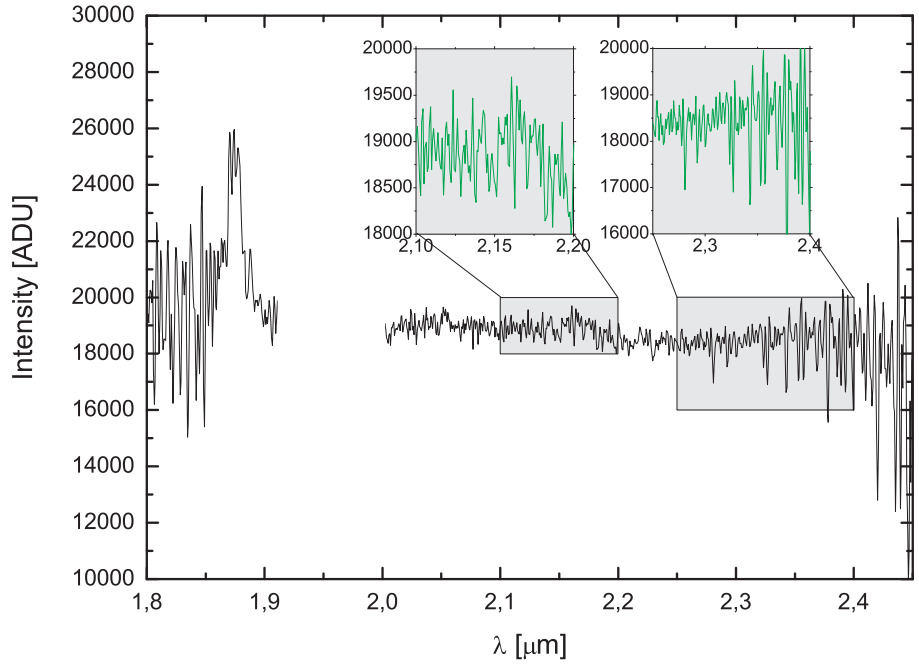

Figure 5.19: *The over 2.5″(= 3.6 kpc) integrated spectrum of HE 2211-3903. In addition to the overall K-band spectrum, the region of the Brγ line as well as the CO absorption are shown.*

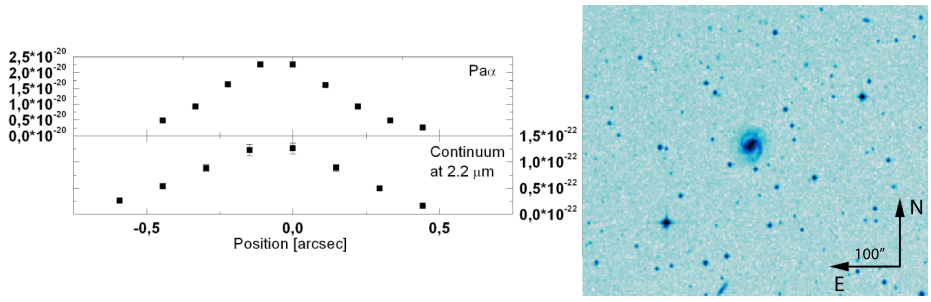

Figure 5.20: *Flux of HE 2211-3903. The flux of the Paα line a is given in units of $W\,m^{-2}$, the continuum flux is in units of $W\,m^{-2}\,\mu m^{-1}$.On the right, a DSS2(red) image of the galaxy's large scale environment is shown.*

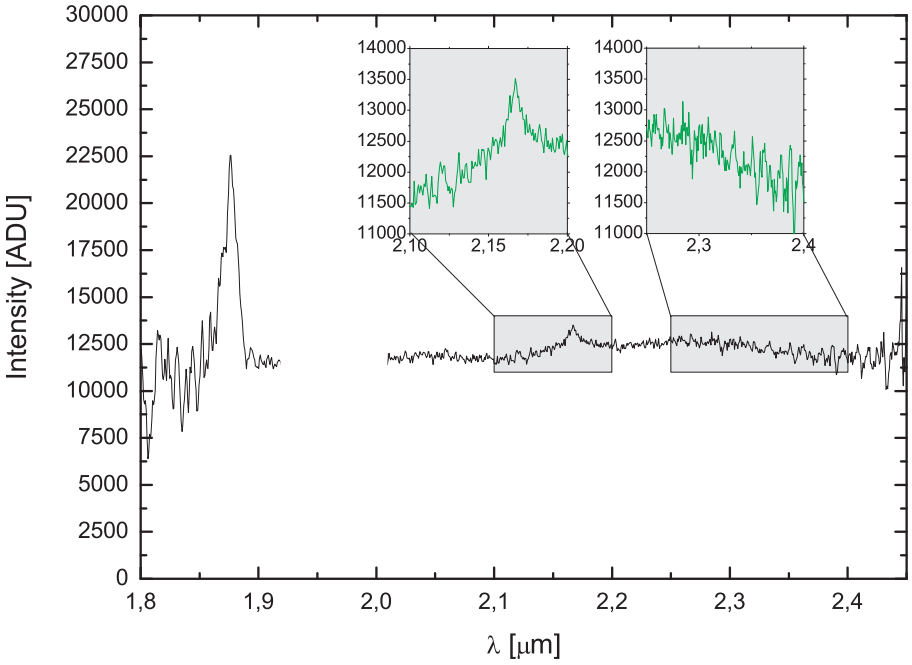

Figure 5.21: *The over 7.7″ (= 12.2 kpc) integrated spectrum of VCV(2001) J204409.7-104324. In addition to the overall K-band spectrum, the region of the Brγ line as well as the CO absorption are shown.*

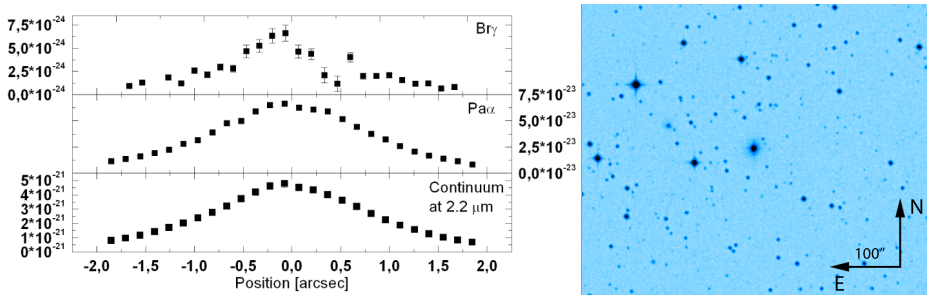

Figure 5.22: *Flux of VCV(2001) J204409.7-104324. The flux of the Brγ and the Paα line is given in units of W m^{-2}, the continuum flux is in units of W m^{-2} μm^{-1}. On the right, a DSS2(red) image of the galaxy's large scale environment is shown.*

colors of an ordinary in-active galaxy and consistent to our findings of a very strong non-stellar contribution. In their long term monitoring of the object, strong variations of ΔJ=0.65^{mag} and ΔK=0.62^{mag} were detected. Collins et al. (2004) find strong absorption in O*IV* and column densities of multiple ionization stages of silicon (Si*II*, *III*, and *IV*) and Carbon (*II*, *III*, and *IV*) which are interpreted as a multiphase medium containing both collisionally ionized and photoionized gas in the bulge.

Broad Paα and Brγ lines can be seen in the spectra. The broad component of the Paα line shows a width of 2353 km s^{-1}±20%, the width of the Brγ line is estimated to a similar value of 2009 km s^{-1}±30%, both being typical for a narrow line Seyfert 1 galaxy. The continuum slope indicates rather strong nuclear influences even at a distance of 2.4kpc from the nucleus, but the seeing during the observations was not very good with 2.6″.

5.5 Summary and conclusions

The Nearby Borderline QSO sample is well suited for spatially resolved studies of AGN. The close distance of the objects allows for a photometric detection of the host galaxy even with only very short observation times. Low resolution spectroscopy of the stellar CO absorption band can give an upper limit to the central enclosed mass and first limited information on the dominating stellar population. The results of our observations can be summarized in the following points:

1. The dominating morphological class in this sample are disk dominated galaxies. Four of the nine hosts show a bar structure and spiral arms. Only one galaxy is found to be an elliptical galaxy. An underrepresentation of ellipticals is consistent with the results of other samples (e.g. Smith et al. 1986; McLeod & Rieke 1995; Taylor et al. 1996; Schade et al. 2000; Jahnke et al. 2004), since most of the observed sources are lower luminosity AGN and the probability to find an underlying disk-dominated host galaxy increases with lower luminosity nuclei.

2. In at least two galaxies, the appearance suggests that these objects are interacting galaxies, in one galaxy a possible second nucleus is found. This supports the theory that nuclear activity may be triggered by merger events.

3. Seven of the nine galaxies show hydrogen recombination lines in either Paα, Brγ or both. In three cases, the Paα line shows a composition of a

broad and a narrow component, while in two cases only a broad component and in HE 0853-0126 only a narrow component is observed. For HE 2211-3903, the shape of the Paα line points to more complicated kinematics.

4. Three galaxies show extended molecular hydrogen emission in the 1-0S(1) transition. This appears to be a lower detection rate of Seyfert 1 galaxies with molecular hydrogen emission lines in comparison to the findings of other surveys (e.g. Rodríguez-Ardila et al. 2004). For significant conclusions, though, a larger sample size is needed.

5. In five galaxies, stellar CO absorption is detected. With the exception of HE 1328-2508, all sources show a strong increase of the CO-equivalent width with growing distance to the center. In HE 1328-2508, HE 1029-1831 and HE 1013-1947, the CO(2-0)-equivalent width resembles the value found in ordinary elliptical or spiral galaxies. In HE 1248-1356, the value can be associated to ongoing star formation. Only in the case of HE 1248-1356, the CO absorption allowed a determination of an upper limit to the central enclosed mass.

6. The continuum slopes show a correlation to the detectability of the CO-absorption. In galaxies with significant reddening, the CO-absorption is diminished by the strong non-stellar continuum.

7. In the $J - H/H - Ks$ 2-color diagram, the Seyfert galaxies are broadly distributed over the region between normal galaxies and Quasars.

8. The $H - Ks$ colors of the spiral hosts are typical for their non-active counterparts or slightly redder.

CHAPTER 6

SINFONI observations of HE 0036-5133

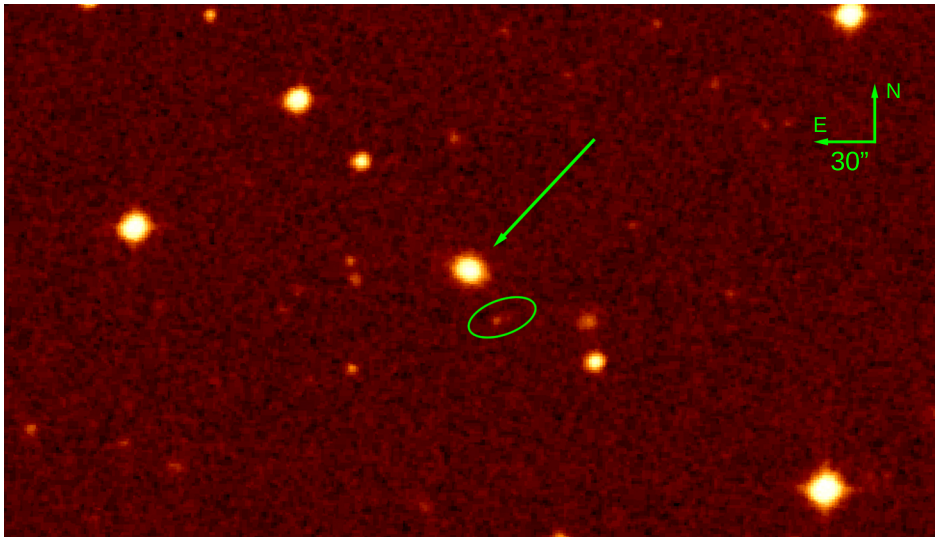

Figure 6.1: *The optical image shows the environment of HE 0036-5133 which is marked by the green arrow. In the direct vicinity, a faint extended companion can be guessed (indicated by the ellipse, but no redshift information is available for this source). Most of the bright, point like objects in the image, however, are probably foreground stars. DSS2 (red) image.*

Chapter 5 showed how difficult it is to spectroscopically disentangle contributions of an AGN and its host galaxy, even for very nearby objects. Bad seeing dilutes host and AGN properties significantly, and in the case of long slit spectroscopy, information of the host galaxies is limited to the (spatially) very outer regions of the spectra. Hence, appropriate quality spectra always require long integration times. To spatially resolve the spectroscopic features of a host galaxy has only recently become feasible (in reasonable amounts of integration time), with the establishment of integral field units which provide imaging and spectroscopy of an object simultaneously.

In this chapter, I present H+Ks-band imaging spectroscopy data on the cen-

tral 3"of HE 0036-5133, obtained with the spectrograph for integral field observations in the near infrared (SINFONI, Eisenhauer et al. 2003).

The use of SINFONI yields several advantages over mere imaging or spectroscopy. Integral field data provides spectral information for each of the spatial pixels forming the FOV. With the help of adaptive optics (AO)[26], the influences of the AGN are reduced to the (almost) diffraction limited, central point source. An upper limit estimate of the performance of the AO is provided by the extent of narrow emission lines, since these are supposed to originate in the galaxy's point like nuclear region.

For our sample of nearby borderline Sy1 QSOs we do not expect to resolve significant kinematics, since type-1 objects exhibit rather a face-on view of the hosts. Nevertheless, in order to get an impression of the feedback between host galaxy and the AGN, the spatial distribution of emission lines, absorption lines and continuum together is a crucial tool to be analyzed.

6.1 HE 0036-5133

HE 0036-5133, also known as WPVS007, is classified as a Seyfert 1 (Winkler et al. 1992) and as a narrow-line Seyfert 1 (Grupe et al. 1995) via optical spectroscopy, with a redshift of z = 0.0288 (comoving radial distance = 113 Mpc). Known optical and NIR magnitudes are V=15.6 (Grupe et al. 1995), and J=13.34±0.06, H=12.74±0.09, K=11.93±0.07 (2MASS), resulting in the NIR colors of $J - H = 0.6$ and $H - K = 0.8$, which places the object in the middle between regions occupied by Quasars and elliptical galaxies in the NIR-2-color diagram (c.f. Figure 5.4).

HE 0036-5133 is known to be an X-ray transient source. In 1990, the ROSAT All-Sky Survey (RASS) detected a peak luminosity of $L_X > 10^{43}\,\mathrm{erg\,s^{-1}}$, comparable to bright Sy 1 galaxies, while ROSAT pointed follow-up observations in 1993 detected a luminosity of only $L_X \sim 10^{40-41}\,\mathrm{erg\,s^{-1}}$ (Grupe et al. 1995), similar to values found in low luminosity AGN (LLAGN). Besides this longterm soft X-ray variability, soft X-ray variability on a time scale of days has been observed. HE 0036-5133 has the steepest AGN spectrum found in the RASS ($\alpha_{softX} \simeq -7$), neither internal absorption on cold gas nor a hard X-ray tail are

[26]The seeing (Chapter 5.1) significantly affects the image quality of ordinary ground-based telescopes: distortion blurs out any structure in objects which have angular scales of less than about one arcsecond during exposures. In AO systems, the deformation of the distorted wavefront (of a nearby natural or artificial guide star) is monitored by a wave front sensor. This information is analyzed and delivered to a deformable mirror which can compensate for the distortion. Ideally, the resulting wavefront in the telescope is planar again, and a point source is imaged with diffraction limited resolution.

detectable. Grupe et al. (1995) suggest a thermal origin of the X-rays, favoring a low mass black hole with high (near Eddington) accretion during the RASS observation. The reason for the turn off remains mysterious, with various possible reasons such as obscuration, change in accretion rate, or change in the nature of radiative transfer. Follow up CHANDRA observations in 2002 (Vaughan et al. 2004) showed no significant change in the X-ray emission in comparison with the Grupe et al. (1995) observations. The existence of long-lasting, high ionization optical line emission from the nucleus of HE 0036-5133 further suggests that it may harbor some kind of long-lived AGN (Crenshaw et al. 1999).

6.2 Observations, data reduction and calibration

HE 0036-5133 was observed in the night of the 14th of August, 2005. The AO guiding was carried out on the nucleus of HE 0036-5133. The average seeing was around 1.1". The 100 mas pixel scale with FOV of 3" × 3" was used (2 pixel=100mas). The observations were performed in the H+Ks band with an integration time of 24 minutes. The same time was spent on the sky. In this mode, a spectral resolution of $R_{H+K} \sim 1500$ is achieved. Successive object (O) and sky (S) observations (OSSO) were acquired to produce sky-subtracted frames.

Using small mirrors, SINFONI slices the 2D image on the sky into 32 slitlets, which are then imaged onto a pseudo-slit and dispersed onto the 2k×2k detector. The reduction of the data and reconstruction of the 3D cubes were carried out similar to Zuther et al. (2007), using ESO's SINFONI instrument pipeline in combination with GASGANO[27], IDL, and QFitsView[28]. Bad pixel, cosmic rays, and flat field corrections were applied to the 2D raw frames. The 3D cubes were reconstructed using calibration frames for the slitlet distances and the light dispersion. Wavelength calibration was performed using calibration lamp spectra. The telluric absorption was accounted for similar to the ISAAC observations (Chapter 5) by the use of intermediate standard-star observations (near in both time and airmass to the target exposures) of a G2V star (HD 14398). In contrast to the telluric stars used during the ISAAC observations, a G2V star has plenty intrinsic features in the H- and K- band, hence prior division by an atmospheric-transmission-corrected solar spectrum (i.e. a very well characterized G2V star, Maiolino et al. 1996) and interpolation with a black body with a temperature of 5800 K was applied in the range of reduced atmospheric transmission between the H- and K- band

[27] www.eso.org/sci/data-processing/software/gasgano

[28] written by Thomas Ott (MPE Garching, www.mpe.mpg.de/ ott/QFitsView).

Flux calibration was performed using 2MASS (H- and) K-band images, ignoring a possible variation of the source. It showed that applying separate flux calibrations to H- and K- band resulted in a steep drop of the spectrum from H- to K-band. Hence, the less extended K-band flux calibration was applied onto the H-band data for more consistent results. The SINFONI data cube was calibrated such that, after being convolved with the 2MASS K-band filtercurve, the collapsed 2D K-band image matches the total 2MASS K-band flux (i.e. $1.12 \cdot 10^{-2}$ Jy). This assumes that the object is completely resolved in the 3"×3" SINFONI FOV, which was taken into account by a factor of 100 (angular size 0.3"/3.0"). However, relative line ratios are our prime objective, and here the error is dominated by the noise in the spectra. In addition, corrections for airmass and galactic extinction according to Schlegel et al. (1998) were applied. For the analysis, only features exceeding 3σ are considered.

6.3 Continuum and emission lines

Figure 6.2 shows the spectrum of HE 0036-5133, integrated over a variable, circular aperture with a radius corresponding to 3×FWHM(PSF). Various lines are detected in the spectrum, strongest being the Hydrogen recombination lines[29] Paα and Brγ. Line maps of these two lines, together with H- and K-band continuum maps, are presented in Figure 6.3. Considering that the Paα and Brγ emission is concentrated in the nuclear component, their line maps yield information on the AO performance and the achieved spatial resolution. For Paα, a Gaussian fit results in a FWHM of 6.6 pixels along the major axis and 5.9 pixels along the minor axis, i.e. ∼0.31". The Brγ line map shows a FWHM of 0.27" (major) and 0.24"(minor).Accordingly, the datacube achieves a spatial resolution of ∼140 pc (1"≃0.534 kpc at z=0.0288) at 2.2 μm, but it also shows that this value is wavelength dependent and becomes worse towards shorter wavelengths. A rough estimate of 200 pc for the H-band is a reasonable assumption, as line maps of the (weaker) recombination lines in the H-band show.

The morphology of the Hydrogen recombination lines is unresolved and centered on the nucleus of HE 0036-5133. The spectral width of the Paα line, derived from the 3FWHM Paα line map, is 1380±80 km s^{-1} (FWHM=(9.0±0.4) nm at (1875.0±0.1) nm and corrected for a spectral resolution of R=1572.8). The line width suggests that HE 0036-5133 is a NLS1 galaxy, consistent with the optical classification.

Most of the H- and K- band continuum is similarly concentrated on the

[29]For a discussion of the possible excitation mechanisms of Hydrogen recombination lines see Section 5.2.1.

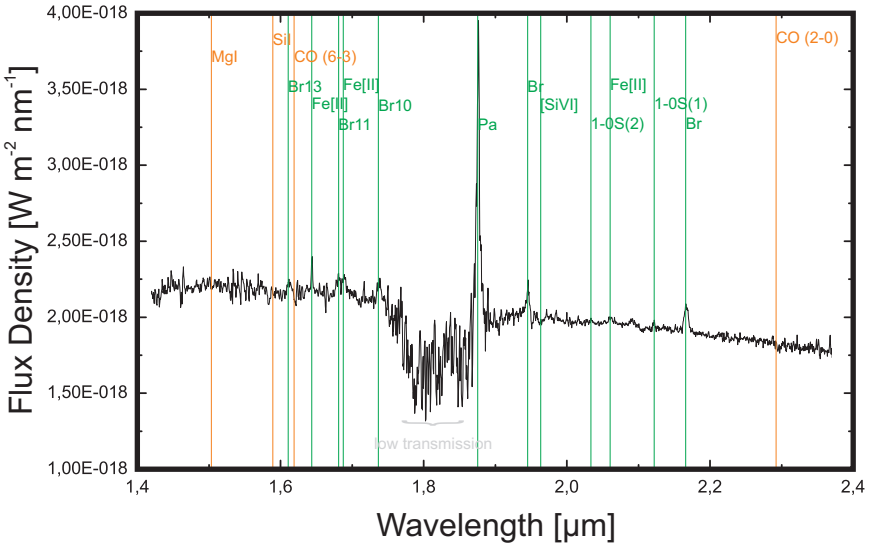

Figure 6.2: *Integrated spectrum of HE 0036-5133. Various emission (green) and absorption (orange) lines are labeled.*

galaxy's core, but in particular the *H*-band continuum shows an extended component along the NE-SW direction.

Integrated line fluxes of all detected emission lines are presented in Table 6.1. The derived line ratios of the recombination lines (Table 6.2) all agree with an unobscured case-B recombination scenario (Osterbrock 1989). The errors in the measured line-fluxes are too high to determine gas temperature and densities. The absence of significant extinction HE 0036-5133 is in agreement with the optical spectrum (Grupe et al. 1995). The spatial distribution of the Paα/Brγ line ratio is shown on the left of Figure 6.4. Where detected, the line ratio stays uniform throughout the center, again supporting the unobscured theme. In addition to the recombination line ratios, the continuum yields information on the reddening. Figure 6.4 also shows flux ratios derived from *H*- and *K*-band continuum, for broad (i.e. (1.4-1.8μm)/(1.85-2.35μm), middle image) and narrow (1.6μm/2.2μm, right image) wavelength regions. The *H*- and *K*-band continuum ratios reflect the H-K color information. Both maps indicate a red continuum in the central region compared to off-central regions. Moreover, the red continuum extends in the NW-SE direction, perpendicular to the *H*-band extent (c.f. Section 6.4 and Figure 6.5). In combination with the fact that no significant obscuration is detected, this red continuum can fully be attributed to re-radiation of hot dust.

Drawing detailed conclusions on the excitation mechanisms of the molecu-

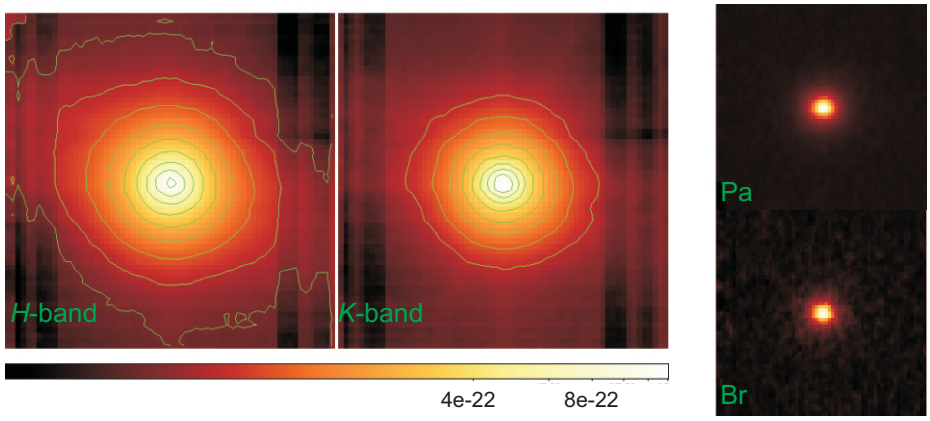

Figure 6.3: *Left and middle image: H- and K-band continuum maps. In both images, contours range from $1 \cdot 10^{-23}$ - $20 \cdot 10^{-23}$ W m^{-2} nm^{-1}. The H-band continuum clearly resolves an extended component which is weakly off-centered from the nucleus in the NE and SW regions. The thermally dominated K-band is more point-like and concentrated on the nucleus. The two images on the right show continuum subtracted Paα and Brγ line maps. The recombination lines are unresolved point sources, with a spatial FWHM of 0.3"(Paα) and 0.25"(Brγ) respectively. Each of the four images shows the full SINFONI FOV of 3"×3". The dark, vertical pixel columns in the continuum images are artifacts of the data reduction.*

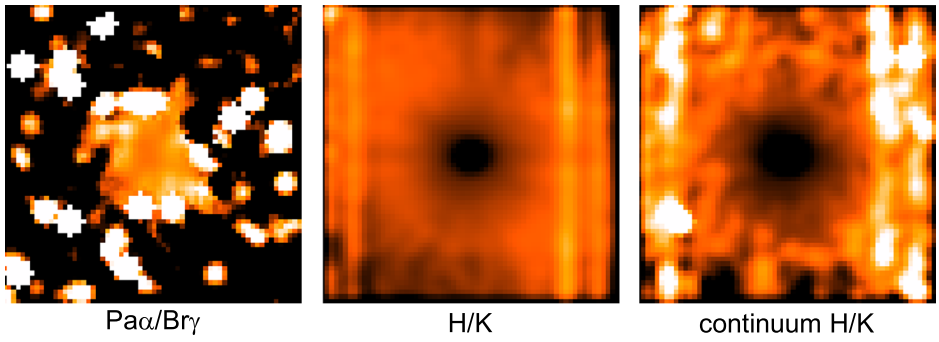

Figure 6.4: *Different reddening maps. The image on the left displays the reddening map deduced from the Paα/Brγ line ratio, in the middle a broad band H-band/K-band ratio (i.e. color map), and on the right the distribution of the ratio of the effective H-band and K-band wavelengths (1.6μm/2.2μm) is shown. All images are smoothed with a 3×3pixel Gaussian.*

lar Hydrogen is useless due to only the 1-0 S(1) line being detected. However, we can use the characteristic NIR line ratio diagram (Rodríguez-Ardila et al. 2005), which compares line ratios of H_2/Brγ with [FeII]/Paβ. The here considered [FeII](λ1.257) line and the Paβ line both fall into the J-band and are not accessible with our observations, but we can rely on the [FeII](λ1.644)/Brγ line ratio instead. In starburst galaxies the value of this ratio typically falls in the range 0.5-2 (Simpson et al. 1996), in agreement with the starburst models of Colina (1993) which predict ratios between 0.1 and 1.4. In these objects, the [Fe II] emission originates in supernova-driven shocks (Mouri 1994). AGN usually show larger values of [Fe II]/Brγ than starburst galaxies. The [FeII](λ1.644)/Brγ line ratio of 0.37±0.01 found in HE 0036-5133 indicates that most of the [FeII] emission is attributed to star formation. [FeII] and H_2 probably originate in different parcels of gas, but can be dominated by the same excitation mechanisms (Rodríguez-Ardila et al. 2004). The weak H_2 line detected in HE 0036-5133 results in a value of log(1-0S(1)/Brγ)=-1.16±0.04. This value is considerably different from values expected for LINERS or Seyfert galaxies[30], and our ratio is typical for a photoionization scenario - which again supports that these emission lines originate in nuclear star formation (starbursts have line ratios log(1-0S(1)/Brγ) <-0.3).

In general, [FeII] and H_2 emission could be produced by (hard) X-ray heating. No hard X-ray component was detected in HE 0036-5133. Together with our result that the [FeII] and H_2 emission can be attributed to nuclear star formation, this supports the theory that there is no/only a very weak hard X-ray source in this NLS1 (Grupe et al. 1995).

The morphology of the [FeII] and H_2 lines is, similar to the recombination lines, point-like and unresolved.

Supposing that the recombination lines are excited due to star formation triggered photo-ionization, we can calculate star formation rates (SFR) from the line fluxes of Paα and Brγ. We adopt the calibration introduced by Panuzzo et al. (2003), following Valdés et al. (2005)[31]:

$$\mathrm{SFR(Pa}\alpha) = 5.06 \cdot 10^{-41}\, L(\mathrm{Pa}\alpha)\, M_\odot\, yr^{-1}/(erg\, s^{-1})$$

$$\mathrm{SFR(Br}\gamma) = 6.60 \cdot 10^{-40}\, L(\mathrm{Br}\gamma)\, M_\odot\, yr^{-1}/(erg\, s^{-1}).$$

The deduced star formation rate values are $\mathrm{SFR}_{\mathrm{Pa}\alpha} = 3.0 \pm 0.2\, M_\odot\, yr^{-1}$ and

[30] LINERS, which are interpreted to be dominated by shock excitation, show line ratios of >2, Seyferts 0.4-2 (Rodríguez-Ardila et al. 2004).

[31] These calculations refer to a Salpeter IMF between 0.1 $M_\odot$ and 120 $M_\odot$ and take into account an increment of 16% due to the lower IMF limit with respect to the value of 0.15 $M_\odot$ from Panuzzo et al. (2003).

$SFR_{Br\gamma} = 3.2 \pm 0.3\, M_\odot\, yr^{-1}$. Since the SFR is calculated from absolute flux values, the error in the flux calibration becomes important here (c.f Section 6.2) and the actual uncertainty in the SFR is significantly higher than the calculations suggest. Nevertheless the SFR is not high. Typical values found in luminous and ultra-luminous infrared galaxies (LIRGs, ULIRGs) range from tenths to hundreds $M_\odot\, yr^{-1}$.[32] However, those values give star formation rates for the whole galaxies. Our SFR is limited to the central $\sim$ 140 pc, and is comparable to the star formation deduced from Hα in normal spiral galaxies (Kennicutt 1983).

With respect to the X-ray properties of HE 0036-5133, the non-detection of [SiVI] (λ1.962μm) is interesting. This coronal line is uniquely associated with Sy 1 and Sy 2 nuclei, and can only be produced by photoionization by a hard (X-ray/UV) continuum (Marconi et al. 1994). It is used as a tracer of Seyfert activity even in obscured Sy 2 nuclei, e.g. Oliva & Moorwood (1990) report detection of strong [SiVI] emission in NGC 1068, despite its heavily obscured nucleus. Due to the redshift of HE 0036-5133, the [SiVI] feature falls into a wavelength range of low atmospheric transmission. However, our telluric standard corrected for this effect exceptionally well and the noise in the spectra is comparable to the wavelength region surrounding the Brγ feature. The non detection of this feature is in striking conformity with the non detection of a hard X-ray component and supports the theory that this hard X-ray component really is absent in the nucleus of HE 0036-5133.

6.4 Absorption lines

In addition to the emission lines which all can be attributed to the nuclear starburst, several stellar absorption lines are detected in the spectrum of HE 0036-5133. In principle, these allow for an estimate of the stellar content, although possible influences of an underlying continuum have to be considered (c.f. Chapter 5.2.3). To allow a comparison of the absorption depth to other galaxies, we consider equivalent widths (EWs), which compare the stellar absorption in the respective line to the surrounding continuum. Three stellar absorption features can be spotted, MgI(λ1.5040), CO(6-3) and CO(2-0), in addition a very weak SiI(λ1.5890) absorption can be found. The definition of the respective EWs is presented in table 6.3.

[32] Deduced from Paα and Brγ. Goldader et al. (1995) as well as Valdés et al. (2005) report a photon deficit of SFR values calculated from NIR lines when compared to SFR_{IR}. In extreme cases, less than 10% of the star formation are detected in the NIR. However, their samples are based on LIRGs and ULIRGs and it is suggested that extinction can explain the missing photons in the NIR, so these influences may not be as significant for HE 0036-5133.

Table 6.1: *Line fluxes of various emission lines measured in the integrated H+Ks band spectrum. For 1-0S(2) and [FeII] (λ2.06059), only upper limits can be given. The flux has always been extracted in an aperture of 3×PSF FWHM of the respective line map.*

	λ [μm]	Flux [$10^{-18}\ Wm^{-2}$]	Flux error [$10^{-18}\ Wm^{-2}$]
Br13	1.61137	0.73	0.03
[FeII]	1.64406	1.21	0.03
Br11	1.68111	*blended*	
[FeII]	1.68778	*blended*	
Br10	1.73669	1.5	0.03
Paα	1.87561	39.6	0.1
Brδ	1.94509	2.4	0.03
1-0S(2)	2.03376	< 0.02	
[FeII]	2.06059	< 0.02	
1-0S(1)	2.12183	0.23	0.01
Brγ	2.16612	3.24	0.02

Table 6.2: *Emission line ratios (c.f. Table 6.1). In addition, two more extreme theoretical values for case B recombination (according to Osterbrock 1989) are given for the recombination line ratios.*

Lines	Ratio	Theoretical value	
		$N \sim 10^2\ cm^{-3}$ 5000 K	$N \sim 10^4\ cm^{-3}$ 10000 K
Paα/Brγ	12.2 ± 0.1	12.4	12.1
Paα/Brδ	16.2 ± 0.1	19.2	18.4
Br10/Paα	0.039 ± 0.001	0.025	0.028
Br10/Brγ	0.47 ± 0.01	0.318	0.33
Brδ/Brγ	0.76 ± 0.01	0.65	0.68
[FeII](1.644)/Brγ	0.37 ± 0.01		
log(1-0S(1)/Brγ)	-1.16 ± 0.04		

Table 6.3: *Definition of equivalent widths. References:* [1]*: Kleinmann & Hall (1986),* [2]*: Origlia et al. (1993),* [3]*: Ivanov et al. (2004).*

Line	λ [μm]	$\Delta\lambda$ [μm]	Continuum [μm]	Reference
^{12}CO (2-0)	2.2957	0.0052	2.2873-2.2925	[1]
^{12}CO (6-3)	1.61975	0.0045	1.6145-1.6175, 1.6255-1.6285	[2]
Si I	1.5890	0.0040	1.5830-1.5870, 1.5910-1.5950	[2]
Mg I	1.5040	0.0040	1.4990-1.5020, 1.5060-1.5090	[3]

The spatial distribution of all detected absorption features varies strongly with the position in the galaxy (Figure 6.5). In general, the EWs become smaller towards the nucleus. This is caused by the same red continuum that can be seen in the continuum-reddening maps (Figure 6.4 middle & right). Of particular interest is the NW-SE extend of a red continuum which can be seen in the decrease in EWs. This trend is detected in all 3 stellar absorption lines. A weak correspondence can already be spotted in the reddening maps, but it is much more pronounced in the EWs of the stellar absorption features. We interpret this as significant contribution of warm dust ($\sim$ 1200 K), which is in agreement with the findings of other studies of QSOs and Sy 1 (Riffel et al. 2006; Glikman et al. 2006); e.g. Boisson et al. (2002) conclude from H-band spectra of 5 Seyfert galaxies that a significant dust component is characteristic of type 1 AGN, while Seyfert 2 galaxies show no dust reddened continuum. Nevertheless, its strong influences on the H-band absorption lines ($\lambda < 1.7\,\mu$m) are surprising (c.f. Oliva et al. 1995).

This dust component probably is evidence for a hidden, nuclear bar. Nuclear bars are thought to be important tools to allow dust-infall into the nuclear region of galaxies (Shlosman et al. 1989), possibly driving both nuclear star formation and feeding the nuclear supermassive black hole. Martini et al. (E.g. 2003) report that barred galaxies show significantly less frequent ring structured nuclear regions, suggesting that bar-driven inflow does not commonly stall in a circumnuclear ring. The detailed connection between bars and AGN-activity, however, is still under evaluation (e.g. nuclei-of-galaxies, NuGA, studies).

In the regions where CO absorption can be detected (i.e. NE and SW of the nucleus), the equivalent widths have mean values of $\mathrm{EW}_{CO(2-0)} = 8.5 \pm 0.6$ Å and $\mathrm{EW}_{CO(6-3)} = 5.1 \pm 0.8$ Å. Both values are typical for early M giants/supergiants (Origlia & Oliva 2000). This result can be interpreted as either

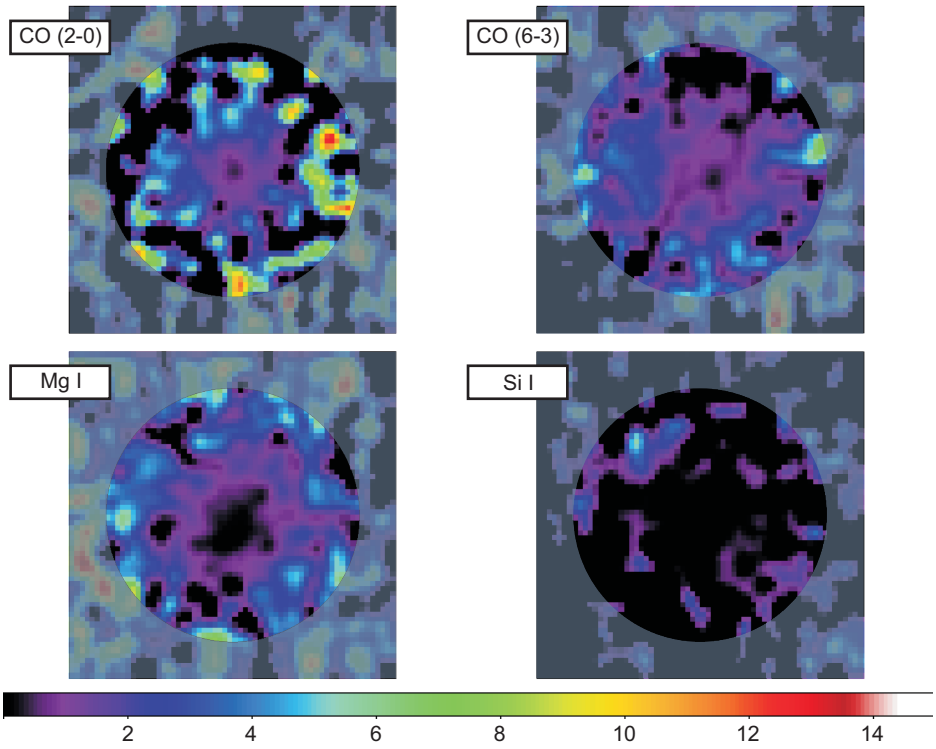

Figure 6.5: *Spatial distribution of the equivalent widths (EW, in Angstroms) of the stellar absorption lines. The images are smoothed with a 3pixel FWHM Gaussian, and regions with insufficient S/N are grayed out.The EWs of CO(2-0), CO(6-3) and MgI all show a decrease towards the central region as well as in NW/SE direction, very similar to the H/K reddening maps of Figure 6.4.*

an indication of an old and metallic bulge population similar to that of elliptical galaxies (being mostly red giants), or members of a few Myr old starburst (being mostly red supergiants). Following Oliva et al. (1995), the line ratio $\log(\mathrm{EW}_{CO(6-3)}/\mathrm{EW}_{CO(2-0)})$ of -0.21±0.17 in combination with the $\mathrm{EW}_{CO(6-3)}$ indicates that dilution by a red continuum is small in these regions. Hence an old bulge population seems to be more reasonable as origin of the CO absorption. Unfortunately, the SiI feature is too weak to be detected in a spatially resolved way and we cannot determine the temperature-sensitive $\log(\mathrm{EW}_{CO(6-3)}/\mathrm{EW}_{SiI})$ ratio to deduce the amount of underlying continuum in the procedure described by the same authors. With respect to the decrease in equivalent width towards the center, it should be noted that they report that NIR stellar absorption features become unmeasurable with a contribution of an underlying continuum of more than 90% (which is, of course, also depending on the S/N in the spectra).

6.5 Conclusions

The results of our SINFONI data on HE 0036-5133 can be summarized in the following points:

- [FeII] and molecular Hydrogen are clearly dominated by excitation mechanisms attributed to star formation. No signs of AGN influences can be found.
- The Hydrogen recombination lines show no direct evidence of reddening. Deduced nuclear star formation rates are moderate. Line-widths are typical for a narrow-line Sy 1.
- Stellar absorption lines and continuum-reddening maps both indicate a significant contribution of a red continuum at the center. In addition, these features reveal a nuclear bar. CO absorption features point to an old bulge component.

In combination, these arguments lead to a qualitative model of the central kpc of HE 0036-5133 that is schematically presented in Figure 6.6.

Several studies of NLSy1 (e.g. Komossa & Xu 2007, and references therein)[33] suggest that narrow-line Sy 1 galaxies have lower-mass massive black holes, but accrete at accretion rates larger than the average value appropriate to Sy 1 galaxies. HE 0036-5133 fits well into this picture, because it explains the NIR/optical

[33] Although, these studies have recently been questioned by new studies which explain NLSy1 by orientation effects (Decarli et al. 2008).

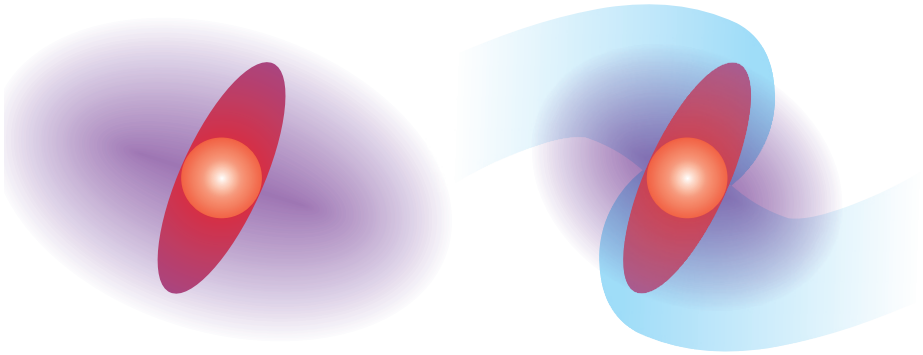

Figure 6.6: *Two schematic models for the central kiloparsec of HE 0036-5133. The core region is dominated by emission lines attributed to star formation and continuum emission of warm dust. Additional dust emission is detected in the form of a nuclear bar that extends ∼500 pc in the NW/SE direction. The absorption lines indicate the presence of an old stellar bulge component. The H-band contours show that the NE and SW extend both are not exactly centered on the nucleus. This, together with the rather blue color (the large extend and the asymmetry are not detected in the K-band), could suggest that there are two spiral arms attached to the nuclear bar (displayed on the right).*

classification and the quiescent phase X-ray emission. However, I have to remark that the broad recombination lines are the only sign of AGN activity in our NIR data. Historically, a broad component of Brα and He lines with a FWHM of $\geq$ 1000 km s^{-1} had also been reported for the galactic center in our Milky Way galaxy, but later it was shown that this line width could be attributed to strong stellar winds of He-stars (Hall et al. 1982; Geballe et al. 1984).

Only the integral field data made the revelation of the nuclear bar possible. The presence of the bar agrees well with the theme of nuclear bars feeding nuclear star formation and the AGN. In order to allow gas infall from the outskirts of a galaxy to the center, it is necessary to lose angular momentum, and interaction and nuclear bars both provide necessary non-axial symmetric gravitational potentials. The fact that the nuclear bar is so well hidden in the galaxy, however, could imply consequences on the results of studies analyzing bar fractions in AGN samples in the optical or NIR (e.g. Malkan et al. 1998; Knapen et al. 2000). If conducted with instruments like SINFONI, the fraction of bars could become higher than initially suggested. In addition, the data shows prominently the success of the approach of the nearby QSO sample: At higher redshifts, the detection of such embedded nuclear bars quickly becomes unfeasible.

Back matter

Glossary

AGN	Galaxies are classified as Active Galactic Nuclei (AGN) if showing energetic properties in their central regions that cannot be described by pure stellar radiation.
LINER	Low-ionization nuclear emission-line region galaxies represent a very low luminosity class of AGN. Spectroscopically similar to Sy 2, with relatively strong low-ionization lines (e.g. [OI]λ6300Å), LINERs are very common and might be present in nearly half of all spiral galaxies. They can be distinguished from normal HII regions and AGN on the basis of emission line ratios.
Quasar/QSO	Quasars represent the most luminous subclass of AGN, with nuclear magnitudes $M_B < -21.5 + 5 \log h_0$. In the late 1950s, quasi stellar objects (QSOs) were distinguished from Seyfert galaxies by being generally spatially unresolved on the images of the Palomar Sky Survey, resulting in a maximum angular size of <1". Today, quasars can be classified by their SED. In contrast to stars or normal galaxies AGN cannot be described by thermal emission. The broad band SED can be described by $F_\nu \sim \nu^{-\alpha}$ with α being the power-law index or spectral index and F_ν the specific flux, usually given in units of $W\,m^{-2}\,Hz^{-1}$ or Jy (=Jansky, 1Jy= $10^{-26} W\,m^{-2}\,Hz^{-1}$). A positive spectral index then characterizes a source whose flux density decreases with increasing frequency. Typical values of α range between 0 and 1.

Radio galaxy	Strong radio sources are typically identified with giant elliptical galaxies (including quasars). The assignment to elliptical galaxies rather than to spirals is an important difference to Seyfert galaxies, as in terms of basic phenomenology, radio galaxies can be seen as radio loud Seyfert galaxies.
Seyfert galaxy	Seyfert galaxies have a absolute brightness of $M_B > -21.5 + 5 \log h_0$ and represent lower luminosity AGN. A Seyfert galaxy has a quasar like nucleus, but also a clearly detectable host galaxy (in the optical $L_{Host} \approx L_{nucleus}$, typically $\sim 10^{11} L_\odot$). Seyfert I and Seyfert II galaxies differ in the broadness of emission lines, i.e. Sy I show a superposition of permitted broad (FWHM$> 1000\,\mathrm{km\,s^{-1}}$) and forbidden narrow (FWHM$\sim 500\,\mathrm{km\,s^{-1}}$) emission lines, whereas emission lines in Sy II show only narrow components. In addition, narrow line Seyfert I (NLS1) galaxies are distinguished from Seyfert I galaxies, if the broad component shows a width of $\leq 2000\,\mathrm{km\,s^{-1}}$.
Starburst galaxy	Similar to AGN, galaxies can have rather blue colors, strong, HII-region-type emission line spectra and strong radio emission, if recent, large scale star formation occured. Emission lines are produced ub the star burst by a large number of O and B stars, and the radio emission is caused by super nova remnants. Sometimes, the starburst takes place in an unresolved region at the galactic center, appearing similar to an AGN. There are theories predicting an evolution from starburst to AGN, while other theories suggest that AGN and starburst are two different manifestations between an identic phenomenon.

ULIRG	Ultraluminous infrared galaxies emit a substantial fraction of their energy in the far infrared. ULIRGs have far-infrared luminosities of $L_{8-1000\mu m} \geq 10^{12} L_{\odot}$ and exceed their optical luminosities by a factor of 10 or more. The far-infrared emission in these galaxies is caused by thermal radiation from dust (T~100 K or less) that is heated either bay massive star formation or by a 'hidden' AGN which cannot be observed directly through the dust.
Unified scheme	The difference in type 1/2 AGN can be explained by different viewing angles between line of sight and the rotational axis of the host galaxy/jet.Basic components of this model are: A supermassive black hole ($10^6 - 10^{10}\, M_{\odot}$); a small ($< 1$ pc), hot accretion disk around the SMBH, origin of the strong UV and otical continuum emission; gaseous clouds, moving around the SMBH and being ionized by the central source - ensemble clouds closer to the center show broad emission lines due to their higher velocities; molecular gas and dust, assembled in a dusty torus with a symmetry axis aligned with the direction of the jet, blocking the view to the center if viewed edge-on, and with temperatures of 1500 K origin of the observed infrared thermal radiation; two highly collimated jets, origin of the synchrotron radiation.

Abbreviations

ACS	Advanced Camera for Surveys
AGN	active galactic nucleus
AIV	assembly, integration and verification
AO	adaptive optics
BLR	broad line region
CAD	computer-aided design
CDR	critical design review
CEA	Commissariat à l'Énergie Atomique
CFRP	carbon fibre reinforced plastic
CSA	Canadian Space Agency
CSL	Centre Spatial de Lige
DM	Demonstration Model
DPA	Double Prism Assembly
EC	European Consortium
ECSS	European Cooperation for Space Standardization
ESA	European Space Agency
ESO	European Southern Observatory
EW	equivalent width
FGS	fine guidance sensors
FM	Flight Model
FOV	field of view
FPM	Focal Plane Module
FS	Flight Spare
FWHM	full width at half maximum
GEM	geometric elements method
HES	Hamburg ESO survey
HR1	ROSAT hardness ratio
HST	Hubble Space Telescope
ICE	Instrument Control Electronics
ICP	Interface Connector Panels
IFU	integral field unit
IMF	initial mass function
IOC	Input Optics & Calibration

ISAAC	Infrared Spectrometer and Array Camera
ISIM	Integrated Science Instrument Module
ISO	Infrared Space Observatory
JWST	James Webb Space Telescope
LIRGs	luminous infrared galaxies
LLAGN	low luminosity AGN
LOSVP	line-of-sight velocity profile
LRS	low resolution spectroscopy
LRSDPA	Low Resolution Double Prism Assembly
MIR	mid infrared
MIRI	Mid Infrared Instrument
MIRIM	MIR-imager
MRS	medium resolution spectrometer
MTS	MIRI Telescope Simulator
NASA	National Aeronautics and Space Administration
NED	NASA/IPAC Extragalactic Database
NIR	near infrared
NIRCam	Near Infrared Camera
NIRSpec	Near Infrared Spectrograph
NLS1	Narrow line Seyfert 1
NLR	narrow line region
OTE	Optical Telescope Element
PSF	point spread function
QM	qualification model
QSO	quasi-stellar object
RASS	ROSAT All-Sky Survey
RMS	root mean-squared
ROSAT	Röntgensatellit
SDSS	Sloan Digital Sky Survey
SF	star formation
SFR	star formation rate
SINFONI	Spectrograph for integral field observations in the near infrared
SMBH	Super Massive Black Hole
SMO	Spectrometer Main-Optics
SPO	Spectrometer Pre-Optics
Sy1/Sy2	Seyfert 1/Seyfert 2
TFI	Tunable Filter Imager
ULIRGs	ultra-luminous infrared galaxies

UoC	University of Cologne
VCV	Vèron-Cetty & Vèron
VLT	Very Large Telescope
VM	Verification Model
WFE	wave front error
WMAP	Wilkinson Microwave Anisotropy Probe
WRT	with respect to
ZP	zero point

Bibliography

Amiaux, J., Alouadi, F., Augueres, J. L., Bouchet, P., Bouzat, M., Cavarroc, C., Cloue, C., Antoni, P. D., Desforges, D., Donati, A., Dubreuil, D., Eppelle, D., Gougnaud, F., Hervieu, B., Lagage, P. O., Leboeuf, D., Mer, I. L., Lussignol, Y., Mattei, P., Meigner, F., Moreau, V., Pantin, E., Perrin, P., Ronayette, S., Tauzin, G., Poupar, S., Wright, D., Glasse, A., Wright, G., Mazy, E., Plesseria, J. Y., Renotte, E., Ray, T., Abergel, A., Guillard, P., Longval, Y., Ressler, M., Reess, J. M., Hofferbert, R., Krause, O., Justtanont, K., & Olofsson, G., 2008; *Development approach and first infrared test results of JWST/Mid Infra Red Imager Optical Bench*. In J. M. Oschmann, Jr, M. W. M. de Graauw, & H. A. MacEwen (editors), *Space Telescopes and Instrumentation 2008: Optical, Infrared, and Millimeter*, volume 7010, page 70100U. Proceedings of the SPIE

Bade, N., Fink, H. H., Engels, D., Voges, W., Hagen, H. J., Wisotzki, L., & Reimers, D., 1995; *AGN from the ROSAT all-sky survey.* Astronomy and Astrophysics Supplement Series, 110:469

Bagnasco, G., Kolm, M., Ferruit, P., Honnen, K., Koehler, J., Lemke, R., Maschmann, M., Melf, M., Noyer, G., Rumler, P., Salvignol, J.-C., Strada, P., & Plate, M. T., 2007; *Overview of the near-infrared spectrograph (NIRSpec) instrument on-board the James Webb Space Telescope (JWST).* In J. B. Heany & L. G. Burriesci (editors), *Cryogenic Optical Systems and Instruments XII*, volume 6692, page 17. Proceedings of the SPIE

Barkana, R. & Loeb, A., 2001; *In the beginning: the first sources of light and the reionization of the universe*. Physics Reports, 349:125

Bertram, T., Eckart, A., Fischer, S., Zuther, J., Straubmeier, C., Wisotzki, L., & Krips, M., 2007; *Molecular gas in nearby low-luminosity QSO host galaxies*. Astronomy and Astrophysics, 470:571

Binney, J. & Merrifield, M., 1998; *Galactic astronomy*

Boisson, C., Coup, S., Cuby, J. G., Joly, M., & Ward, M. J., 2002; *Near IR spectroscopy of active galactic nuclei*. Astronomy and Astrophysics, 396:489

Bouwens, R. J., Illingworth, G. D., Blakeslee, J. P., & Franx, M., 2006; *Galaxies at z ˜ 6: The UV Luminosity Function and Luminosity Density from 506 HUDF, HUDF Parallel ACS Field, and GOODS i-Dropouts*. Astrophysical Journal, 653:53

Bromm, V., Kudritzki, R. P., & Loeb, A., 2001; *Generic Spectrum and Ionization Efficiency of a Heavy Initial Mass Function for the First Stars*. Astrophysical Journal, 552:464

Bromm, V. & Larson, R. B., 2004; *The First Stars*. Annual Review of Astronomy and Astrophysics, 42:79

Burriesci, L. G., 2005; *NIRCam instrument overview*. In J. B. Heany & L. G. Burriesci (editors), *Cryogenic Optical Systems and Instruments XI.*, volume 5904, pages 21–29. Proceedings of the SPIE

Cole, S., Aragon-Salamanca, A., Frenk, C. S., Navarro, J. F., & Zepf, S. E., 1994; *A Recipe for Galaxy Formation*. Monthly Notices of the Royal Astronomical Society, 271:781

Colina, L., 1993; *Forbidden Fe II 1.64 micron emission in high-luminosity and ultraluminous IRAS galaxies*. Astrophysical Journal, 411:565

Collins, J. A., Shull, J. M., & Giroux, M. L., 2004; *Highly Ionized High-Velocity Clouds toward PKS 2155-304 and Markarian 509*. Astrophysical Journal, 605:216

Crenshaw, D. M., Kraemer, S. B., Boggess, A., Maran, S. P., Mushotzky, R. F., & Wu, C.-C., 1999; *Intrinsic Absorption Lines in Seyfert 1 Galaxies. I. Ultraviolet Spectra from the Hubble Space Telescope*. Astrophysical Journal, 516:750

Decarli, R., Dotti, M., Fontana, M., & Haardt, F., 2008; *Are the black hole masses in narrow-line Seyfert 1 galaxies actually small?* Monthly Notices of the Royal Astronomical Society, 386:L15

Deutsch, L. K. & Willner, S. P., 1987; *Far-infrared luminosities of Markarian starburst galaxies. II - Individual galaxies*. Astrophysical Journal Supplement Series, 63:803

Doyon, R., Joseph, R. D., & Wright, G. S., 1994; *A near-infrared spectroscopic study of the luminous merger NGC 3256. 1: Constraints on the initial mass function of the starburst*. Astrophysical Journal, 421:101

Draine, B. T., 1989; *Interstellar extinction in the infrared.* In B. H. Kaldeich (editor), *Infrared Spectroscopy in Astronomy*, volume 290 of *ESA Special Publication*, pages 93–98

Dubreuil, D., Poupar, S., Dupont, P., Amiaux, J., & Augu\'erers, J.-L., 2008; *Requirements Specification for the MIRI Imager Double Prism Assembly*

Dunlop, J. S., Cirasuolo, M., & McLure, R. J., 2007; *A systematic search for very massive galaxies at z > 4.* Monthly Notices of the Royal Astronomical Society, 376:1054

Dunlop, J. S., McLure, R. J., Kukula, M. J., Baum, S. A., O'Dea, C. P., & Hughes, D. H., 2003; *Quasars, their host galaxies and their central black holes.* Monthly Notices of the Royal Astronomical Society, 340:1095

ECSS-E-30, 2000a; *Mechanical - Part 2: Structural.* ESA Publications Division

ECSS-E-30, 2000b; *Mechanical - Part 3: Mechanisms.* ESA Publications Division

ECSS-Q-70-46A, 2004; *General requirements for procurement of threaded fasteners.* ESA Publications Division

Eisenhauer, F., Abuter, R., Bickert, K., Biancat-Marchet, F., Bonnet, H., Brynnel, J., Conzelmann, R. D., Delabre, B., Donaldson, R., Farinato, J., Fedrigo, E., Genzel, R., Hubin, N. N., Iserlohe, C., Kasper, M. E., Kissler-Patig, M., Monnet, G. J., Roehrle, C., Schreiber, J., Stroebele, S., Tecza, M., Thatte, N. A., & Weisz, H., 2003; *SINFONI - Integral field spectroscopy at 50 milliarcsecond resolution with the ESO VLT.* In M. Iye & A. F. M. Moorwood (editors), *Instrument Design and Performance for Optical/Infrared Groundbased Telescopes.*, volume 4841, pages 1548–1561. Proceedings of the SPIE

Falco, E. E., Kurtz, M. J., Geller, M. J., Huchra, J. P., Peters, J., Berlind, P., Mink, D. J., Tokarz, S. P., & Elwell, B., 1999; *The Updated Zwicky Catalog (UZC).* Publications of the Astronomical Society of the Pacific, 111:438

Fan, X., Narayanan, V. K., Strauss, M. A., White, R. L., Becker, R. H., Pentericci, L., & Rix, H.-W., 2002; *Evolution of the Ionizing Background and the Epoch of Reionization from the Spectra of z˜6 Quasars.* Astronomical Journal, 123:1247

Fischer, J. U., Hasinger, G., Schwope, A. D., Brunner, H., Boller, T., Trmper, J., Voges, W., & Neizvestnyj, S., 1998; *The ROSAT Bright Survey. I. Identification of an AGN sample with hard ROSAT X-ray spectra.* Astronomische Nachrichten, 319:347

Fischer, S., Iserlohe, C., Zuther, J., Bertram, T., Straubmeier, C., & Eckart, A., 2006a; *NIR imaging and spectroscopy of AGN hosts at z <= 0.06*. New Astronomy Review, 50:736

Fischer, S., Iserlohe, C., Zuther, J., Bertram, T., Straubmeier, C., Schdel, R., & Eckart, A., 2006b; *Nearby AGN and their hosts in the near infrared*. Astronomy and Astrophysics, 452:827

Fischer, S., Moratschke, D., Straubmeier, C., Eckart, A., Rossi, L., Plesseria, J.-Y., Renotte, E., Mazy, E., & Amiaux, J., 2008; *The JWST MIRI double-prism: design and science drivers*. In J. M. Oschmann, Jr, M. W. M. de Graauw, & H. A. MacEwen (editors), *Space Telescopes and Instrumentation 2008: Optical, Infrared, and Millimeter*, volume 7010, page 70103K. Proceedings of the SPIE

Fischer, S., Straubmeier, C., Eckart, A., Rossi, L., & Mazy, E., 2006c; *Mounting MIRI's double prism*. In J. C. Mather, H. A. MacEwen, & M. W. M. de Graauw (editors), *Space Telescopes and Instrumentation I: Optical, Infrared, and Millimeter*, volume 6265, page 62653A. Proceedings of the SPIE

Frogel, J. A., Persson, S. E., Matthews, K., & Aaronson, M., 1978; *Photometric studies of composite stellar systems. I - CO and JHK observations of E and S0 galaxies*. Astrophysical Journal, 220:75

Gaffney, N. I., Lester, D. F., & Doppmann, G., 1995; *Measuring stellar kinematics in galaxies with the near-infrared (2-0) (12) CO absorption bandhead*. Publications of the Astronomical Society of the Pacific, 107:68

Gaffney, N. I., Lester, D. F., & Telesco, C. M., 1993; *Kinematics of the M82 Starburst*. In *Bulletin of the American Astronomical Society*, volume 25, page 842

Gardner, J. P., Mather, J. C., Clampin, M., Doyon, R., Greenhouse, M. A., Hammel, H. B., Hutchings, J. B., Jakobsen, P., Lilly, S. J., Long, K. S., Lunine, J. I., McCaughrean, M. J., Mountain, M., Nella, J., Rieke, G. H., Rieke, M. J., Rix, H.-W., Smith, E. P., Sonneborn, G., Stiavelli, M., Stockman, H. S., Windhorst, R. A., & Wright, G. S., 2006; *The James Webb Space Telescope*. Space Science Reviews, 123:485

Geballe, T. R., Krisciunas, K., Lee, T. J., Gatley, I., Wade, R., Duncan, W. D., Garden, R., & Becklin, E. E., 1984; *Observations of broad helium and hydrogen lines in the very center of the galaxy*. Astrophysical Journal, 284:118

Glass, I. S., 1984; *JHK colours of 'ordinary' galaxies*. Monthly Notices of the Royal Astronomical Society, 211:461

Glass, I. S., 2004; *Long-term infrared photometry of Seyferts*. Monthly Notices of the Royal Astronomical Society, 350:1049

Glikman, E., Helfand, D. J., & White, R. L., 2006; *A Near-Infrared Spectral Template for Quasars*. Astrophysical Journal, 640:579

Goldader, J. D., Joseph, R. D., Doyon, R., & Sanders, D. B., 1995; *Spectroscopy of luminous infrared galaxies at 2 microns: 1. The ultraluminous galaxies (L_{IR} approximately greater than 10 ¹² solar luminosity)*. Astrophysical Journal, 444:97

Grupe, D., Beuerman, K., Mannheim, K., Thomas, H. C., Fink, H. H., & de Martino, D., 1995; *Discovery of an ultrasoft transient ROSAT AGN: WPVS 007.* Astronomy and Astrophysics, 300:L21

Hall, D. N. B., Kleinmann, S. G., & Scoville, N. Z., 1982; *Broad helium emission in the galactic center*. Astrophysical Journal, 260:L53

Hinkle, K. & Wallace, L., 2001; *Spectral Atlases of Cool Stars in the Infrared and Visible (CD-ROM Directory: contribs/hinkle)*. In R. J. G. Lopez, R. Rebolo, & M. R. Z. Osorio (editors), *11th Cambridge Workshop on Cool Stars, Stellar Systems and the Sun*, volume 223 of *Astronomical Society of the Paci?c Conference Series*, pages 803–+

Hyland, A. R. & Allen, D. A., 1982; *Aninfrared study of quasars*. Monthly Notices of the Royal Astronomical Society, 199:943

Ivanov, V. D., Rieke, M. J., Engelbracht, C. W., Alonso-Herrero, A., Rieke, G. H., & Luhman, K. L., 2004; *A Medium-Resolution Near-Infrared Spectral Library of Late-Type Stars. I.* Astrophysical Journal Supplement Series, 151:387

Jahnke, K., Kuhlbrodt, B., & Wisotzki, L., 2004; *Quasar host galaxy star formation activity from multicolour data*. Monthly Notices of the Royal Astronomical Society, 352:399

Jahnke, K. & Wisotzki, L., 2003; *The B-band luminosities of quasar host galaxies*. Monthly Notices of the Royal Astronomical Society, 346:304

Jakobsen, P. & Jensen, P., 2008; *James Webb Space Telescope, A Bigger and Better Time Machine*. ESA Bulletin, 133

Kennicutt, R. C., 1983; *The rate of star formation in normal disk galaxies*. Astrophysical Journal, 272:54

Kewley, L. J., Heisler, C. A., Dopita, M. A., & Lumsden, S., 2001; *Optical Classification of Southern Warm Infrared Galaxies*. Astrophysical Journal Supplement Series, 132:37

Kleinmann, S. G. & Hall, D. N. B., 1986; *Spectra of late-type standard stars in the region 2.0-2.5 microns*. Astrophysical Journal Supplement Series, 62:501

Knapen, J. H., Shlosman, I., & Peletier, R. F., 2000; *A Subarcsecond Resolution Near-Infrared Study of Seyfert and "Normal" Galaxies. II. Morphology*. Astrophysical Journal, 529:93

Kogut, A., Spergel, D. N., Barnes, C., Bennett, C. L., Halpern, M., Hinshaw, G., Jarosik, N., Limon, M., Meyer, S. S., Page, L., Tucker, G. S., Wollack, E., & Wright, E. L., 2003; *First-Year Wilkinson Microwave Anisotropy Probe (WMAP) Observations: Temperature-Polarization Correlation*. Astrophysical Journal Supplement Series, 148:161

Komossa, S. & Xu, D., 2007; *Narrow-Line Seyfert 1 Galaxies and the M_{BH}-sigma Relation*. Astrophysical Journal, 667:L33

Kroes, G., Oudenhuysen, A., Meijers, M., & Pel, J.-W., 2005; *MIRI-JWST spectrometer main optics opto-mechanical design andprototyping*. In A. E. Hatheway (editor), *Optomechanics*, volume 5877, page 58770P. Proceedings of the SPIE

Lim, T., Alvarez, J. L., Bauwens, E., Bedregal, A. G., Blommaert, J., Dannerbauer, H., Eccleston, P., Ferlet, M., Fischer, S., Garcia-Marin, M., Glasse, A., Glauser, A. M., Gordon, K., Greene, T., Grundy, T., Hennemann, M., Klaas, U., Labiano, A., Lahuis, F., Martinez-Galarza, J. R., Martin, B. M., Morrison, J., Nakos, T., O'Sullivan, B., Pindor, B., Ressler, M., Shaughnessy, B., Vandenbussche, B., Wells, M., Wright, G., & Zuther, J., 2008; *First results from MIRI verification model testing*. In J. M. Oschmann, Jr, M. W. M. de Graauw, & H. A. MacEwen (editors), *Space Telescopes and Instrumentation 2008: Optical, Infrared, and Millimeter*, volume 7010, page 70103A. Proceedings of the SPIE

Magorrian, J., Tremaine, S., Richstone, D., Bender, R., Bower, G., Dressler, A., Faber, S. M., Gebhardt, K., Green, R., Grillmair, C., Kormendy, J., & Lauer, T., 1998; *The Demography of Massive Dark Objects in Galaxy Centers*. Astronomical Journal, 115:2285

Maia, M. A. G., Machado, R. S., & Willmer, C. N. A., 2003; *The Seyfert Population in the Local Universe*. Astronomical Journal, 126:1750

Maiolino, R., Rieke, G. H., & Rieke, M. J., 1996; *Correction of the Atmospheric Transmission in Infrared Spectroscopy*. Astronomical Journal, 111:537

Malkan, M. A., Gorjian, V., & Tam, R., 1998; *A Hubble Space Telescope Imaging Survey of Nearby Active Galactic Nuclei*. Astrophysical Journal Supplement Series, 117:25

Marconi, A., Moorwood, A. F. M., Salvati, M., & Oliva, E., 1994; *A (Si VI) (1.92 micrometer) coronal line survey of galactic nuclei*. Astronomy and Astrophysics, 291:18

Martini, P., Regan, M. W., Mulchaey, J. S., & Pogge, R. W., 2003; *Circumnuclear Dust in Nearby Active and Inactive Galaxies. II. Bars, Nuclear Spirals, and the Fueling of Active Galactic Nuclei*. Astrophysical Journal, 589:774

McLeod, K. K. & Rieke, G. H., 1995; *Luminous Quasars in Luminous Early-Type Host Galaxies*. Astrophysical Journal, 454:L77

Mountain, M., 2005; *Draft Report of the JWST Science Assessment Team*. Report of the JWST Science Assessment Team

Mouri, H., 1994; *Molecular hydrogen emission in galaxies: Determination of excitation mechanism*. Astrophysical Journal, 427:777

Nagao, T., Murayama, T., & Taniguchi, Y., 2001; *The Narrow-Line Region of Seyfert Galaxies: Narrow-Line Seyfert 1 Galaxies versus Broad-Line Seyfert 1 Galaxies*. Astrophysical Journal, 546:744

Oliva, E. & Moorwood, A. F. M., 1990; *Detection of forbidden Si VI 1.962 microns and new observations of infrared H, forbidden Fe II, and H2 line emission in the Seyfert galaxy NGC 1068*. Astrophysical Journal, 348:L5

Oliva, E., Origlia, L., Kotilainen, J. K., & Moorwood, A. F. M., 1995; *Red supergiants as starburst tracers in galactic nuclei.* Astronomy and Astrophysics, 301:55

Origlia, L., Moorwood, A. F. M., & Oliva, E., 1993; *The 1.5-1.7 micrometer spectrum of cool stars: Line identifications, indices for spectral classification and the stellar content of the Seyfert galaxy NGC 1068*. Astronomy and Astrophysics, 280:536

Origlia, L. & Oliva, E., 2000; *Is the [CO] index an age indicator for star forming galaxies?* Astronomy and Astrophysics, 357:61

Osterbrock, D. E., 1989; *Astrophysics of gaseous nebulae and active galactic nuclei*

Page, L., Hinshaw, G., Komatsu, E., Nolta, M. R., Spergel, D. N., Bennett, C. L., Barnes, C., Bean, R., Dor, O., Dunkley, J., Halpern, M., Hill, R. S., Jarosik, N., Kogut, A., Limon, M., Meyer, S. S., Odegard, N., Peiris, H. V., Tucker, G. S., Verde, L., Weiland, J. L., Wollack, E., & Wright, E. L., 2007; *Three-Year Wilkinson Microwave Anisotropy Probe (WMAP) Observations: Polarization Analysis*. Astrophysical Journal Supplement Series, 170:335

Panagia, N., 2003; *The Quest for Primordial Stellar Populations and the James Webb Space Telescope*. Chinese Journal of Astronomy and Astrophysics Supplement, 3:115

Panagia, N., Fall, S. M., Mobasher, B., Dickinson, M., Ferguson, H. C., Giavalisco, M., Stern, D., & Wiklind, T., 2005; *Direct Evidence for an Early Reionization of the Universe?* Astrophysical Journal, 633:L1

Panuzzo, P., Bressan, A., Granato, G. L., Silva, L., & Danese, L., 2003; *Dust and nebular emission. I. Models for normal galaxies*. Astronomy and Astrophysics, 409:99

Reimers, D., Koehler, T., & Wisotzki, L., 1996; *The Hamburg/ESO survey for bright QSOs. II. Follow-up spectroscopy of 160 quasars and Seyferts.* Astronomy and Astrophysics Supplement Series, 115:235

Renotte, E., Rossi, L., Fischer, S., & Plesseria, J.-Y., 2006; *MIRI-NC-00012-CSL iss7, DM prism vibration*

Reunanen, J., Kotilainen, J. K., & Prieto, M. A., 2002; *Near-infrared spectroscopy of nearby Seyfert galaxies - I. First results*. Monthly Notices of the Royal Astronomical Society, 331:154

Rieke, G. H. & Lebofsky, M. J., 1985; *The interstellar extinction law from 1 to 13 microns*. Astrophysical Journal, 288:618

Riffel, R., Rodríguez-Ardila, A., & Pastoriza, M. G., 2006; *A 0.8-2.4 mum spectral atlas of active galactic nuclei*. Astronomy and Astrophysics, 457:61

Rodríguez-Ardila, A., Binette, L., Pastoriza, M. G., & Donzelli, C. J., 2000a; *The Narrow-Line Region of Narrow-Line Seyfert 1 Galaxies*. Astrophysical Journal, 538:581

Rodríguez-Ardila, A., Pastoriza, M. G., & Donzelli, C. J., 2000b; *Visible and Near-Infrared Spectroscopy of Seyfert 1 and Narrow-Line Seyfert 1 Galaxies*. Astrophysical Journal Supplement Series, 126:63

Rodríguez-Ardila, A., Pastoriza, M. G., Viegas, S., Sigut, T. A. A., & Pradhan, A. K., 2004; *Molecular hydrogen and [Fe II] in Active Galactic Nuclei*. Astronomy and Astrophysics, 425:457

Rodríguez-Ardila, A., Riffel, R., & Pastoriza, M. G., 2005; *Molecular hydrogen and [FeII] in active galactic nuclei - II. Results for Seyfert 2 galaxies*. Monthly Notices of the Royal Astronomical Society, 364:1041

Rossi, L., Jamoye, J.-F., Renotte, E., Mazy, E., Plesseria, J.-Y., Ninane, N., Wielandts, M., Fischer, S., Straubmeier, C., Augueres, J.-L., Dubreuil, D., Amiaux, J., Poupar, S., & Ronayette, S., 2008; *Manufacturing and verification of ZnS and Ge prisms for the JWST MIRI imager*. In E. Atad-Ettedgui & D. Lemke (editors), *Advanced Optical and Mechanical Technologies in Telescopes and Instrumentation*, volume 7018, page 701823. Proceedings of the SPIE

Rowlands, N., Evans, C., Greenberg, E., Gregory, P., Scott, A., Thibault, S., Poirier, M., Doyon, R., Hutchings, J. B., & Alexander, R., 2004; *Tunable filters for JWST Fine Guidance Sensor*. In J. C. Mather (editor), *Optical, Infrared, and Millimeter Space Telescopes.*, volume 5487, pages 676–687. Proceedings of the SPIE

Sanders, D. B., Soifer, B. T., Elias, J. H., Madore, B. F., Matthews, K., Neugebauer, G., & Scoville, N. Z., 1988; *Ultraluminous infrared galaxies and the origin of quasars*. Astrophysical Journal, 325:74

Schade, D. J., Boyle, B. J., & Letawsky, M., 2000; *Hubble Space Telescope observations of X-ray-selected active galactic nuclei*. Monthly Notices of the Royal Astronomical Society, 315:498

Schlegel, D. J., Finkbeiner, D. P., & Davis, M., 1998; *Maps of Dust Infrared Emission for Use in Estimation of Reddening and Cosmic Microwave Background Radiation Foregrounds*. Astrophysical Journal, 500:525

Shlosman, I., Frank, J., & Begelman, M. C., 1989; *Bars within bars - A mechanism for fuelling active galactic nuclei*. Nature, 338:45

Shu, F. H., Adams, F. C., & Lizano, S., 1987; *Star formation in molecular clouds - Observation and theory*. Annual Review of Astronomy and Astrophysics, 25:23

Simpson, C., Forbes, D. A., Baker, A. C., & Ward, M. J., 1996; *Forbidden Feˆ+ emission from active galaxies*. Monthly Notices of the Royal Astronomical Society, 283:777

Smith, E. P., Heckman, T. M., Bothun, G. D., Romanishin, W., & Balick, B., 1986; *On the nature of QSO host galaxies*. Astrophysical Journal, 306:64

Spergel, D. N., Bean, R., Dor, O., Nolta, M. R., Bennett, C. L., Dunkley, J., Hinshaw, G., Jarosik, N., Komatsu, E., Page, L., Peiris, H. V., Verde, L., Halpern, M., Hill, R. S., Kogut, A., Limon, M., Meyer, S. S., Odegard, N., Tucker, G. S., Weiland, J. L., Wollack, E., & Wright, E. L., 2007; *Three-Year Wilkinson Microwave Anisotropy Probe (WMAP) Observations: Implications for Cosmology*. Astrophysical Journal Supplement Series, 170:377

Steakley, B., 2005; *NIRCam systems engineering: the recipe*. In J. B. Heany & L. G. Burriesci (editors), *Cryogenic Optical Systems and Instruments XI.*, volume 5904, pages 9–20. Proceedings of the SPIE

Tamura, M., Kleinmann, S. G., Scoville, N. Z., & Joyce, R. R., 1991; *Near-infrared long-slit spectra of NGC 1068*. Astrophysical Journal, 371:131

Taylor, G. L., Dunlop, J. S., Hughes, D. H., & Robson, E. I., 1996; *A near-IR study of the host galaxies of radio-quiet quasars, radio-loud quasars and radio galaxies*. Monthly Notices of the Royal Astronomical Society, 283:930

Thronson, H. A., Majewski, S., Descartes, L., & Hereld, M., 1990; *A subdued interpretation of the visual and infrared emission from merging galaxies - Application to NGC 6240*. Astrophysical Journal, 364:456

Valdés, J. R., Berta, S., Bressan, A., Franceschini, A., Rigopoulou, D., & Rodighiero, G., 2005; *NIR spectroscopy of luminous infrared galaxies and the hydrogen recombination photon deficit*. Astronomy and Astrophysics, 434:149

Vaughan, S., Edelson, R., & Warwick, R. S., 2004; *Chandra observations of five X-ray transient galactic nuclei*. Monthly Notices of the Royal Astronomical Society, 349:L1

Wadadekar, Y., 2004; *Radio emission from AGN detected by the VLA FIRST survey*. Astronomy and Astrophysics, 416:35

Ward, M., Allen, D. A., Wilson, A. S., Smith, M. G., & Wright, A. E., 1982; *The near infrared properties of Seyfert and related active galaxies*. Monthly Notices of the Royal Astronomical Society, 199:953

White, S. D. M. & Frenk, C. S., 1991; *Galaxy formation through hierarchical clustering*. Astrophysical Journal, 379:52

Winkler, H., Stirpe, G. M., & Sekiguchi, K., 1992; *The spectroscopic analysis of emission line galaxies identified from an objective prism survey*. Astronomy and Astrophysics Supplement Series, 94:103

Wisotzki, L., Christlieb, N., Bade, N., Beckmann, V., Khler, T., Vanelle, C., & Reimers, D., 2000; *The Hamburg/ESO survey for bright QSOs. III. A large flux-limited sample of QSOs*. Astronomy and Astrophysics, 358:77

Wisotzki, L., Koehler, T., Groote, D., & Reimers, D., 1996; *The Hamburg/ESO survey for bright QSOs. I. Survey design and candidate selection procedure.* Astronomy and Astrophysics Supplement Series, 115:227

Wright, D., 2007; *DPA random vibration design loads, MIRI-CP-00073-AEU*

Wright, D., O'Sullivan, B., Thatcher, J., Renouf, I., Wright, G., Wells, M., Glasse, A., Grozinger, U., Sykes, J., Smith, D., Eccleston, P., & Shaughnessy, B., 2008a; *System engineering and management in a large and diverse multinational consortium*. In G. Z. Angeli & M. J. Cullum (editors), *Modeling, Systems Engineering, and Project Management for Astronomy III*, volume 7017, page 701708. Proceedings of the SPIE

Wright, G. S., Reike, G., Barella, P., Boeker, T., Colina, L., van Dishoeck, E., Driggers, P., Goodson, G., Greene, T., Heske, A., Henning, T., Lagage, P.-O., Meixner, M., Norgaard-Nielsen, H., Olofsson, G., Ray, T., Ressler, M., Thatcher, J., Waelkens, C., Wright, D., & Zehnder, A., 2008b; *Design and development of MIRI, the mid-IR instrument for JWST*. In J. M. Oschmann, Jr, M. W. M. de Graauw, & H. A. MacEwen (editors), *Space Telescopes and Instrumentation 2008: Optical, Infrared, and Millimeter*, volume 7010, page 70100T. Proceedings of the SPIE

Zuther, J., Iserlohe, C., Pott, J. U., Bertram, T., Fischer, S., Voges, W., Hasinger, G., & Eckart, A., 2007; *Mrk 609: resolving the circumnuclear structure with near-infrared integral field spectroscopy*. Astronomy and Astrophysics, 466:451

List of Figures

List of Tables

Danksagung

At long last, one of the arguably most important parts of my thesis - the acknowledgments!

First and foremost, I would like to express my thanks to my supervisor, Prof. Dr. A. Eckart, for giving me the opportunity to be able to combine instrumentational and observational studies in the course of my thesis. His open guidance has always confirmed me in what I'm doing.

My thanks go also to Prof. Dr. M. Abd-Elmeguid for refereeing my thesis, and to Prof. Dr. J. Saur for being the president of my disputation committee.

I also thank Christian Straubmeier & Thomas Bertram, who were always there with useful comments and inspiring discussions, and Jens Zuther, with whom I spent many fun nights writing proposals and getting Lost.

Ich danke auch Herrn Mondt und der gesamten Werkstatt, allen voran Damian Moratschke, für die sehr gute Zusammenarbeit und die Geduld, die sie immer wieder aufbringen mussten. Vor allen die vielen Pläne und gegenseitige Motivation auf den zahlreichen Zugfahrten nach und von Lüttich zurück haben mich auch nach etwaigen Rückschlägen meinen Optimismus nie (oder nur kurzzeitig, aber dann schnell in belgischem Bier ertränkt) verlieren lassen.

Je rends beaucoup d'hommage pour leur collaboration à mes collègues belges du CSL, et ce particulìrement à Laurence Rossi, Jean-Yves Plesseria et Etienne Renotte. Je les remercie profondément pour l'excellente collaboration et pour l'appui au sein du team MIRI. Un grand merci aussi à Charlotte Delree pour l'aide qu'elle m'a apportée pendant les tests de vibration innombrables.

In addition, I would like to thank Prof. Dr. Krabbe and Christof Iserlohe for observing HE 0036-5133 during their DDTime. Christof also provided me with helpful insights into SINFONI data, even at the very 'last' moment.

My thanks go also to Jens Zuther & Macarena Garcia-Marin for the help during our MIRI-testscript development and the nice time during our stays at RAL.

Of course, thanks go also to all the cool people from the ”aegroup”, including former members Rainer Schödel and Leo Meyer, for a harmonic and humorous working atmosphere.

Darüber hinaus gebührt mein ganz besonderer Dank:
meinen Eltern, ohne deren immerwährende Unterstützung ich sicherlich nie so weit gekommen wäre;
meiner Lieblingsschwester Kathrin, auf die ich immer zählen kann (auch wenn ich nicht der ”Raketenwissenschaftler” bin, für den sie mich zu verkaufen versucht);
meinem Opa Kurt, der mit mir zusammen zum Mond geflogen wäre, aber nie in ein Flugzeug auch nur einen Fuß gesetzt hätte;
Sascha und Philippe für den Weltmeistertitel;
und zu guter letzt meiner Freundin Lisa, alldieweil sie sich nie (groß) über die vielen Dienstreisen und die so oft viel zu wenige Zeit, die ich für sie habe, beschwert hat, und die mir immer wieder hilft, allen Streß des Alltags innerhalb kürzester Zeit zu vergessen.

This work is supported by the German federal department for education and research (BMBF) under the project numbers: 50OS0502 & 50OS0801.

Erklärung

Ich versichere, dass ich die von mir vorgelegte Dissertation selbständig angefertigt, die benutzten Quellen und Hilfsmittel vollständig angegeben und die Stellen der Arbeit – einschließlich Tabellen, Karten und Abbildungen – die anderen Werken im Wortlaut oder dem Sinn nach entnommen sind, in jedem Einzelfall als Entlehnung kenntlich gemacht habe; dass diese Dissertation noch keiner anderen Fakultät oder Universität zur Prüfung vorgelegen hat; dass sie – abgesehen von unten angegebenen Teilpublikationen – noch nicht veröffentlicht worden ist sowie, dass ich eine solche Veröffentlichung vor Abschluss des Promotionsverfahrens nicht vornehmen werde. Die Bestimmungen dieser Promotionsordnung sind mir bekannt. Die von mir vorgelegte Dissertation ist von Herrn Prof. Dr. Andreas Eckart betreut worden.

Köln, den 19. September 2008

Teile der Dissertation sind in den folgenden Publikationen enthalten:

Fischer, S., C. Iserlohe, J. Zuther, T. Bertram, C. Straubmeier, und A. Eckart. 2006; *NIR imaging and spectroscopy of AGN hosts at z < 0.06.* New Astronomy Review 50: 736-738.

Fischer, S., C. Iserlohe, J. Zuther, T. Bertram, C. Straubmeier, R. Schödel, & A. Eckart, 2006; *Nearby AGN and their hosts in the near infrared.* Astronomy and Astrophysics 452: 827-837.

Fischer, S., C. Straubmeier, A. Eckart, L. Rossi, & E. Mazy. 2006; *Mounting MIRI's double prism.* In J. C. Mather, H. A. MacEwen, & M. W. M. de Graauw (editors), *Space Telescopes and Instrumentation I: Optical, Infrared, and Millimeter*, 6265:62653A. Proceedings of the SPIE.

Fischer, S., D. Moratschke, C. Straubmeier, A. Eckart, L. Rossi, J.-Y. Plesseria, E. Renotte, E. Mazy, & J. Amiaux. 2008; *The JWST MIRI double-prism: design and science drivers*. In J. M. Oschmann, Jr, M. W. M. de Graauw, & H. A. MacEwen (editors), *Space Telescopes and Instrumentation 2008: Optical, Infrared, and Millimeter*, 7010:70103K. Proceedings of the SPIE.

Weitere Veröffentlichungen:

Bertram, T., A. Eckart, **S. Fischer**, J. Zuther, C. Straubmeier, L. Wisotzki, & M. Krips, 2007; *Molecular gas in nearby low-luminosity QSO host galaxies.* Astronomy and Astrophysics 470: 571-583.

Bertram, T., A. Eckart, M. Krips, C. Straubmeier, **S. Fischer**, & J. G. Staguhn, 2006; *Molecular gas in QSO host galaxies.* New Astronomy Review 50: 712-715.

Krips, M., A. Eckart, R. Neri, T. Bertram, C. Straubmeier, **S. Fischer**, J. G. Staguhn, & S. N. Vogel, 2007; *Barred CO emission in HE 1029-1831.* Astronomy and Astrophysics 464: 187-191.

Lim, T., J. L. Alvarez, E. Bauwens, A. G. Bedregal, J. Blommaert, H. Dannerbauer, P. Eccleston, M. Ferlet, **S. Fischer**, M. Garcia-Marin, A. Glasse, A.M. Glauser, K. Gordon, T. Greene, T. Grundy, M. Hennemann, U. Klaas, A. Labiano, F. Lahuis, J. R. Martinez-Galarza, B. M. Martin, J. Morrison, T. Nakos, B. O'Sullivan, B. Pindor, M. Ressler, B. Shaughnessy, B. Vandenbussche, M. Wells, G. Wright, & J. Zuther, 2008; *First results from MIRI verification model testing.* In J. M. Oschmann, Jr, M. W. M. de Graauw, & H. A. MacEwen (editors), *Space Telescopes and Instrumentation 2008: Optical, Infrared, and Millimeter*, 7010:70103A. Proceedings of the SPIE.

Rossi, L., J.-F. Jamoye, E. Renotte, E. Mazy, J.-Y. Plesseria, N. N., M. Wielandts, **S. Fischer**, C. Straubmeier, J.-L. Augueres, D. Dubreuil, J. Amiaux, S. Poupar, & S. Ronayette, 2008 ; *Manufacturing and verification of ZnS and Ge prisms for the JWST MIRI imager.* In E. Atad-Ettedgui & D. Lemke (editors), *Advanced Optical and Mechanical Technologies in Telescopes and Instrumentation*, 7018:701823. Proceedings of the SPIE.

Zuther, J., C. Iserlohe, J. -U Pott, T. Bertram, **S. Fischer**, W. Voges, G. Hasinger, & A. Eckart, 2007. *Mrk 609: resolving the circumnuclear structure with near-infrared integral field spectroscopy.* Astronomy and Astrophysics 466: 451-466.

Zuther, J., **S. Fischer**, J.-U. Pott, T. Bertram, A. Eckart, C. Straubmeier, C. Iserlohe, W. Voges, & G. Hasinger, 2007. *Dissecting the Nuclear Environment of Mrk 609 with SINFONI the Starburst-AGN Connection.* The ESO Messenger 128: 44.